

TRANSACTIONS ON MACHINE LEARNING AND ARTIFICIAL INTELLIGENCE

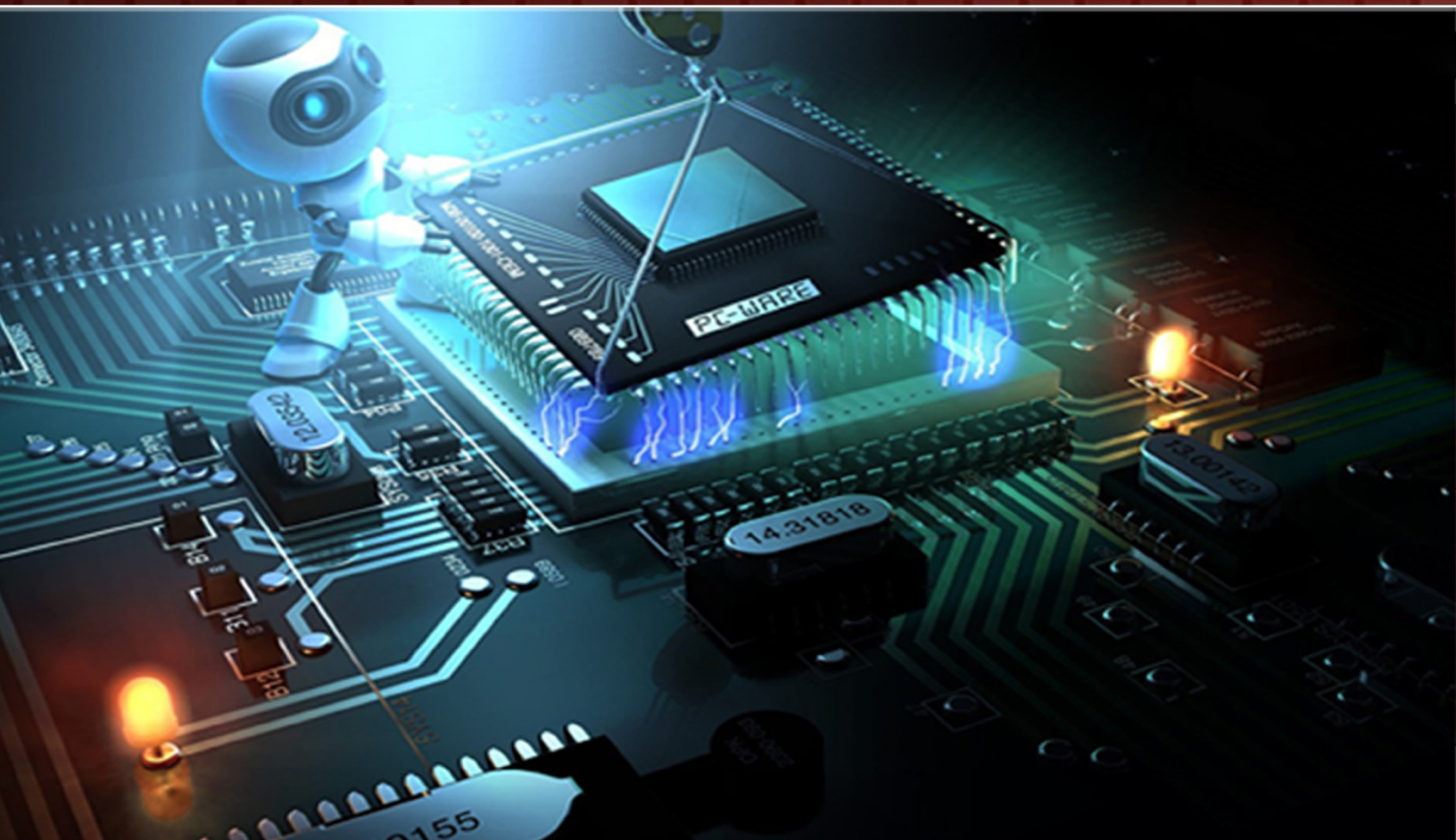


TABLE OF CONTENTS

EDITORIAL ADVISORY BOARD	I
DISCLAIMER	II
Image Learning of Charge Motion in Electric and Magnetic Fields by Java Programming Masami Morooka, Suhua Qian, Midori Morooka	1
A novel Approach to System Security using Derived Odor Keys with Weight Elimination Neural Algorithm (DOK-WENA) Mahmoud Z. Iskandarani	20
Algorithm Development for Analysis of Statistical Accuracy of the Extraction of Cartographic Features in Digital Images Guilherme Pina Cardim, Erivaldo Antônio da Silva, Maurício Araújo Dias	32
Convolutional Bottleneck Network with Dropout for Dysarthric Speech Recognition Toru Nakashika, Toshiya Yoshioka, Tetsuya Takiguchi, Yasuo Arika Stefan Duffner, Christophe Garcia	48
Experimental Verification of Parameter Identification Method based on Symbolic Time Series Analysis and Adaptive Immune Clonal Selection Algorithm Rongshuai Li	63
A MATLAB Toolbox for Misconceptions Analysis Based on S-P Chart, Grey Relational Analysis and ROC Tian-Wei Sheu, Phuoc-Hai Nguyen, Phung-Tuyen Nguyen, Duc-Hieu Pham, Ching-Pin Tsai and Masatake Nagai	72
On Securing a Door with Finger Print Biometric Technique Adeolu Afolabi, Oke Alice	86

EDITORIAL ADVISORY BOARD

Professor Er Meng Joo

Nanyang Technological University
Singapore

Professor Djamel Bouchaffra

Grambling State University, Louisiana
United States

Prof Bhavani Thuraisingham

The University of Texas at Dallas
United States

Professor Dong-Hee Shin,

Sungkyunkwan University, Seoul
Republic of Korea

Professor Filippo Neri,

Faculty of Information & Communication Technology,
University of Malta,
Malta

Prof Mohamed A Zohdy,

Department of Electrical and Computer Engineering,
Oakland University,
United States

Dr Kyriakos G Vamvoudakis,

Dept of Electrical and Computer Engineering, University of
California Santa Barbara
United States

Dr M. M. Fraz

Kingston University London
United Kingdom

Dr Luis Rodolfo Garcia

College of Science and Engineering, Texas A&M University,
Corpus Christi
United States

Dr Hafiz M. R. Khan

Department of Biostatistics, Florida International
University
United States

Dr Xiaocong Fan

The Pennsylvania State University
United States

Dr Julia Johnson

Dept. of Mathematics & Computer Science, Laurentian
University, Ontario,
Canada

Dr Chen Yanover

Machine Learning for Healthcare and Life Sciences
IBM Haifa Research Lab, Israel

Dr Vandana Janeja

University of Maryland, Baltimore
United States

Dr Nikolaos Georgantas

Senior Research Scientist at INRIA, Paris-Rocquencourt
France

Dr Zeyad Al-Zhour

College of Engineering, The University of Dammam
Saudi Arabia

Dr Zdenek Zdrahal

Knowledge Media Institute, The Open University, Milton
Keynes
United Kingdom

Dr Farouk Yalaoui

Institut Charles Dalaunay, University of Technology of
Troyes
France

Dr Jai N Singh

Barry University, Miami Shores, Florida
United States

DISCLAIMER

All the contributions are published in good faith and intentions to promote and encourage research activities around the globe. The contributions are property of their respective authors/owners and the journal is not responsible for any content that hurts someone's views or feelings etc.

Image Learning of Charge Motion in Electric and Magnetic Fields by Java Programming

Masami Morooka¹, Suhua Qian¹, Midori Morooka²

¹ *Department of Electrical Engineering, Fukuoka Inst. Tech, Higashi-ku, Fukuoka 811-0295, Japan;*

² *Flash Design Center, Micron Japan, P. O. Box 57, Kamata 5-37-1, Ota-ku, Tokyo, Japan;*

ABSTRACT

Java programs in a GUI environment have been developed for an image learning of charge motions in electric and magnetic fields. Text fields of selected parameters for the numerical calculation of the differential equations of the charge motion, such as the electric field and magnetic field, are set on the display, and the calculation by Runge-Kutta method is begun by clicking the start button after inputting values into the text fields. The calculated results are plotted immediately after the completion of the calculation as a figure on the display, e.g., a charge locus for the simulation of charge motion. By changing the values in the text fields, new results can be represented immediately, and the charge motion under a new electric and magnetic fields can be easily simulated. These Java programs are useful in education applications for rapidly and accurately image learning for the phenomena expressed by ordinary differential equations.

Keywords: Image learning, charge motion in electric and magnetic fields, Java programming, ordinary differential equations.

1 INTRODUCTION

In many situations, it is often difficult to obtain the charge motion, e. g. the charge locus, in electric and magnetic fields, and it is even more difficult to visualize the variation of the motion due to the change in the fields. The charge motion can be expressed by ordinary differential equations which can be solved numerically by Runge-Kutta method. With the wide use of Java programming and the rapid development of personal computers, the author has recently directly solved the partial differential equations and has shown that the complicated diffusion of Au into Si can be simulated easily by the Java programming [1]. In this paper, the ordinary differential equations for a charge motion in electric and magnetic fields have been solved numerically, and the locus of the charge motion in the fields can be easily and accurately simulated using Java in a GUI (graphical user interface) environment.

2 NUMERICAL METHOD FOR CHARGE MOTION IN ELECTRIC AND MAGNETIC FIELDS

2.1 Basic Equations for Charge Motion in Electric and Magnetic Fields

We simulate the motion of a charge q in an applied electric field $\mathbf{E} = (E_x, E_y, E_z)$ and an applied magnetic field $\mathbf{B} = (B_x, B_y, B_z)$. The charge motion is generally affected by the resistance force based on collisions and by the restoring Coulomb force in addition to the electric and electro-magnetic forces. The charge motion under these forces is given as

$$m \frac{d\mathbf{v}}{dt} = -a\mathbf{v} + q\mathbf{E} + q\mathbf{v} \times \mathbf{B} - b(\mathbf{r} - \mathbf{r}_{R0}). \quad (1)$$

Here, m , $\mathbf{v} = (v_x, v_y, v_z)$, and $\mathbf{r} = (x, y, z)$ are the mass, velocity, and displacement of the charge, respectively. a and b are coefficients of the resistance and restoring forces. $\mathbf{r}_{R0} = (x_{R0}, y_{R0}, z_{R0})$ is the restoring center, and

$$\frac{d\mathbf{r}}{dt} = \mathbf{v}. \quad (2)$$

By decomposing the vector equations (7) and (8) into the scalar equations in the x , y , and z directions, we obtain

$$m \frac{dv_x}{dt} = -av_x + qE_x + q(v_y B_z - v_z B_y) - b(x - x_{R0}), \quad (3)$$

$$m \frac{dv_y}{dt} = -av_y + qE_y + q(v_z B_x - v_x B_z) - b(y - y_{R0}) \quad (4)$$

$$m \frac{dv_z}{dt} = -av_z + qE_z + q(v_x B_y - v_y B_x) - b(z - z_{R0}), \quad (5)$$

$$\frac{dx}{dt} = v_x, \quad (6)$$

$$\frac{dy}{dt} = v_y, \quad (7)$$

$$\frac{dz}{dt} = v_z. \quad (8)$$

In the case of the magnetic field having a fixed direction, for example, $\mathbf{B} = (0, 0, B_z)$, we obtain the following equations, which are simpler than equations (3) - (5).

$$m \frac{dv_x}{dt} = -av_x + qE_x + qv_y B_z - b(x - x_{R0}), \quad (9)$$

$$m \frac{dv_y}{dt} = -av_y + qE_y - qv_x B_z - b(y - y_{R0}), \quad (10)$$

$$m \frac{dv_z}{dt} = -av_z + qE_z - b(z - z_{R0}). \quad (11)$$

In this case, we can obtain the charge motion in the x and y directions by solving four ordinary differential equations ((6), (7), (9), and (10)) and the motion in the z direction by solving two ordinary differential equations ((8) and (11)).

2.2 Runge-Kutta Method

The ordinary differential equations can be solved numerically using the fourth-order Runge-Kutta method. When differential equations for dependent variables $(y_1(t), y_2(t), \dots, y_n(t))$ of the independent variable, t , are given, such as $dy_1(t)/dt = f_1(t, y_1(t), y_2(t), \dots, y_n(t))$, $dy_2(t)/dt = f_2(t, y_1(t), y_2(t), \dots, y_n(t))$, \dots , $dy_n(t)/dt = f_n(t, y_1(t), y_2(t), \dots, y_n(t))$, the first-order increment functions are given as

$$k_1^{(1)} = f_1(t, y_1, y_2, \dots, y_n), \tag{12}$$

$$k_2^{(1)} = f_2(t, y_1, y_2, \dots, y_n), \tag{13}$$

•
•

$$k_n^{(1)} = f_n(t, y_1, y_2, \dots, y_n), \tag{14}$$

and the second-order increment functions as

$$k_1^{(2)} = f_1\left(t + \frac{h}{2}, y_1 + \frac{hk_1^{(1)}}{2}, y_2 + \frac{hk_2^{(1)}}{2}, \dots, y_n + \frac{hk_n^{(1)}}{2}\right), \tag{15}$$

$$k_2^{(2)} = f_2\left(t + \frac{h}{2}, y_1 + \frac{hk_1^{(1)}}{2}, y_2 + \frac{hk_2^{(1)}}{2}, \dots, y_n + \frac{hk_n^{(1)}}{2}\right), \tag{16}$$

•
•

$$k_n^{(2)} = f_n\left(t + \frac{h}{2}, y_1 + \frac{hk_1^{(1)}}{2}, y_2 + \frac{hk_2^{(1)}}{2}, \dots, y_n + \frac{hk_n^{(1)}}{2}\right), \tag{17}$$

and the third-order increment functions as

$$k_1^{(3)} = f_1\left(t + \frac{h}{2}, y_1 + \frac{hk_1^{(2)}}{2}, y_2 + \frac{hk_2^{(2)}}{2}, \dots, y_n + \frac{hk_n^{(2)}}{2}\right), \tag{18}$$

$$k_2^{(3)} = f_2\left(t + \frac{h}{2}, y_1 + \frac{hk_1^{(2)}}{2}, y_2 + \frac{hk_2^{(2)}}{2}, \dots, y_n + \frac{hk_n^{(2)}}{2}\right), \tag{19}$$

•
•

$$k_n^{(3)} = f_n\left(t + \frac{h}{2}, y_1 + \frac{hk_1^{(2)}}{2}, y_2 + \frac{hk_2^{(2)}}{2}, \dots, y_n + \frac{hk_n^{(2)}}{2}\right), \tag{20}$$

and the fourth-order increment functions as

$$k_1^{(4)} = f_1(t + h, y_1 + hk_1^{(3)}, y_2 + hk_2^{(3)}, \dots, y_n + hk_n^{(3)}), \tag{21}$$

$$k_2^{(4)} = f_2(t + h, y_1 + hk_1^{(3)}, y_2 + hk_2^{(3)}, \dots, y_n + hk_n^{(3)}), \tag{22}$$

$$\begin{aligned}
 & \bullet \\
 & \bullet \\
 & k_n^{(4)} = f_n(t+h, y_1 + hk_1^{(3)}, y_2 + hk_2^{(3)}, \bullet, \bullet, \bullet, y_n + hk_n^{(3)}). \tag{23}
 \end{aligned}$$

Here, h is the increment of t . The variables at $t + h$ are given as

$$y_1(t+h) = y_1(t) + \frac{1}{6}(k_1^{(1)} + 2k_1^{(2)} + 2k_1^{(3)} + k_1^{(4)}), \tag{24}$$

$$y_2(t+h) = y_2(t) + \frac{1}{6}(k_2^{(1)} + 2k_2^{(2)} + 2k_2^{(3)} + k_2^{(4)}), \tag{25}$$

$$\begin{aligned}
 & \bullet \\
 & \bullet \\
 & y_n(t+h) = y_n(t) + \frac{1}{6}(k_n^{(1)} + 2k_n^{(2)} + 2k_n^{(3)} + k_n^{(4)}). \tag{26}
 \end{aligned}$$

If the variables at a t are given, the numerical values at $t + h$ can be obtained from equations (24) – (26), then the values at $t + 2h$, at $t + 3h$, etc. by repeating the calculations.

2.3 Numerical Calculation of Charge Motion

For the charge motion in the x and y directions, the variables are $x(t)$, $y(t)$, $v_x(t)$, and $v_y(t)$, and the differential equations are equations (6), (7), (9), and (10). For the charge motion in the z direction, the variables are $z(t)$ and $v_z(t)$, and the differential equations are equations (8) and (11). Here, we will discuss the case of motion in the x - y plane only. We obtain the incremental functions for the charge motion

$$k_1^{(1)} = v_{x,j}, \tag{27}$$

$$k_2^{(1)} = v_{y,j}, \tag{28}$$

$$k_3^{(1)} = -c_1 v_{x,j} + c_3 E_x(t) + c_3 v_{y,j} B_z(t) - c_2 (x_j - x_{R0}), \tag{29}$$

$$k_4^{(1)} = -c_1 v_{y,j} + c_3 E_y(t) - c_3 v_{x,j} B_z(t) - c_2 (y_j - y_{R0}), \tag{30}$$

$$k_1^{(2)} = v_{x,j} + \frac{hk_3^{(1)}}{2}, \tag{31}$$

$$k_2^{(2)} = v_{y,j} + \frac{hk_4^{(1)}}{2}, \tag{32}$$

$$k_3^{(2)} = -c_1 \left(v_{x,j} + \frac{hk_3^{(1)}}{2} \right) + c_3 E_x \left(t + \frac{h}{2} \right) + c_3 \left(v_{y,j} + \frac{hk_4^{(1)}}{2} \right) B_z \left(t + \frac{h}{2} \right) - c_2 \left(x_j + \frac{hk_1^{(1)}}{2} - x_{R0} \right), \tag{33}$$

$$k_4^{(2)} = -c_1 \left(v_{x,j} + \frac{hk_4^{(1)}}{2} \right) + c_3 E_y \left(t + \frac{h}{2} \right) - c_3 \left(v_{x,j} + \frac{hk_3^{(1)}}{2} \right) B_z \left(t + \frac{h}{2} \right) - c_2 \left(y_j + \frac{hk_2^{(1)}}{2} - y_{R0} \right), \quad (34)$$

$$k_1^{(3)} = v_{x,j} + \frac{hk_3^{(2)}}{2}, \quad (35)$$

$$k_2^{(3)} = v_{y,j} + \frac{hk_4^{(2)}}{2}, \quad (36)$$

$$k_3^{(3)} = -c_1 \left(v_{x,j} + \frac{hk_3^{(2)}}{2} \right) + c_3 E_x \left(t + \frac{h}{2} \right) + c_3 \left(v_{y,j} + \frac{hk_4^{(2)}}{2} \right) B_z \left(t + \frac{h}{2} \right) - c_2 \left(x_j + \frac{hk_1^{(2)}}{2} - x_{R0} \right), \quad (37)$$

$$k_4^{(3)} = -c_1 \left(v_{y,j} + \frac{hk_4^{(2)}}{2} \right) + c_3 E_y \left(t + \frac{h}{2} \right) - c_3 \left(v_{x,j} + \frac{hk_3^{(2)}}{2} \right) B_z \left(t + \frac{h}{2} \right) - c_2 \left(y_j + \frac{hk_2^{(2)}}{2} - y_{R0} \right), \quad (38)$$

$$k_1^{(4)} = v_{x,j} + hk_3^{(3)}, \quad (39)$$

$$k_2^{(4)} = v_{y,j} + hk_4^{(3)}, \quad (40)$$

$$k_3^{(4)} = -c_1 \left(v_{x,j} + hk_3^{(3)} \right) + c_3 E_x \left(t + h \right) + c_3 \left(v_{y,j} + hk_4^{(3)} \right) B_z \left(t + h \right) - c_2 \left(x_j + hk_1^{(3)} - x_{R0} \right), \quad (41)$$

$$k_4^{(4)} = -c_1 \left(v_{y,j} + hk_4^{(3)} \right) + c_3 E_y \left(t + h \right) - c_3 \left(v_{x,j} + hk_3^{(3)} \right) B_z \left(t + h \right) - c_2 \left(y_j + hk_2^{(3)} - y_{R0} \right). \quad (42)$$

Ηερε, $\chi_1 = \alpha/\mu$, $\chi_2 = \beta/\mu$, ανδ $\chi_3 = \theta/\mu$. Τηε συβσχηριπ φ ρεπρεσεντς τηε κνωων παριαβλες
 ατ τ . Τηε υκνωων παριαβλες $\xi_{\varphi+1}$, $\psi_{\varphi+1}$, $\varpi_{\xi,\varphi+1}$, ανδ $\varpi_{\psi,\varphi+1}$ ατ $\tau + \eta$ αρε γιωεν ασ

$$x_{j+1} = x_j + \frac{1}{6} (k_1^{(1)} + 2k_1^{(2)} + 2k_1^{(3)} + k_1^{(4)}), \quad (43)$$

$$y_{j+1} = y_j + \frac{1}{6} (k_2^{(1)} + 2k_2^{(2)} + 2k_2^{(3)} + k_2^{(4)}), \quad (44)$$

$$v_{x,j+1} = v_{x,j} + \frac{1}{6} (k_3^{(1)} + 2k_3^{(2)} + 2k_3^{(3)} + k_3^{(4)}), \quad (45)$$

$$v_{y,j+1} = v_{y,j} + \frac{1}{6} (k_4^{(1)} + 2k_4^{(2)} + 2k_4^{(3)} + k_4^{(4)}). \quad (46)$$

2.4 Reflection at a Boundary

When the charge reflects at a wall, the perpendicular component of the velocity against the wall changes into the inverse value and the parallel component does not change. That is, v_y changes into $-v_y$ at x -plane and v_x changes into $-v_x$ at y -plane. In the case of the reflection at (x,y) on a cylindrical wall for z -direction, the perpendicular component of the velocity, v_τ , and the parallel component, v_p , are

$$v_T = v_x \frac{x-x_0}{R} + v_y \frac{y-y_0}{R}, \quad (47)$$

$$v_P = v_x \frac{y-y_0}{R} - v_y \frac{x-x_0}{R}. \quad (48)$$

Here, R and (x_0, y_0) are the radius and center of the cylinder, respectively. If $\sqrt{(x-x_0)^2 + (y-y_0)^2} \geq R$, v_T changes into $-v_T$, and the new velocities after the reflection are obtained as

$$v_x = (-v_T) \frac{x-x_0}{R} + v_P \frac{y-y_0}{R}, \quad (49)$$

$$v_y = (-v_T) \frac{y-y_0}{R} - v_P \frac{x-x_0}{R}. \quad (50)$$

3 PROGRAMMING

In a numerical calculation, values alternating with time, such as electric field and magnetic field are more conveniently expressed as cosine functions instead of sine functions, for example $E_x = E_{x0} \cos(2\pi f_E t)$ and $B_z = B_0 \cos(2\pi f_B t)$, for the calculation at $f_E = 0$ and $f_B = 0$. Here, f_E and f_B are frequencies of the electric and magnetic fields, respectively. If we use $E_x = E_{x0} \sin(2\pi f_E t)$ and $B_z = B_0 \sin(2\pi f_B t)$, then $E_x = 0$ at $f_E = 0$ and $B_z = 0$ at $f_B = 0$ despite the existence of direct electric and magnetic fields.

In our basic numerical calculation, nine text fields for coefficient of the resistance force, a , coefficient of the restoring Coulomb force, b , absolute values of E_x , E_y , and B_z , that are E_{x0} , E_{y0} and B_0 , frequencies of electric and magnetic fields, f_E and f_B , increment of time, h , and number of calculations, n , are set on the display. In addition them, more text fields are set for the motion in a boundary, such as the position and size of the boundary, for example, the radius and center of the cylinder, R and (x_0, y_0) . Values of a and b in the text-fields are normalized by q due to same effective order with electric and magnetic fields.

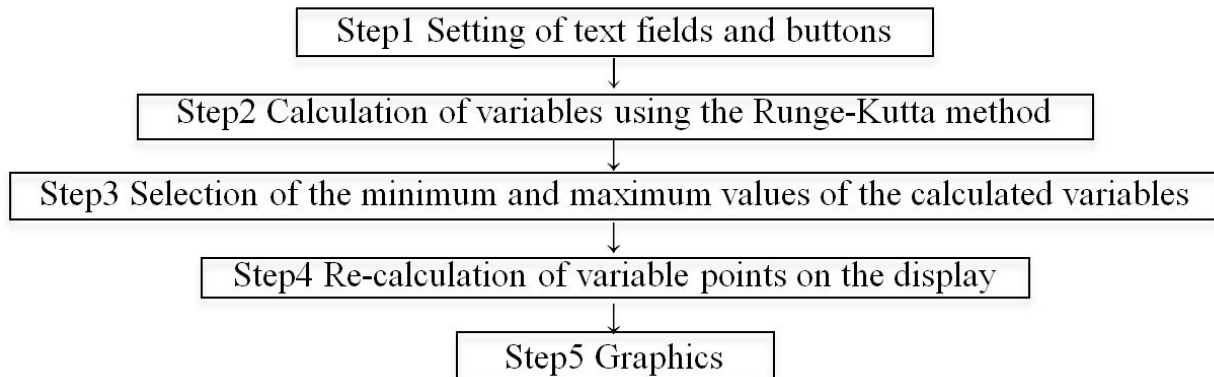
When the calculated results are presented on a display, the value of the y -direction is plotted on the lower part on the display; in other words, the y -direction on the display is opposite to the real y -direction. Therefore, to plot the point of the variables $(x(t), y(t))$ within the area between (X_{\min}, Y_{\min}) and (X_{\max}, Y_{\max}) on the display, and to plot the point (x_{\min}, y_{\max}) at (X_{\min}, Y_{\min}) , the points of the variables on the display, $x_D(t)$ and $y_D(t)$, should be re-calculated as follows:

$$x_D(t) = X_{\min} + (X_{\max} - X_{\min}) \frac{x(t) - x_{\min}}{x_{\max} - x_{\min}}, \quad (51)$$

$$y_D(t) = Y_{\min} + (Y_{\max} - Y_{\min}) \frac{y_{\max} - y(t)}{y_{\max} - y_{\min}}. \quad (52)$$

Here, the subscripts $_{\min}$ and $_{\max}$ represent the minimum and maximum values, respectively. In this case, the points x_{\min} and x_{\max} are plotted at X_{\min} and X_{\max} , respectively, and the points y_{\min} and y_{\max} are plotted at Y_{\max} and Y_{\min} , respectively. Therefore, the scale for x -direction, $(x_{\max} - x_{\min})/(X_{\max} - X_{\min})$ is different from that for y -direction, $(y_{\max} - y_{\min})/(Y_{\max} - Y_{\min})$, on the display. The charge motion can be plotted as a same scale for x and y directions by using their smaller value for $(X_{\max} - X_{\min})$ or $(Y_{\max} - Y_{\min})$ and using their larger value for $(x_{\max} - x_{\min})$ or $(y_{\max} - y_{\min})$ in Eqs. (51) and (52).

The main flow of the programming is shown below.



4 RESULTS

The text fields are immediately presented on the display after the execution of the program by the applet viewer form of Java, and the calculation is initiated by clicking the start button after inputting values in the text fields. The charge motion is plotted immediately after the completion of the calculation. The time needed to display the charge motion after clicking the start button is usually less than several seconds depending on the number of calculations and the performance of computer. By changing the values in the text fields and clicking again the start button, new charge motion can be obtained immediately.

4.1 Charge Motion in No-Boundary

A typical ion motion in which the forces of the resistance, electric and magnetic fields, and restoring are all effective is shown in Fig. 1. The figure is shown as an image on the display. By increasing the value in the text field of B_0 by a factor of 5, a new locus in which the motion is strongly affected by the magnetic field, such as in Larmor motion, can be immediately obtained, as shown in Fig. 2. By increasing the value in the text field of b by a factor of 10, a new locus in which the motion is strongly affected by the restoration can also be immediately obtained, as shown in Fig. 3. By increasing the value in the text field of a , E_{x0} , or E_{y0} by a factor of 10, a new locus in which the motion is strongly affected by the resistance or each electric field can be immediately obtained also. The point of start and stop, the values of the motion range for x - and y -directions, the final time at the stop point, and the initial velocity of the charge are also shown on the display. By changing the values in the text fields and clicking again the start

button, the change of the specific motion affected by each forces are recognized easily and correctly as an image of the locus of the motion on the display.

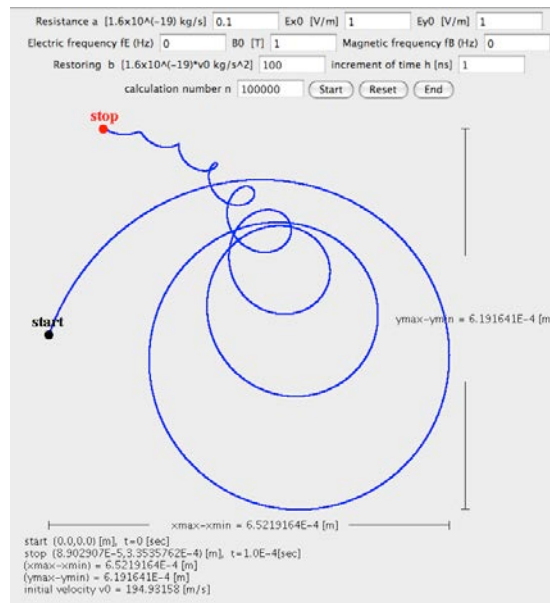


Figure 1. Typical ion motion in which all forces are effective. The values used for the calculation are shown in the text fields. The distance, final time, and initial velocity are also shown in the figure.

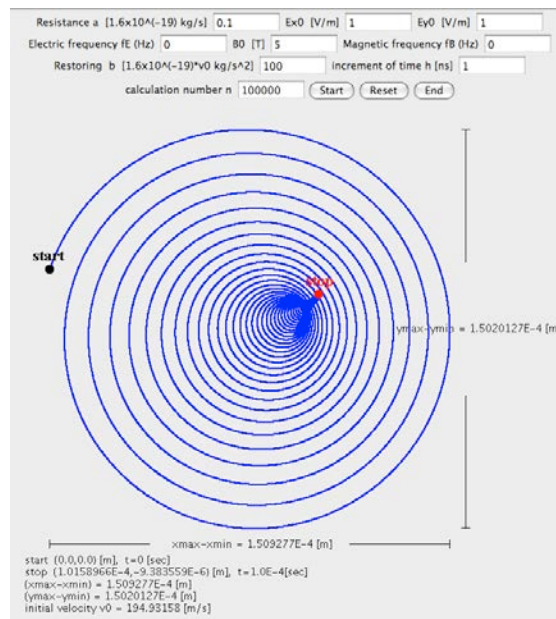


Figure 2. Updated motion affected strongly by the magnetic field B_0 after increasing by a factor of 5 relative to that in Fig. 1.

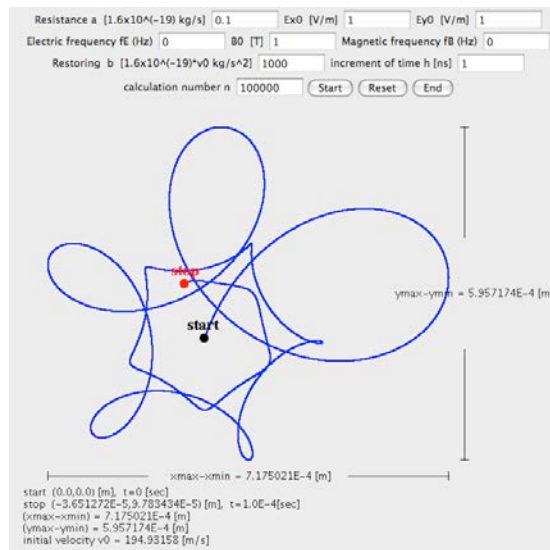


Figure 3. Updated motion affected strongly by the restoration b after increasing by a factor of 10 relative to that in Fig. 1.

4.2 Charge Motion in Quadrilateral Boundary

A typical ion motion in a quadrilateral boundary, which size is 10 cm x 5 cm, is shown in Fig. 4. The reflection at the wall is clearly shown as an image on the display. By changing the values in the text fields, charge motions in the different size of the boundary under the different effect of each forces can be shown immediately and correctly as images on the display.

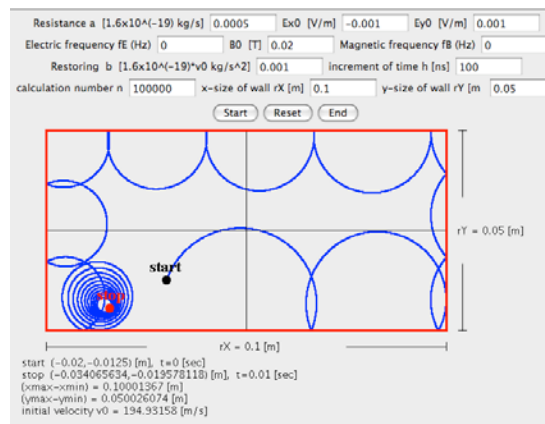


Figure 4. Typical ion motion in a quadrilateral boundary, 10 cm x 5 cm.

4.3 Charge Motion in Cylindrical Boundary

A typical ion motion in a cylindrical boundary for z-direction, which radius is 2.5 cm, is shown in Fig. 5. The values in the text fields except the boundary condition, that is the effects of each forces, are same as that in Fig. 4. The reflection at the cylindrical wall is clearly shown as an image on the display. By changing the values in the text fields, charge motions in the different size of the cylindrical boundary under the different effect of each forces can be also shown immediately and correctly as images on the display.

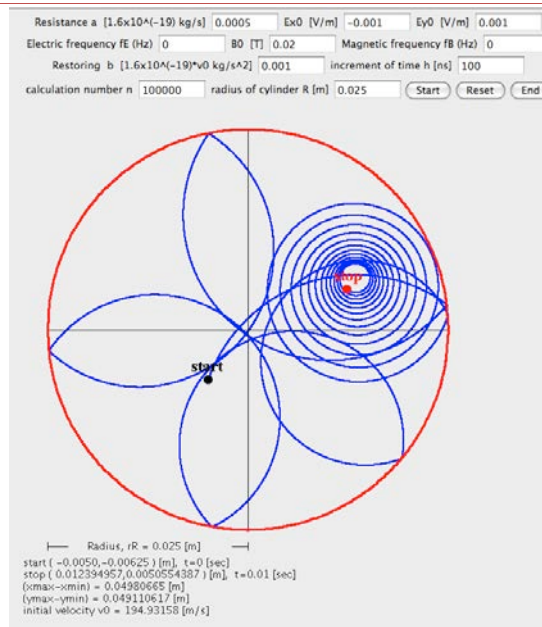


Figure 5. Typical ion motion in a cylindrical boundary, which radius is 2.5 cm. The values are same as that in Fig. 4 except the boundary condition.

4.4 A sample of Program

One example of the program used here to get Fig. 5 is shown below. The function of the main part of program is written as a comment line.

```

/* Charge motion in cylindrical wall 2012.01, 2014.01 M. Morooka */
/*<applet code="IonAIVP30.class" width=700 height=800></applet>*/
import java.applet.Applet;
import java.awt.*;
import java.awt.event.*;
public class IonAIVP30 extends Applet implements ActionListener{
    TextField txt1,txt2,txt3,txt4,txt5,txt6,txt7,txt8,txt9,txt10;
    Label lb1,lb2,lb3,lb4,lb5,lb6,lb7,lb8,lb9,lb10;
    Button btn1,btn2,btn3;
    String moji;
    double a,ex0,ey0,fE,b0,fB,b,h,rR;
    int n;
    public void init(){
        lb1=new Label("Resistance a [1.6x10-19 kg/s]");
        add(lb1);
        txt1=new TextField(8);
        add(txt1);
        lb2=new Label("Ex0 [V/m]");
        add(lb2);
        txt2=new TextField(8);
        add(txt2);
        lb3=new Label("Ey0 [V/m]");
        add(lb3);
        txt3=new TextField(8);
        add(txt3);
    }
}

```

```

lb4=new Label("Electric frequency fE (Hz)");
add(lb4);
txt4=new TextField(8);
add(txt4);
lb5=new Label("B0 [T]");
add(lb5);
txt5=new TextField(8);
add(txt5);
lb6=new Label("Magnetic frequency fB (Hz)");
add(lb6);
txt6=new TextField(8);
add(txt6);
lb7=new Label("Restoring b [1.6x10-19*v0 kg/s2]");
add(lb7);
txt7=new TextField(8);
add(txt7);
lb8=new Label("increment of time h [ns]");
add(lb8);
txt8=new TextField(8);
add(txt8);
lb9=new Label("calculation number n");
add(lb9);
txt9=new TextField(8);
add(txt9);
lb10=new Label("radius of cylinder R [m]");
add(lb10);
txt10=new TextField(8);
add(txt10);
btn1=new Button("Start");
btn1.addActionListener(this);
add(btn1);
btn2=new Button("Reset");
btn2.addActionListener(this);
add(btn2);
btn3=new Button("End");
btn3.addActionListener(this);
add(btn3);
}
public void actionPerformed(ActionEvent e){
    moji=e.getActionCommand();
    repaint();
}
public void paint(Graphics g){
    if(moji=="Start"){
        lb1.setText("Resistance a [1.6x10-19 kg/s]");
        lb2.setText("Ex0 [V/m]");
        lb3.setText("Ey0 [V/m]");
        lb4.setText("Electric frequency fE (Hz)");
        lb5.setText("B0 [T]");
        lb6.setText("Magnetic frequency fB (Hz)");
        lb7.setText("Restoring b [1.6x10-19 *v0 kg/s2]");
        lb8.setText("increment of time h [ns]");
        lb9.setText("calculation number n");
    }
}

```

```
lb10.setText("radius of cylinder R [m]");
try{
    a=Double.parseDouble(txt1.getText());
    ex0=Double.parseDouble(txt2.getText());
    ey0=Double.parseDouble(txt3.getText());
    fE=Double.parseDouble(txt4.getText());
    b0=Double.parseDouble(txt5.getText());
    fB=Double.parseDouble(txt6.getText());
    b=Double.parseDouble(txt7.getText());
    h=Double.parseDouble(txt8.getText());
    n=Integer.parseInt(txt9.getText());
    rR=Double.parseDouble(txt10.getText());
}
catch(NumberFormatException ex){
    lb1.setText(" error");
}
double[] t=new double[n+2];
double[] x=new double[n+2];
double[] vx=new double[n+2];
double[] y=new double[n+2];
double[] vy=new double[n+2];

//constants
double q,z,m,m0;
a=a*1.6e-19;
b=b*1.6e-19;
h=0.00000001*h;
z=1.0;
q=z*1.6e-19;//charge q=z x 1.6e(-19) [C]
m=9.11e-31;//mass of electron [kg]
m0=197.0;//mass No. of ion (Gold)
m=m0*1.66e-27;//mass of atom and ion
double tmax;
tmax = h*(double)n;// final time (sec)
double v0,temp;
temp=27.0;// temperature [C]
v0=Math.sqrt(3.0*1.38e-23*(273.15+temp)/m);// thermal velocity [m/s]
b=b*v0;
double c1,c2,eEx0,eEy0,bB0;
c1=a/m;
c2=b/m;
eEx0=ex0*q/m;
eEy0=ey0*q/m;
bB0=b0*q/m;

//center of cylinder (x0,y0), minimum (xWmin,yWmin) and maximum (xWmax,yWmax) points of cylinder
double x0,y0,xWmin,xWmax,yWmin,yWmax,r; // r: distance from the center = sqrt.((x-x0)^2+(y-
y0)^2)

x0=0.0;
y0=0.0;
xWmin=x0-rR;
xWmax=x0+rR;
yWmin=y0-rR;
yWmax=y0+rR;
```

```

double vT,vP; //vT:perpendicular component of v, vP:parallel component of v for wall
//initial conditions
t[0]=0.0;
x[0]=x0-0.2*rR; // sqrt.((x[0]-x0)*(x[0]-x0)+(y[0]-y0)*(y[0]-y0)) < rR
y[0]=y0-0.25*rR; // sqrt.((x[0]-x0)*(x[0]-x0)+(y[0]-y0)*(y[0]-y0)) < rR
vx[0]=v0*1.0/3.0; // [m/s]
vy[0]=Math.sqrt(v0*v0-vx[0]*vx[0]);
double xR0,yR0; // center of restoring force (xR0,yR0)
xR0=x0;
yR0=y0;
//Runge-Kutta method
double k1,k2,k3,k4,l1,l2,l3,l4,m1,m2,m3,m4,n1,n2,n3,n4;
int i;
for(i=0;i<=n;++i){
    k1=vx[i];
    l1=-
c1*vx[i]+eEx0*Math.cos(2.0*Math.PI*fE*t[i])+bB0*vy[i]*Math.cos(2.0*Math.PI*fB*t[i])-c2*(x[i]-xR0);
    m1=vy[i];
    n1=-c1*vy[i]+eEy0*Math.cos(2.0*Math.PI*fE*t[i])-
bB0*vx[i]*Math.cos(2.0*Math.PI*fB*t[i])-c2*(y[i]-yR0);
    k2=vx[i]+h/2.0*k1;
    l2=-
c1*(vx[i]+h/2.0*k1)+eEx0*Math.cos(2.0*Math.PI*fE*(t[i]+h/2.0))+bB0*(vy[i]+h/2.0*n1)*Math.cos(2.0*Math.PI*fB*(t[i]+h/2.0))-
c2*(x[i]+h/2.0*k1-xR0);
    m2=vy[i]+h/2.0*n1;
    n2=-c1*(vy[i]+h/2.0*n1)+eEy0*Math.cos(2.0*Math.PI*fE*(t[i]+h/2.0))-
bB0*(vx[i]+h/2.0*k1)*Math.cos(2.0*Math.PI*fB*(t[i]+h/2.0))-c2*(y[i]+h/2.0*m1-yR0);
    k3=vx[i]+h/2.0*k2;
    l3=-
c1*(vx[i]+h/2.0*k2)+eEx0*Math.cos(2.0*Math.PI*fE*(t[i]+h/2.0))+bB0*(vy[i]+h/2.0*n2)*Math.cos(2.0*Math.PI*fB*(t[i]+h/2.0))-
c2*(x[i]+h/2.0*k2-xR0);
    m3=vy[i]+h/2.0*n2;
    n3=-c1*(vy[i]+h/2.0*n2)+eEy0*Math.cos(2.0*Math.PI*fE*(t[i]+h/2.0))-
bB0*(vx[i]+h/2.0*k2)*Math.cos(2.0*Math.PI*fB*(t[i]+h/2.0))-c2*(y[i]+h/2.0*m2-yR0);
    k4=vx[i]+h*k3;
    l4=-
c1*(vx[i]+h*k3)+eEx0*Math.cos(2.0*Math.PI*fE*(t[i]+h))+bB0*(vy[i]+h*n3)*Math.cos(2.0*Math.PI*fB*(t[i]+h))-c2*(x[i]+h*k3-
xR0);
    m4=vy[i]+h*n3;
    n4=-c1*(vy[i]+h*n3)+eEy0*Math.cos(2.0*Math.PI*fE*(t[i]+h))-
bB0*(vx[i]+h*k3)*Math.cos(2.0*Math.PI*fB*(t[i]+h))-c2*(y[i]+h*m3-yR0);
    t[i+1]=t[i]+h;
    x[i+1]=x[i]+h/6.0*(k1+2.0*k2+2.0*k3+k4);
    vx[i+1]=vx[i]+h/6.0*(l1+2.0*l2+2.0*l3+l4);
    y[i+1]=y[i]+h/6.0*(m1+2.0*m2+2.0*m3+m4);
    vy[i+1]=vy[i]+h/6.0*(n1+2.0*n2+2.0*n3+n4);
    r = Math.sqrt((x[i+1]-x0)*(x[i+1]-x0)+(y[i+1]-y0)*(y[i+1]-y0));

    if(r>=rR){
        vT = (x[i+1]-x0)/rR*vx[i+1]+(y[i+1]-y0)/rR*vy[i+1];
        vP = (y[i+1]-y0)/rR*vx[i+1]-(x[i+1]-x0)/rR*vy[i+1];
        vT=-vT;
        vx[i+1] = (x[i+1]-x0)/rR*vT+(y[i+1]-y0)/rR*vP;
    }
}

```

```
vy[i+1] = (y[i+1]-y0)/rR*vT-(x[i+1]-x0)/rR*vP;
    }
}
//maximum and minimum values of x[i] and y[i]
double xmin,xmax,ymin,ymax;
xmin=x[0];
xmax=x[0];
ymin=y[0];
ymax=y[0];
for(i=0;i<=n;++i){
    xmax=Math.max(x[i],xmax);//maximum of x
    xmin=Math.min(x[i],xmin);//minimum of x
    ymax=Math.max(y[i],ymax);//maximum of y
    ymin=Math.min(y[i],ymin);//minimum of y
}
// print range on display; from (xDmin,yDmin) to (xDmax,yDmax)
int xDmin,xDmax,yDmin,yDmax;
xDmin=50;
xDmax=550;
yDmin=150;
yDmax=yDmin+(xDmax-xDmin);
// point of cylinder on display
double xDa,yDa;
//center (x0,y0) of cylinder
int x0D,y0D;
xDa=(double)xDmin+(double)Math.min((xDmax-xDmin),(yDmax-yDmin))*(x0-xWmin)/(2.0*rR);
yDa=(double)yDmin+(double)Math.min((xDmax-xDmin),(yDmax-yDmin))*(yWmax-y0)/(2.0*rR);
x0D=(int)xDa;
y0D=(int)yDa;
// point of cylinder
int iwmax;
iwmax = 200;
int[] xDw=new int[iwmax+2];// point of x of cylinder
int[] ypDw=new int[iwmax+2];// point of +y of cylinder
int[] ynDw=new int[iwmax+2];// point of -y of cylinder
double xw,xDwa,ypw,ynw,ypDwa,ynDwa;
for(i=0;i<=iwmax;++i){
    xw=xWmin+(xWmax-xWmin)*(double)i/(double)iwmax;
    xDwa=(double)xDmin+(double)(xDmax-xDmin)*(xw-xWmin)/(xWmax-xWmin);
    xDw[i]=(int)xDwa;
    ypw=y0+Math.sqrt(rR*rR-(xw-x0)*(xw-x0));
    ynw=y0-Math.sqrt(rR*rR-(xw-x0)*(xw-x0));
    ypDwa=(double)yDmin+(double)(yDmax-yDmin)*(yWmax-ypw)/(yWmax-yWmin);
    ypDw[i]=(int)ypDwa;
    ynDwa=(double)yDmin+(double)(yDmax-yDmin)*(yWmax-ynw)/(yWmax-yWmin);
    ynDw[i]=(int)ynDwa;
}
// minimum (xWmin,yWmin) and maximum (xWmax,yWmax) of cylinder
int xWminD,yWminD,xWmaxD,yWmaxD;
xDa=(double)xDmin+(double)Math.min((xDmax-xDmin),(yDmax-yDmin))*(xWmin-
xWmin)/Math.max(xWmax-xWmin,yWmax-yWmin);
xWminD=(int)xDa;
```

```

        yDa=(double)yDmin+(double)Math.min((xDmax-xDmin),(yDmax-yDmin))*(yWmax-
yWmin)/Math.max(xWmax-xWmin,yWmax-yWmin);
        yWminD=(int)yDa;
        xDa=(double)xDmin+(double)Math.min((xDmax-xDmin),(yDmax-yDmin))*(xWmax-
xWmin)/Math.max(xWmax-xWmin,yWmax-yWmin);
        xWmaxD=(int)xDa;
        yDa=(double)yDmin+(double)Math.min((xDmax-xDmin),(yDmax-yDmin))*(yWmax-
yWmax)/Math.max(xWmax-xWmin,yWmax-yWmin);
        yWmaxD=(int)yDa;
        // point of x[i] and y[i] on display (xDmin at x[i]=xWmin and xDmax at x[i]=xWmax, yDmin at y[i]=yWmax and
yDmax at y[i]=yWmin)
        int[] xD=new int[n+2]; // point of x[i] on display
        int[] yD=new int[n+2]; // point of y[i] on display
        for(i=0;i<=n;++i){
            xDa=(double)xDmin+(double)Math.min((xDmax-xDmin),(yDmax-yDmin))*(x[i]-
xWmin)/Math.max(xWmax-xWmin,yWmax-yWmin);
            yDa=(double)yDmin+(double)Math.min((xDmax-xDmin),(yDmax-yDmin))*(yWmax-
y[i])/Math.max(xWmax-xWmin,yWmax-yWmin);
            xD[i]=(int)xDa;
            yD[i]=(int)yDa;
        }
        // point of xmin, xmax, ymin, and ymax on display
        int xminD,yminD,xmaxD,ymaxD;
        xDa=(double)xDmin+(double)Math.min((xDmax-xDmin),(yDmax-yDmin))*(xmin-
xWmin)/Math.max(xWmax-xWmin,yWmax-yWmin);
        yDa=(double)yDmin+(double)Math.min((xDmax-xDmin),(yDmax-yDmin))*(xWmax-
ymin)/Math.max(xWmax-xWmin,yWmax-yWmin);
        xminD=(int)xDa;
        yminD=(int)yDa;
        xDa=(double)xDmin+(double)Math.min((xDmax-xDmin),(yDmax-yDmin))*(xmax-
xWmin)/Math.max(xWmax-xWmin,yWmax-yWmin);
        yDa=(double)yDmin+(double)Math.min((xDmax-xDmin),(yDmax-yDmin))*(xWmax-
ymax)/Math.max(xWmax-xWmin,yWmax-yWmin);
        xmaxD=(int)xDa;
        ymaxD=(int)yDa;
        // print of start and stop points and motion range
        double xW,yW;
        xW=xmax-xmin;//[m]
        yW=ymax-ymin;//[m]
        float startx,starty,stopx,stopy,rRf,xWf,yWf;
        startx=(float)x[0];
        starty=(float)y[0];
        stopx=(float)x[n];
        stopy=(float)y[n];
        rRf=(float)rR;
        xWf=(float)xW;
        yWf=(float)yW;
        String sstartx,sstarty,sstopx,sstopy,srR,sxW,syW;
        sstartx=Float.toString(startx);
        sstarty=Float.toString(starty);
        sstopx=Float.toString(stopx);
        sstopy=Float.toString(stopy);
        srR=Float.toString(rRf);

```

```
    sxW=Float.toString(xWf);
    syW=Float.toString(yWf);
    float tmaxf;
    tmaxf=(float)tmax;
    String stmax;
    stmax = Float.toString(tmaxf);
    float v0f;
    v0f=(float)v0;
    String sv0;
    sv0 = Float.toString(v0f);
    g.drawString("Radius, rR = "+srR+" [m]",xWminD+50,yWminD+25);
    g.drawLine(xWminD,yWminD+20-5,xWminD,yWminD+20+5);
    g.drawLine(x0D,yWminD+20-5,x0D,yWminD+20+5);
    g.drawLine(xWminD,yWminD+20,xWminD+25,yWminD+20);
    g.drawLine(x0D-20,yWminD+20,x0D,yWminD+20);
    g.drawString("start ( "+sstartx+", "+sstarty+" ) [m], t=0 [sec]",xWminD-30,yWminD+45);
    g.drawString("stop ( "+sstopx+", "+sstopy+" ) [m], t="+stmax+" [sec]",xWminD-30,yWminD+60);
    g.drawString("(xmax-xmin) = "+sxW+" [m]",xWminD-30,yWminD+75);
    g.drawString("(ymax-ymin) = "+syW+" [m]",xWminD-30,yWminD+90);
    g.drawString("initial velocity v0 = "+sv0+" [m/s]",xWminD-30,yWminD+105);
// charge motion on display
    for(i=0;i<=n;++i){
        try{
            g.setColor(Color.blue);
            g.fillOval(xD[i],yD[i],1,1);
        }
        catch(ArrayIndexOutOfBoundsException ex){
        }
    }
    g.setColor(Color.black);
    g.drawLine(xWminD,(yWmaxD+yWminD)/2,xDmax,(yWmaxD+yWminD)/2);
    g.drawLine((xWminD+xWmaxD)/2,yWmaxD,(xWminD+xWmaxD)/2,yWminD);
// print of wall on display
    g.setColor(Color.red);
    BasicStroke stroke;
    Graphics2D g2 = (Graphics2D)g;
    stroke = new BasicStroke(2.0f); //thickness of wall
    g2.setStroke(stroke);
    for(i=0;i<=iwmax-1;++i){
        try{
            g2.drawLine(xDw[i],ypDw[i],xDw[i+1],ypDw[i+1]);
            g2.drawLine(xDw[i],ynDw[i],xDw[i+1],ynDw[i+1]);
        }
        catch(ArrayIndexOutOfBoundsException ex){
        }
    }
//selection of font
    try {
        Font f1=new Font("TIMES",Font.BOLD,20);
        g.setFont (f1);
        g.setColor(Color.black);
        g.fillOval(xD[0]-5,yD[0]-5,10,10);
    }
```

```

        g.drawString("start",xD[0]-20,yD[0]-10);
        g.setColor(Color.red);
        g.fillOval(xD[n]-5,yD[n]-5,10,10);
        g.drawString("stop",xD[n]-15,yD[n]-10);
    }
    catch (ArrayIndexOutOfBoundsException ex){
    }
}
else if(moji=="End"){
    System.exit(0);
}
if(moji=="Reset"){
    g.clearRect(0,0,701,500);
}
}
}
}

```

5 DISCUSSION

The accuracy of the calculation by this program depends on the value of the time increment, h . If we use a too large h , the calculation is not done accurately and the locus of the motion is shown non-continuously as shown in Fig. 6. In this case, the reflection at the wall slips out of the wall place, and the calculated point of the charge deviates more from the accurate point with increasing the time. The calculation is more accurate with use of smaller h , but a larger number of calculation, that is a longer calculation time, is needed to get a characteristic motion. It is better to chose the largest h value by tentative calculation with relative small calculation number n . Here, we used fourth-order Runge-Kutta method to solve numerically the ordinary differential equations, but the results such as Figs. 1-5 were completely same as that obtained by the improved Runge-Kutta-Gill method [2] by using an appropriate value of h .

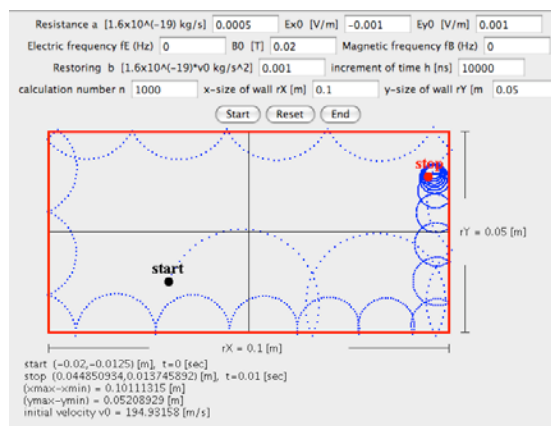


Figure 6. A sample of an non-accurate calculation using a too large h .

In Figure 6, the values used for the calculation are same as that in Fig. 4, except h and n . The final time at the stop point, 0.05 sec, is also same as that in Fig. 4, but the stop point deviates largely from that in Fig. 4. The reflection at the wall slips out of the wall place, and the calculated point deviates more from that in Fig. 4 with increasing the time.

By plotting the change of the velocity with time in addition to the charge locus, as shown in Fig. 7, the charge motion can be understood more clearly in relation to the velocity, such as, the decrease of Larmor radius with time is caused by the decrease of the velocity due to the resistance force.

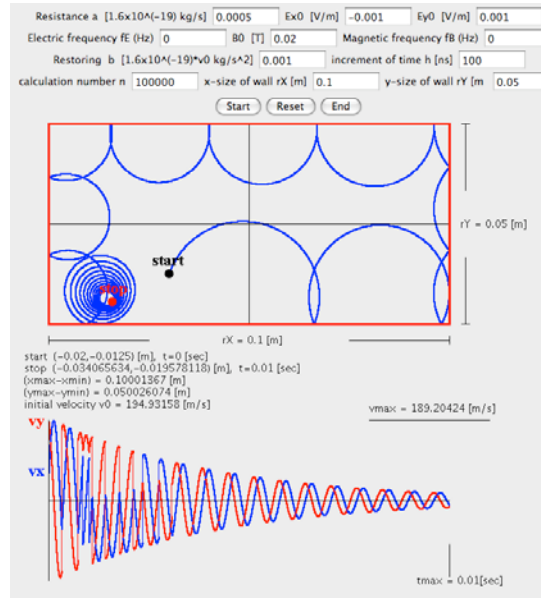


Figure 7. Change of the velocity with the time plotted together with the charge motion in Fig. 4. It is clearly understood that the decrease of Larmor radius is caused by the decrease of the velocity.

The values in the text fields are used here from a point of view such that each force is effective or not effective. The used values for the electric and magnetic fields are reasonable, but that for the resistance and restoring change very much under the circumstances of the charge motion, for example, the value of resistance force, a , is very large in a solid but nearly equal to 0 in a vacuum. In this program, the values are used with no-considering actual media for the charge motion. In this view point, the charge shows a very mysterious motion under a particular condition, as shown in Fig. 8.

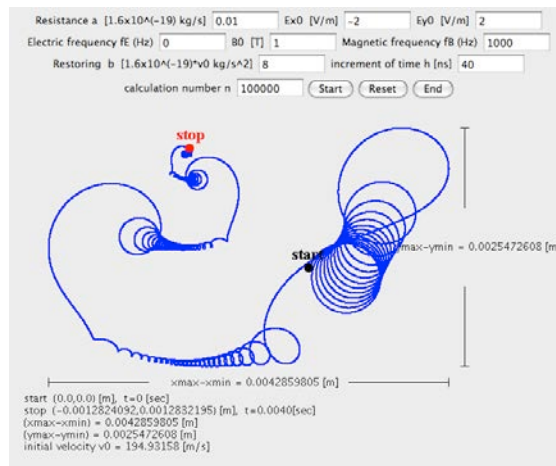


Figure 8. A mysterious motion of charge under a particular condition.

6 CONCLUSION

Java programs in a GUI environment have been developed for the simulations of charge motion in electric and magnetic fields. The values of the selected parameters for the numerical calculation are set using text fields on the display, and the calculation is initiated by clicking the start button after inputting these values. The calculated results are plotted immediately after the completion of the calculation as a locus of the charge motion on the display. By changing the values in the text fields and clicking again the start button, new results can be displayed immediately. The simulations of the charge motion depending on each force in the electric and magnetic fields can be obtained easily and accurately as a locus of the motion on the display. The time needed to simulate is very short and less than several seconds using an usual personal computer. These Java programs are useful for an image learning of the charge motion in education applications because of their ability to quickly provide accurate depictions of fundamentals of charge motion.

This Java program can be applied for rapidly and accurately image learning for the phenomena expressed by ordinary differential equations due to use Runge-Kutta method. By using Crank-Nicolson's implicit method and Gauss-Seidel's iteration method [1], these Java simulations are also useful in education applications for rapidly and accurately image learning for the more complicated phenomena expressed by partial differential equations such as diffusions of atoms and propagations of heat and wave, etc.

REFERENCES

- [1]. M. Morooka, Journal of Software Engineering and Applications, vol. 5 No. 10, pp. 764-776, (2012).
- [2]. S. Gill, Proc. Cambridge Phil. Soc. , vol. 47, 96-108, (1951).

A novel Approach to System Security using Derived Odor Keys with Weight Elimination Neural Algorithm (DOK-WENA)

Mahmoud Z. Iskandarani

Faculty of Science and Information Technology, Al-Zaytoonah University of Jordan

m.iskandarani@hotmail.com

ABSTRACT

A novel security technique for network and data communication applications that makes use of odors as password generators is developed and tested. The developed system employs odor keys derived from an original key together with the original key to allow access to systems and networks. The used key combinations are initially unknown to the user, and if detected while in the transmission process, there is no way of being able to be emulated.

The uniqueness of the developed system is that it is not necessary for an odor key to be an exact replica of the original, but to be derived from the original. This is a chemical encryption and encoding as the right key will not be detected by anyone since it is a derived version and not a match. Genetic Algorithm is used to emulate the chemical derivation and to make up for any margin of odor detection error and sensors tolerances.

Keywords: Genetic Algorithm, Olfactory, Odor Sensor, Software, Neural, Algorithm, Security.

1 INTRODUCTION

The selective application of technological and related procedural safeguards is an important responsibility of every organization in providing adequate security to its electronic data systems. Protection of data during transmission or while in storage may be necessary to maintain the confidentiality and integrity of the information represented by the data. Attacks against computer systems and networks are becoming more sophisticated, using new techniques and technologies with increased global interconnectivity, and Internet communication, system security has become a necessity.

Organizations must protect their systems from intruders and other forms of attacks. Such protection must detect anomalous patterns while monitoring normal computer programs and networks. The need for authentication is well understood and is concerned with well-equipped attackers who have access to processes and who merely need a starting point to be considered successful. This conservative approach is now finding its way into standards and specifications.

Network and device security is utilized in various applications and environments. The specific utilization and various implementations will be based on many factors particular to the computer system and its associated components. In general, password security is used to protect data access while it is stored in a medium vulnerable to physical theft or technical intrusion (e.g., hacker attacks, where the key must be maintained and accessible for the duration of the storage period).

A security technique for network data communication applications that makes use of odors as password generators, might adopt both personal and synthetic odors. Such a system not only use such odors as an access control identifier, but also the converted signals obtained from them can be implanted and added randomly to a data file for extra security [1-5].

In this paper, a novel algorithm that employs odors as password and encryption keys is developed within a hierarchical layered architecture, which maps out odor features in a lower (uncertain) and upper (certain) bands, thus resulting in finding the correct access and/or decryption key [6-10].

2 MATERIALS AND METHODS

The used system comprises a combinations of tuned sensors coupled with sophisticated information processing. Each odorant or volatile compound presented to the sensor array produces a signature or characteristic pattern of the odorant.

By presenting many different odorants to the sensor array, a database of signatures is built up. This database of odorant signatures is then used to build odor recognition system. The goal of this process is to configure the recognition system to produce unique classifications or clustering's of each odorant so that an automated identification can be implemented.

When the sensor array is exposed to odor mixtures, containing the molecules to which the devices are sensitive, different response patterns will be created. By detecting odor patterns the system would then be able to classify a vapor mixture and perform security actions as required. Different levels of security exist, depending number of odors required as keys to generate a specific password.

Generally speaking, the odor system collects a sample and routes it through a sensor array where the presence of certain substances are detected. The concentrations of these substances are recorded. The combination of tuned sensors coupled with sophisticated information processing makes the recognition system a powerful instrument for odor applications. Each odorant presented to the sensor array produces a signature or characteristic pattern of the odorant.

Our Multi-Sensor array system employs MOS- based sensors with an SnO₂ metal-oxide semiconducting film coated onto a ceramic substrate Each device also contains a heating element. Oxygen from the air is dissolved in the semiconductors' lattice, setting its electrical resistance to a background level (stable when at equilibrium). During the measurement, the

volatile molecules (mainly non-polar) are adsorbed at the surface of the semiconductor where they react (oxidation/reduction) with the dissolved oxygen species causing a further modification of the resistance (or conductivity) of the device. This last change is taken as the response of the system to that particular sample.

By presenting many different odorants to the sensor array, a database of signatures is built up. This database of odorant signatures is then used to build the odor recognition system. The goal of this process is to train or configure the recognition system to produce unique classifications or clustering's of each odorant so that an automated identification can be implemented. During testing operation, a chemical vapor or odor is blown over the sensor array, the sensor signals are digitized and fed into the computer, with intelligent classification algorithm used to identify the odor and its relation to others odors.

Consider a classification problem where a test pattern is to be assigned to a class label (Odor Class), OC where:

$$OC \in \{OC_1, OC_2, \dots, OC_n\} \quad (1)$$

n: Number of possible classes.

Measuring the test pattern is carried out by means of M sensors. Assume that the observations on the test pattern from the i th sensor are represented by the feature vector S_i ($i=1\dots m$), which can be assumed a row vector. The objective now is to map S_i ($i=1\dots m$) to a pattern class OC.

S_i can be considered an estimation of the test pattern's characters using the i^{th} sensor. Different sensors probably give different measurements due to the factors of sensor type, position, sensitivity, while measuring same odor and describing the same test pattern. So there must be some kind of inherent relationship among them.

We define S_0 as the Center-Feature (CF) which is the default and intrinsic response of the test pattern's characters, which is a priori feature. Hence, there is a functional relationship T_i between S_0 and S_i :

$$S_i = T_i(S_0) \quad (2)$$

T_i : Transformation Function (TF).

Using CF and TF, the observation set $\{S_1, \dots, S_m\}$ can be re-written as:

$$\{T_1(S_0), \dots, T_m(S_0)\} \quad (3)$$

which is the mapping from the observation set to the pattern class label OC.

3 RESULTS AND DISCUSSION

Table 1 shows the obtained results from exposing an odor sensor array unit to six different types of odors where the presence of certain substances is detected. The concentrations of these substances are counted and recorded as digital pulses. Each odorant presented to the sensor array produces a signature or characteristic pattern of the odorant.

Table 1: Sensor Array Pulse Output

Time(Sec)	Number of Response Pulses (N) for Six Odor Samples					
t	k ₁	k ₂	k ₃	k ₄	k ₅	k ₆
10	119	19	8	13	13	21
20	145	25	10	18	17	40
30	160	29	11	21	21	50
40	169	30	11	24	22	54
50	174	32	12	26	23	55
60	178	34	13	27	24	56

Each sensor response signal rises from its base as the sensor detects the presence of a particular odor. This means an unstable rising function of signal amplitude for a certain period of time followed by a stable and constant value for a second period of time. Such behavior would not be obvious from the sensor readings and will not show which key is the one derived from the original key that can be used as a password to the intended system [11-15].

For the system to only accept the correct odor key, which is also encrypted within the signal readings as the main, master odor key is not emulated in an opening key but the opening odorant key is derived from the master key composition, and hence, the output readings for any odorant key will not be equal to the original master key. This is a new way of hiding the key [16-20].

To uncover the correct password odorant key, all represented keys are processed using equations 4 and 5 as part of the mapping process into lower and upper bounding parts as shown in Tables 2-6.

$$Odor_{code\ match}(t) = XOR(k_i, k_j) = const. \dots \quad (4)$$

$$(k_i, k_j) = (k_n, k_i) XOR (k_n, k_j) \dots \quad (5)$$

Table 2: Odor Keys Map1

t	k₁k₂	k₁k₃	k₁k₄	k₁k₅	k₁k₆
Lower Bounded					
10	100	127	122	122	98
20	136	155	131	128	185
30	189	171	181	181	146
Upper Bounded					
40	183	162	177	191	159
50	142	162	180	185	153
60	144	191	169	170	138

Table 3: Odor Keys Map2

t	k₂k₃	k₂k₄	k₂k₅	k₂k₆
Lower Bounded				
10	27	30	30	6
20	19	11	8	49
30	22	8	8	47
Upper bounded				
40	21	6	8	40
50	44	58	55	23
60	47	57	58	26

Table 4: Odor Keys Map3

t	k₃k₄	k₃k₅	k₃k₆
Lower Bounded			
10	5	5	29
20	24	27	34
30	30	30	57
Upper Bounded			
40	19	29	61
50	22	27	59
60	22	21	53

Table 5: Odor Keys Map4

t	k_4k_5	k_4k_6
Lower Bounded		
10	0	24
20	3	58
30	0	39
Upper Bounded		
40	14	46
50	13	45
60	3	35

Table 6: Odor Keys Map5

t	k_5k_6
Lower Bounded	
10	24
20	57
30	39
Upper Bounded	
40	32
50	32
60	32

Careful analysis of the odorant feature maps in Tables 2-6, results in the following observations:

1. The lower bounding encloses the unstable part of the sensor's response to odor keys, while the upper bounding encloses the stable and certain part of the sensor's response.
2. As the number of equity features increases in the lower and unstable bounding, the probability of such a key to be derived from the master one decreases.
3. As the number of equity features increases in the upper and stable bounding, the probability of such a key to be derived from the master one increases.

From the features maps in the tables, semi-final feature map is constructed by the algorithm based on sequential correlation of occurring features per main key per same location over succession of keys. This is illustrated in Table 7.

Table 7: Lower Bounded Final Feature Map

Testing Key	Number of Identical Features {Lower, Upper}	Bounded Features {lower, Upper}
k1	{0, 0}	{15, 15}
k2	{2, 0}	{12, 12}
k3	{0, 2}	{9, 9}
k4	{0, 0}	{6, 6}
k5	{0, 3}	{3, 3}

From table 7, it is clear that k_5 is the correct key as it has zero equity features in the lower bounding and three out of three equity features in the upper bounding. This gives a matching of %100, while k_3 has two out of nine features with matching of only %22, with the rest of the keys k_1, k_2, k_4 having %0 matching.

Considering the keys data for k_5 and k_6 and the resulted pairing of (k_5, k_6) , which is shown in Figure 1, the following is deduced from the plot:

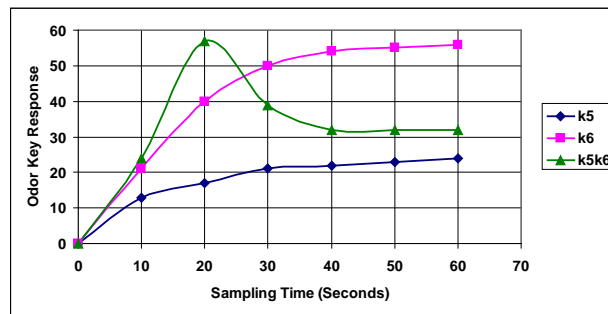


Figure 1: Master and Derived key Responses.

1. k_5k_6 response is consistent with the typical sensor response as it rises when the sensor is exposed to the odorant, reaching a maximum value, then decaying over time to a stable equity and constant region.
2. The observed response for k_5k_6 differs from the conventional response in that it settles at a constant value over the upper bounding part for the rest of the sampling time, instead of decaying towards zero.
3. The observed constant value, which is derived from both k_5 and k_6 responses proved that k_5 is the derived key and can be used to access the system.

For k_3 as a testing key and as it has two equity features in the upper bound, is not a derived key from k_6 , as it shows unstable curve with no constant region, as illustrated in Figure 2.

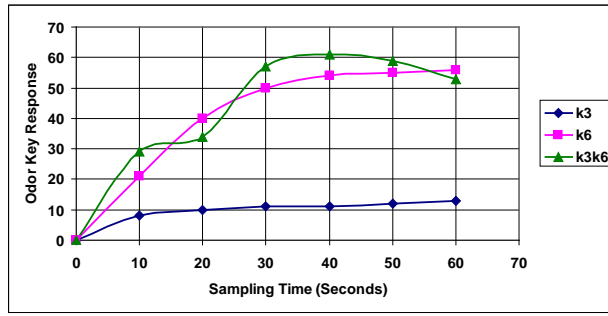


Figure 2: Relationship between k_3 and k_6 .

The stability and instability of odor keys and the checking of matching with the master key is further checked by the algorithm using slide-XOR mapping as shown in Table 8.

Table 8: Slide-XOR for k_5k_6

k_6/k_5	13	17	21	22	23	24
21	24	4	0	3	2	13
40	37	57	61	62	63	48
50	53	35	39	36	37	42
54	59	39	35	32	33	46
55	58	38	34	33	32	47
56	53	41	45	46	47	32

Table 8 is divided into two main areas:

1. Unstable, lower bounded characterized by the line matrix [24, 57, 39].
2. Stable, upper bounded area characterized by the line matrix [32, 32, 32].

From the Mapping of data in Table 8, the following is observed:

1. In the stable, upper bounded area, the result of XORing any diagonally based values around the center value of 32 is 0. This indicates validity of k_5 as derived from k_6 . The pairs are: {33,33}, {46,46}, {47,47}, {32,32}.
2. In the stable, upper bounded area, the result of XORing any diagonally unequal values around the center value of 32 is constant and equal to 14. The pairs are: {46,32}, {47,33}.

The table which represents a multi-level filtered map shows clearly which odor key fits to unlock and access the required system.

The overall decision making using the DOK classification algorithm can be described by equation 6.

$$Odor_{code\ match}(t, x+i) = XOR(k_m, k_{m+1}) = 0 \dots \tag{6}$$

The overall DOK algorithm is simulated using Weight Elimination Neural Algorithm (WENA) as shown in Figure 3.

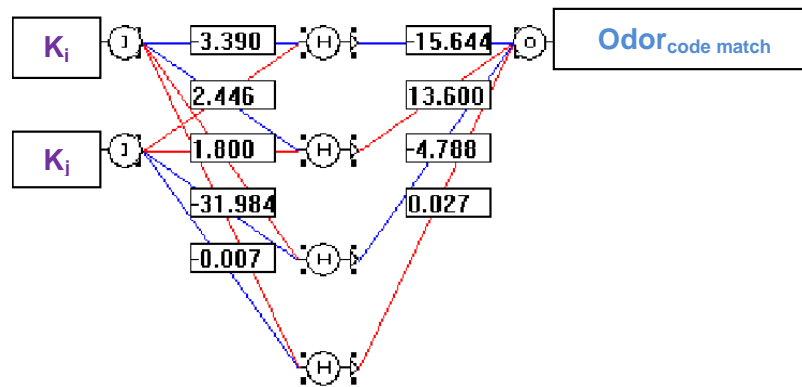


Figure 3: WENA Structure (Alpha: 0.9, LRate: 0.1, dL: 2.5)

Training of the Neural Network was carried out using Weight Elimination Neural Algorithm (WENA), which is a bidirectional Bottom-Up, Top-Down pruning algorithm. It starts with a simple, then complex network and drives unnecessary weights during training towards zero.

The WENA makes use of a liability function that is based on the error function. By reducing the number of connection weights and hence the model's complexity using the weight-elimination liability term, it is expected that network's classification performance to improve.

The weight-elimination overhead function is shown in equation 7. The liability term in weight-elimination minimizes the sum of performance error and the number of weights using standard back propagation technique.

$$E_{Total}(W) = E_{Sum\ Squared}(W) + E_{Liability}(W) \dots \quad (7)$$

$E_{Total}(W)$ is the combined overhead function that includes the initial overhead function, $E_{Sum\ Squared}(W)$ and the weight-elimination term $E_{Liability}(W)$.

$$E_{Sum\ Squared}(W) = \frac{1}{2} \sum_k (T_k - O_k)^2 \dots \quad (8)$$

Where:

T_k : Target Output

O_k : Actual Output

$$E_{Liability}(W) = \xi \left(\sum_{jk} \frac{\left(\frac{w_{jk}}{w_{epochs-n}} \right)^2}{1 + \left(\frac{w_{jk}}{w_{epochs-n}} \right)^2} \right) \dots \tag{9}$$

Hence;

$$\Delta W = \left(-\eta \frac{\partial E_{Sum Squared}}{\partial W} \right) - \left(\xi \frac{\partial E_{Liability}}{\partial W} \right) \dots \tag{10}$$

Where

η : Learning Rate (between 0 and 1)

W represents the weight vector, ξ is the weight-reduction factor, and w_{jk} represents the individual weight of the neural network model.

The role of the weight-reduction factor is to determine the relative importance of the weight-elimination term. Larger values of ξ pushes small weights to further reduce their size. Small values of ξ will not affect the network.

The scale parameter, $w_{epochs-n}$, is a scale parameter computed by the WENA, and chosen to be the smallest weigh from the last epoch or set of epochs to force small weights to zero.

The Neural engine is tested with another odor (k_7) derived from odor k_6 . The ratios of chemical concentration derivation are $k_7=0.67K_6$ and $k_5=0.33K_6$. The results are shown in Table 9:

Table 9: Neural Networks Testing Results

k7	k6	k5	k7k6-Odor code match	k5k6-Odor code match
25.000	21.000	13.000	3.000	24.000
40.000	40.0000	17.000	42.000	57.000
50.000	50.000	21.000	30.000	39.000
55.000	54.000	22.000	26.000	32.000
55.000	55.000	23.000	26.000	32.000
60.000	56.000	24.000	26.000	32.000

It is clear that both codes have similar upper and lower bound characteristics with similar patterns that indicate that they originated from the same odor source (master key), hence both keys can be used as passwords and encryption keys. It also indicates that the unlocking key and password can be changed by deriving another key from the original with the ability to use multi-level passwords and public and private keys, with the advantage of hiding the keys inside the master key.

4 CONCLUSION

The implemented intelligent algorithm within the designed sensing system proved to be able to detect and classify different odor combinations. Such an approach combined with neural engine forms an excellent platform for further development of odor keys as security and data encryption keys. Such keys can be an array of metal oxide sensors or any custom designed chemiresistors together with an electronic system that is controlled by specially developed software, which extract sequences and subsequence and place them in a feature map before applying the proposed algorithm. The system makes decisions about the odorant at certain concentrations using detection and recognition levels for the odorants. Such security system can replace traditional biometric systems like fingerprint or iris. It also replaces traditional door and safe keys with odor keys that are randomly selected and combined with impossibility of hacking.

REFERENCES

- [1]. E. Kim 1, S. Lee, J. Kim, C. Kim, Y. Tae Byun, H. Kim, T. Lee, Pattern Recognition for Selective Odor Detection with Gas Sensor Arrays. *Sensors*. 2012. 12(12): p.16262-16273. doi:10.3390/s121216262.
- [2]. Y. Tian, X. Kang, Y. Li, W. Li, A. Zhang, J. Yu, Y. Li, Identifying Rhodamine Dye Plume Sources in Near-Shore Oceanic Environments by Integration of Chemical and Visual Sensors, *Sensors*. 2013. 13(13): p.3776-3798. doi:10.3390/s130303776.
- [3]. T. Dymerski, J. Gębicki, P. Wiśniewska , M. Śliwińska, W. Wardencki, J. Namieśnik, Application of the Electronic Nose Technique to Differentiation between Model Mixtures with COPD Markers, *Sensors*. 2013. 13(4): p.5008-5027. doi:10.3390/s130405008.
- [4]. K. Fujioka, E. Arakawa, J. Kita, Y. Aoyama, Y. Manome, K. Ikeda, K. Yamamoto, Detection of *Aeromonas hydrophila* in Liquid Media by Volatile Production Similarity Patterns, Using a FF-2A Electronic Nose, *Sensors*. 2013. 13(1): p.736-745. doi:10.3390/s130100736.
- [5]. W. Yu, S. Wang, Key pre-distribution using combinatorial designs for wireless sensor networks, nodes have the same capabilities and constraints, *WSEAS Transactions on Mathematics*, 2013. 12(1): p.32-41. doi:10.1109/TNET.2007.892879.

- [6]. Y. Lan, X. Zheng, J. Westbrook, J. Lopez, R. Lacey, W. Hoffmann, Identification of Stink Bugs Using an Electronic Nose. *Journal of Bionic Engineering*, 2008. 5(1): p.172-180. doi:10.1016/S1672-6529(08)60090-6.
- [7]. M. Zarzo, Effect of Functional Group and Carbon Chain Length on the Odor Detection Threshold of Aliphatic Compounds, *Sensors*, 2012. 12(1): p.4105-4112. doi:10.3390/s120404105.
- [8]. Puligundla, J. Jung, S. Ko, Carbon dioxide sensors for intelligent food packaging applications, *Food Control*, 2012. 25(1): p.328-333. doi.org/10.1016/j.foodcont.2011.10.043.
- [9]. M. Mannoor, H. Tao, J. Clayton, A. Sengupta, D. Kaplan, R. Naik, N. Verma, F. Omenetto, M. McAlpine, Graphene-based wireless bacteria detection on tooth enamel. *Nature Communications*, 2012. 763(3): p.1-8. Doi:10.1038/ncomms1767.
- [10]. F. Benrekia, M. Attari, M. Bouhedda, Gas Sensors Characterization and Multi-layer Perceptron (MLP) Hardware Implementation for Gas Identification Using a Field Programmable Gate Array (FPGA), *Sensors*, 2013. 13(1): p.2967-2985, 2013 doi:10.3390/s130302967.
- [11]. B. Zhou, J. Wang, Detection of Insect Infestations in Paddy Field using an Electronic Nose, *International Journal Of Agriculture & Biology*, 2011. 13(5): p.708-712. doi:11-058/SAE/2011/13-5-707-712.
- [12]. C. Wongchoosuk, M. Lutz, T. Kerd-charoen, Detection and Classification of Human Body Odor Using an Electronic Nose, *Sensors*, 2009. 9(1): p. 7234-7249. doi:10.3390/s90907234.
- [13]. H. Lee, W. Yang, N. Choi, S. Moon, Encapsulation of Semiconductor Gas Sensors with Gas Barrier Films for USN Application, *ETRI Journal*, 2012. 34(5): p.713-718. doi:10.4218/etrij.12.0112.0266.
- [14]. A. Lotfi, S. Coradeschi, Odor Recognition for Intelligent Systems, *IEEE intelligent Systems*, 2008. 23(1): p.41-48. doi: 10.1109/MIS.2008.11.
- [15]. M. Ke, M. Lee, C. Lee, L. Fu, A MEMS-based Benzene Gas Sensor with a Self-heating WO₃ Sensing Layer, *Sensors*, 2009. 9(4): p.2895-2906. doi:10.3390/s90402895.
- [16]. M. Iskandarani, Low Pass Filter Model for Chemical Sensors in Response to Gases and Odors, *American Journal of Applied Sciences*, 2012. 9(4): p.605-608. doi: 10.3844/ajassp.2012.605.608.
- [17]. M. Iskandarani, Inheritance based Intelligent Technique Employing Nested-XOR with Recursion for Recognition and Classification of Odors using Multi-Sensor Nose System, *American Journal of Applied Sciences*, 2011. 8(9): p.910-917. 10.3844/ajassp.2011.910.917.
- [18]. M. Iskandarani, A Novel Odor Key Technique for Security Applications Using Electronic Nose System, *American Journal of Applied Sciences*, 2010, 7(8): p.1118-1122. doi:10.3844/ajassp.2010.1118.1122.
- [19]. M. Iskandarani, A Novel Approach to Signal Detection of Sensor Array Units Using 5-3-1 Rule Based Matched Filter Algorithm with Intelligent Identifiers, *American Journal of Engineering and Applied Sciences*, 2010. 3(2): p.427-432. doi: 10.3844/ajeassp.2010.427.432.
- [20]. M. Iskandarani, Mathematical Modeling and Characterization of Thin Film, Narrow Gap Sensor Array Units (SAU), *American Journal of Applied Sciences*, 7(9): p.1277-1284. doi: 10.3844/ajassp.2010.1277.1284.

Algorithm Development for Analysis of Statistical Accuracy of the Extraction of Cartographic Features in Digital Images

Guilherme Pina Cardim, Erivaldo Antônio da Silva, Maurício Araújo Dias

FCT/UNESP - Faculty of Science and Technology - University of São Paulo State, Brazil;

gpcardim@gmail.com, silva.erivaldo@gmail.com, madias@fct.unesp.br

ABSTRACT

Cartography uses large-scale digital images obtained by remote sensing. Such images are commonly used for the extraction and / or detection of cartographic features, which are the targets of interest in mapping. Extracting targets of interest from digital images streamlines the mapping, but the accuracy of this mapping depends on the characteristics of the features of interest present in the extracted image. Therefore, this paper proposes an automated way to calculate and display statistical values so that the extraction processes of any feature type mapping can be assessed considering its quality and quantity. With this purpose in mind, a computer program has been developed. This program applies an already established methodology to calculate statistical values concerning the results obtained by the automatic extraction process. The implemented program performs calculations in a quick and objective manner. In addition, it also generates resultant images that provide the user viewing of the errors obtained by the reported method. This paper presents the results obtained from the use of this computer program. Thus, the program developed accomplishes the proposed objectives, allowing the user to perform a consistent analysis of the automated extraction, since this evaluation is performed based on statistical calculations. Therefore, this program assists researchers and scholars of cartography to evaluate automatic extraction processes in the cartographic features of interest.

Keywords: Extraction of Cartographic Features, Evaluation Process, Digital Image Processing.

1 INTRODUCTION

Remote sensing images, from earth-orbiting satellites, have been widely used for several studies. These studies could be improved and automated through the use of digital image processing (DIP) [2], [17], which had its greatest impetus in the late 50's. Already in the 1960's, the U.S. launched many satellites into orbit, such as the GOES and the NIMBUS, in order to capture and send orbital images to Earth through techniques of PDI . Since then, several satellites were launched into orbit with this goal. From this point, cartographic studies that use

these images to design computational algorithms in order to extract cartographic features in the images [19] have started. We use the term targets for cartographic features or characteristics of interest present in the digital image related to the mapping area, such as roads, rivers, and even crater pictures of planetary surfaces. Among the purposes of an extraction, we can mention the use of extracted images for mapping large areas, the cartographic updating and calculation of flooded areas, for example.

Over time, several methods of feature extraction have been developed. All aim at a methodology capable of automatically extract features from digital images from any earth-orbiting satellites. Once the extraction result is obtained by the several developed methods, it is of a great importance being able to evaluate the quality obtained by this process.

In the literature, some metrics are presented to evaluate the quality achieved by an extraction method [20], however these metrics were used only for extraction of the road network. Furthermore, there are metrics which are adapted and implemented in algorithms [18], [4], but these works perform analysis without using the tolerance areas, while there is an algorithm that only uses them [3]. Another computer program found on the automation of the evaluation [14] is not in the public domain and therefore cannot be used on an ongoing basis. Besides this, the methodology and the metrics used by this program are still unclear. Thus, researchers find it difficult to qualify the developed processes of extraction. As a result, the quality of the extraction process is usually visually analyzed or by manually calculated metrics.

Therefore, this paper proposes an automated way to calculate statistical values for the extraction processes of cartographic features so that they can be assessed from qualitative and quantitative viewpoints, using or not the tolerance area. A variation of the methodology for calculating the metrics in the literature is also proposed [20].

It is justified by the necessity of using a free computer program to calculate specific statistical values related to quality analysis presented in a particular automatically performed extraction process, regardless of the type of feature mapping in this image, so that this program can be used by the user community area.

The remaining part of this paper is organized as follows. Section 2 provides the necessary definitions for the understanding of the methodology applied in this work. Section 3 presents the methodology used in the computer program to obtain statistical values. Section 4 shows the results obtained by the computer program at each step the methodology presented. The last section presents a discussion and the conclusions made in accordance with the results.

2 THEORETICAL RECITAL

In this section, we will provide a theoretical knowledge on the studied subject during the development of this project, such as concepts present in the literature about the evaluation process for the extraction of cartographic features and metrics related to this subject.

2.1 Assessment Methods of Cartographic Extraction

Literature is scarce on how to evaluate extraction methods for cartographic features. It is commonly observed in the literature to use two methods to evaluate the results obtained during the extraction process: the overlay method and the method described by Christian Wiedmann [20], [21]. The first method is simple and performed overlapping the extracted image on the original image, thus making it possible to observe whether any feature of interest was extracted by the executed process. This process is usually carried out during the steps determination and parameters extraction tests, thus facilitating the visualization of large displacements and errors made in the implementation of the studied extraction method.

However, the superposition method does not provide a good quality metric. Thus, the method reported in the literature for determining a good quality metric for a process of extracting features of interest is the method described by Christian Wiedmann in its various publications, presented in the next section, or adaptations of these metrics [3], [4], [18].

2.2 Quality Metrics

An evaluation of the results obtained is essential for any automatic system [21]. Thus, it is defined that for the evaluation of an automatic method for extraction of cartographic features is always necessary a reference image [3], [4], [18], [21], which is considered as correct. It is used as basis for the statistical calculations to be performed, whose statistical results serve as a basis for the user to determine the quality of the extraction obtained with through a certain automatic method used.

In order to evaluate the extraction process, the resulting image of the extraction process is compared pixel by pixel with the reference image. The comparison is carried out with an acceptance buffer (tolerance) disposed separately on both images [20]. The method described by the author considers as coincident pixels if one is present within the acceptance buffer of the other one during the comparison.

By doing so, the author is able to count the total number of the feature points of reference, which coincides with the feature extracted (pixels matching the extracted image - Figure 1 (a)), and the extracted feature points, which coincide with the reference feature (coincident pixels in the reference image - Figure 1 (b)). As a result, the method also obtains the total points that do not coincide during the comparisons.

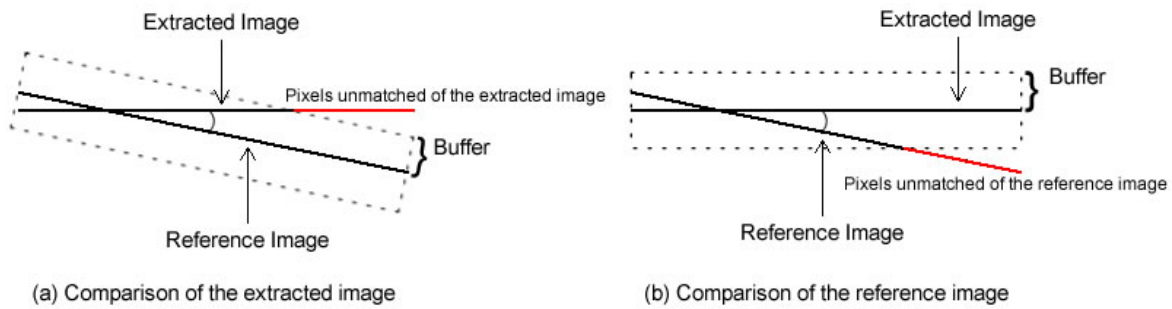


Figure 1: Features Matching Process

Some statistical calculations are defined based on the values of the totals mentioned in the previous paragraph [20], [21]. These calculations can be used by the user as metrics to evaluate the quality obtained by the extraction of cartographic features of interest.

Referring to Figure 1, it can be noted that the comparison method shown [20] uses only the skeleton or contour of the feature of interest present in a digital image. Therefore, preprocessing is necessary in order to perform skeletonization or detecting the edges of the feature of interest. Given that the errors obtained during an automatic extraction of features are usually located on the edges of the features of interest, the section 2.3. defines an approach to edge detection.

2.2.1 Completeness

The first proposed quality metric is called completeness [20], [21], and the calculation is defined by the equation 1. The completeness value represents the percentage of pixels of the reference image that has been properly extracted by the method used to obtain the extracted image. The value can vary in the interval [0:1] and the value 1 is considered optimum.

$$\text{completeness} = \frac{\text{matched pixels of reference image comparison}}{\text{total of pixels of the reference image}} \quad (1)$$

2.2.2 Correctness

The second quality metric is called correctness [20], [21], and its formula is given by the equation 2. This metric represents the percentage of the extracted image points that are in accordance to the reference image. The correctness can vary within the range [0:1], having the value 1 as great.

$$\text{correctness} = \frac{\text{matched pixels of extracted image comparison}}{\text{total of pixels of the extracted image}} \quad (2)$$

2.2.3 Quality

Once completeness and correctness metrics have been defined, a third metric called quality is presented. This metric does not include more information than what is already present in the completeness and correctness values, since the value of quality can be defined based on the

values obtained by the first two metrics presented, as shown in equation 3. However, the value of quality is useful in cases where it is necessary to use only one value to describe the quality obtained by a particular extraction method. As in the completeness and correctness metrics, the value of quality is in the range [0:1] and 1 is expected as a great result.

$$quality = \frac{completeness * correctness}{complet. - complet. * correct. + correct.} \quad (3)$$

2.2.4 Redundancy

Other metric reported in the literature is the value called redundancy [20]. Defined by the equation 4, this value represents the percentage of coincident pixels in the extraction that are redundant with each other, the ones that overlap. For this metric, the optimal value is 0, and the result may vary within the range $]-\infty: 1]$.

$$redundancy = \frac{matched\ of\ extraction - matched\ of\ reference}{total\ of\ extracted\ image} \quad (4)$$

2.2.5 RMS

In the literature, it is also displayed the simplified RMS metric (Root Mean Square) [20], which comprises the average difference between the overlapping pixels and the extraction reference. The result of this measure depends on the size of the buffer and usually has a normal distribution of the extracted feature on the buffer around the reference feature, allowing the use of the equation 5 to calculate the RMS. The RMS value is defined in the interval $[0:buffer\ size]$, with 0 as the optimal value for this quality metric.

$$RMS = \frac{1}{\sqrt{3}} * (buffer\ size) \quad (5)$$

2.2.6 Simplified comparison

Following the presented approach, a simplified comparison is accomplished without the use of buffer acceptance or tolerance feature and the total of interest without the need to find the edges of the feature, where errors tend to occur [4], [18]. This comparison is illustrated in Figure 2, originally presented in [4], in which the resulting image gets: black for non-feature points of interest; white color for pixels belonging to the feature of interest in both images; blue points that belong to the feature only in the resulting from the automated image extraction (false positives); and red for points that belong to the feature of interest only in the reference image (false negatives).

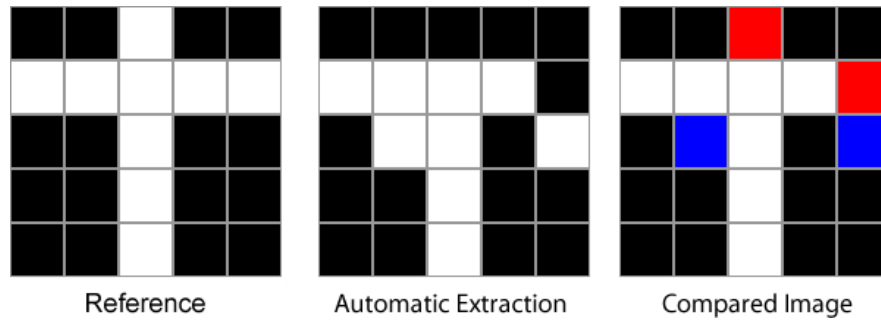


Figure 2: Simplified Comparison

From the resulting image, equation 6 is shown, which is called the correspondence equation (C). [4]

$$C = \left(\frac{TW}{TW + TR + TB} \right) \quad (6)$$

Where: C is the correspondence value; TW is the total of white pixels; TR is the total of red pixels; and TB is the total of blue pixels.

2.3 Edge Detection

Edge detection is one of the most common operations for image analysis. In 1996, it was supposed to have probably more algorithms defined in the literature than any other subject in particular [15]. Although not current, the previous statement shows the importance of this subject for literature. This is because the edges are the basic characteristics of the features present in an image [17]. The edges of objects or features present in an image carry essential information about the limits of the features of interest, being of extremely importance in the characterization and analysis of images. As a result, many algorithms have been developed in order to detect the edges present in a digital image.

It is known that the edges of a target in a digital image are perceived by the great change in the digital values within the image. When there is interest in finding large changes in a one-dimensional function, the best procedure is to use the theory of the second derivative, as this will be null when the magnitude value of a derivative is maximum [7]. However, this definition is not limited to a single dimension, and may be extended to two dimensional functions, such as an image. In digital images, the edge detection is defined as a local variation of the intensity of brightness.

Computationally, the gradient of an image can be calculated by performing a convolution on a particular mask on the original image. The Sobel operator is often used in this context. This fact is due to the good performance and low sensitivity to noise of the Sobel method. On the other hand, the Laplacian operator, being a second order derivative, is very sensitive to noise, for which it is rarely used in practice [16]. However, in our case, using the Laplacian operator becomes interesting, since this unwanted noise is a feature that needs to be detected by the operator. Thus, the edges detected by the use of Laplace becomes a variation of the original evaluation

method, which uses the skeleton of the feature of interest [20]. This variation has been proposed in this work because it is considered that, in general, the errors of an extracting method are located at the edges of the feature of interest.

2.4 Morphological Dilation

Another concept related to PDI, whose theoretical foundation is also important for this work, is the morphologic image dilation, which expands the objects present in the image in relation to the background of it [6]. Thus, the dilation is capable of eliminating small noises on an image object. This approach is embedded in the context of the mathematical morphology, which is based on the set theory to represent and manipulate the values of a digital image [16].

Thus, it is known that for two sets defined in R^2 , A and B , the dilation of A by B is denoted by $A \oplus B$ and defined by the equation 7 [9]. For this purpose, B is assumed as a structuring element and A as the set, or the image to be expanded.

$$A \oplus B = \left\{ Z \mid \left(\hat{B} \right)_z \cap A \neq \emptyset \right\} \quad (7)$$

The expansion can be viewed as a convolution of the structuring element B on the image A , for which the neighborhood of each feature point of interest will undergo some changes in accordance to the shape of the structuring element. Thus, the structural element has a primary role in the result generated by the expanding operator, once the size and shape of the structuring element respectively define the size and shape of the expanded area.

3 TEST AREA OF RESEARCH

In order to validate the methodology applied by the system, we have used a set of 15 images obtained from the database of the Faculty of Science and Technology - UNESP. In order to demonstrate this methodology, this work presents an image obtained by the panchromatic band of QuickBird satellite with a spatial resolution of 0.6m. This image is shown in Figure 3, which has as one feature of interest a clover from Raposo Tavares highway.



Figure 3: Original Image

Besides the original image, a reference image is required (ground truth) , which will be considered as correct, or as absolute truth for statistical calculations. The reference image can be generated from measurements taken in the field. However, the reference image is usually achieved manually by the use of an image editor software, selecting all points belonging to the cartographic feature of interest in the original image [4]. Therefore, as an example in this work, the reference image was manually obtained and is shown in Figure 4.

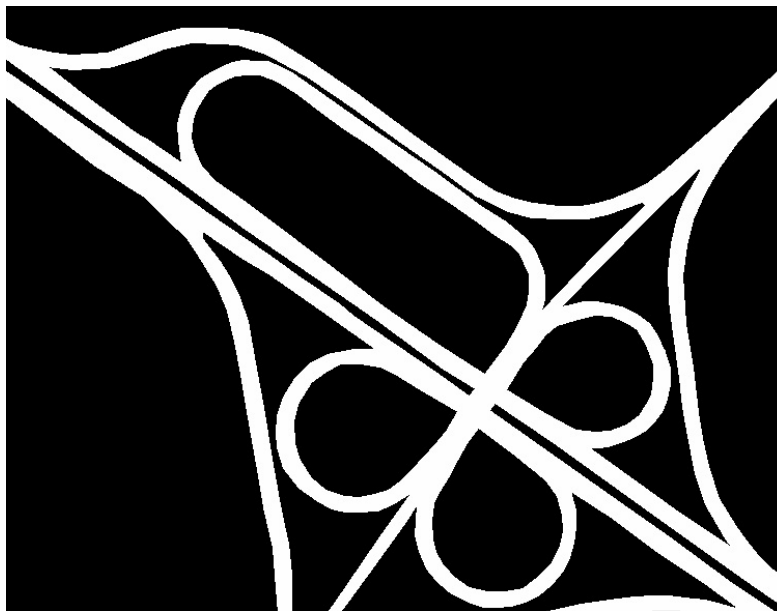


Figure 4: Reference Image

The computational proposed program also requires the resulting image from the process of automatic extraction so that it can be statistically analyzed. Thus, the image obtained by an automatic extraction method for the example is shown in Figure 5.

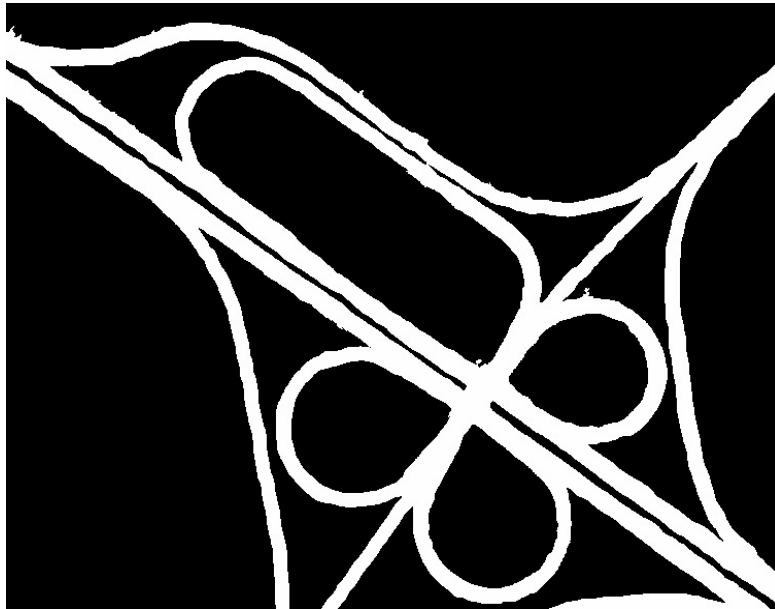


Figure 5: Automatic Extracted image

4 METHODOLOGY

The methodology applied in the computer program is developed based on results from the use of the metrics presented in the section 2.2. For this purpose, it is necessary to use a reference image, the resulting image from the automated extraction process, the original image used to obtain the reference and the extracted images.

Having the three images and knowing that the errors of an extraction process concentrate on the edges of the feature of interest, the first step of the evaluation methodology applied is to obtain the edges of the feature of interest present in the reference and extracted images. For this purpose, the Laplacian operator is applied over the image to detect any change in brightness values, since this filter behaves like a second order derivative being sensitive to any change in the values of the digital image. Thus, the Laplacian filter has shown as appropriate in order to detect the edges of the feature of interest, since the reference and extracted images are binary, which makes it easy to find modifications of brightness values of the digital image.

After obtaining the images containing the edges of the feature of interest, both in the reference as in the automatically extracted images, the second stage of the methodology is to check the coordinates or the position of each point belonging to the edges. These coordinates are used to fetch the gray levels in the original image, enabling the performance of traditional statistical calculations such as mean, mode, median, standard deviation and minimum and maximum values.

Having calculated the first statistical values, the third step of the evaluation method is to make a comparison between the obtained edges for the reference and the extracted images. The comparison is carried out pixel by pixel with no tolerance among the images, generating a resultant image, as exemplified by Figure 2. The resulting image of this comparison enables the visualization of coincident points and errors found during this process. Performed the comparison, the computer program gets the number of matching points and points that were classified as false positives (pixels blue) or false negatives (pixels red). Thus, it becomes possible to perform the calculations of the correspondence metric (Equation 6), of completeness (Equation 1) and the correctness (Equation 2), where the tolerance is regarded as zero for the calculation of the last two metrics.

However, as described in the literature [20], [21], the comparison can be performed using a tolerance, defined as a buffer acceptance for positioning the edge pixels of the feature of interest. Accordingly, the fourth step of the methodology consists of generating the tolerance range for the reference and extracted images by implementing morphological dilation operation on the images containing the edges of the feature of interest and reference images extracted. In order to perform the morphological operator, the user needs to define the structural element to be used and hence the shape and size of the tolerance generated by the program around the feature of interest.

The fifth step of the methodology applied by the program is to compare the image containing the edges of the feature of interest from the reference image with the image containing the dilated edges of the feature of interest of the extracted image. During the comparison, the program calculates the points that coincide or not, calling them reference coincident or not coincident points. Similarly, a comparison is also made of the image containing the extracted image edges of the feature of interest with the image containing the enlarged edges of the feature of interest from the reference image. In this comparison, the match points are called extraction coincidents and, consequently, the ones which do not match are called extraction non-coincident. In both comparisons, the program generates a resulting image containing errors or mismatched points found during each comparison.

Having calculated the reference and the extraction coincident or not coincident points, on the sixth stage of the methodology the program calculates the Equations 1, 2, 3, 4 and 5 in order to get the statistical values that influence the quality obtained by the automatic extraction of cartographic features. All calculated values enable the user to perform a statistical evaluation of the quality resulted by the automatic extraction performed to obtain the extracted image.

5 PRESENTATION AND ANALYSIS OF THE RESULTS

To demonstrate the methodology used by the program, this article presents one example, as mentioned above, for which the original, the reference and the extracted images are displayed respectively on Figures 3, 4 and 5.

As a first result of the methodology, we calculate the statistical values of mean, median, mode, standard deviation, minimum and maximum values of the brightness values of the original image according with the edges positions of the reference and extracted images. The values obtained for the sample are shown in Table 1.

Table 1: Traditional Statistics

	Reference	Extracted
Mean	54.437	53.427
Median	54	54
Mode	54	51
Minimum	18	28
Maximum	158	151
Standard Deviation	8.93232	9.06013

Continuing the methodology, the program performed the statistical calculations concerning the comparison without image tolerance containing the edges of the feature of interest of the reference and extracted images. Therefore, the obtained values for the example are presented in Table 2 and Figure 6 shows the result image.

Table 2: Comparison Without Buffer of Tolerance

	Comparison without tolerance
Total Matched	2349
Total of False Positives	6623
Total of False Negatives	6499
Completeness	0.265484
Correctness	0.261815
Correspondence	0.151832

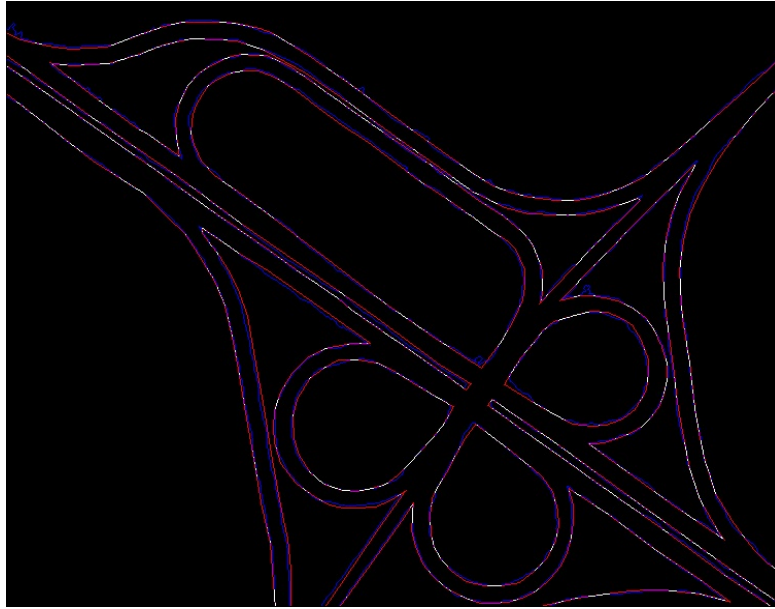


Figure 6: Result of Simplified Comparison

After, in order to generate the images of the edges with tolerances by morphological dilation, as described in the fourth step of the method, a structure element with dimensions 3x3 cross type was used, generating a point of tolerance at neighborhood 4.

As part of the fifth stage of the methodology, a comparison between the images with the edges of the reference image with the dilated image of the extracted image edges was performed. Figure 7 shows the image resulting from this comparison. In this image, the red points are those who have not corresponded in the comparison made between the images, being considered as false negatives.



Figure 7: Comparison of Reference Over Extracted Image

Finishing the fifth step, the reverse comparison was also performed. A comparison between the image of the automatically extracted image edges with the image of the performed dilation on the edges of the reference image was made. The red points, in this case, are considered false positives because they have not corresponded in this comparison. The image is shown in Figure 8.

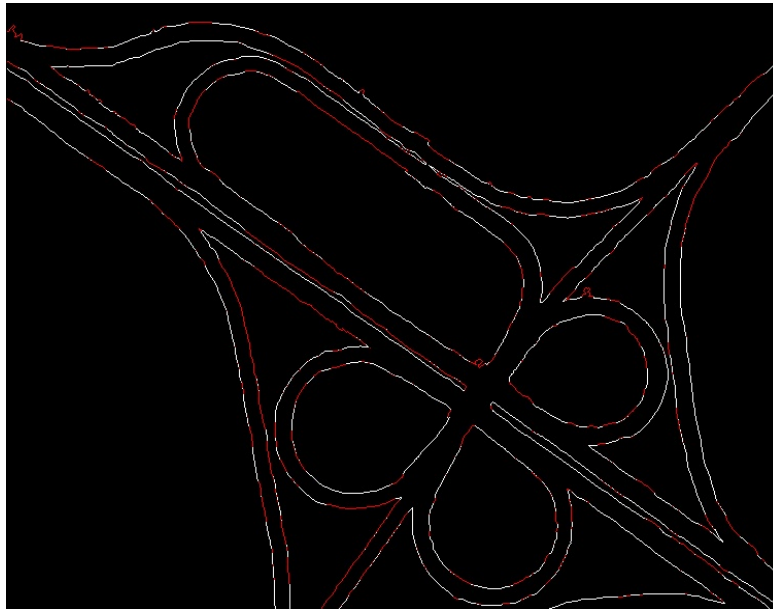


Figure 8: Comparison of Extracted Over Reference Image

Having performed these comparisons, the computer program calculated the related metrics compared with the tolerance area. The results calculated by the program are presented in Table 3. It is noteworthy that the structuring element used in the example was the type cross with dimensions 3x3.

Table 3: Comparison With Buffer of Tolerance

	Comparison with tolerance
Matched in the Extracted Image	5985
Unmatched in the Extracted Image	2987
Matched in the Reference Image	5982
Unmatched in the Reference Image	2866
Completeness	0.67608
Correctness	0.66707
Quality	0.50557
Redundancy	0.0005
RMS	1.1547

6 CONCLUSIONS

With the purpose of obtaining an automated way to calculate and display statistical values related to the results obtained by an automatic method of extracting cartographic features, a free computer program capable of performing the statistical calculations from the original image, from a reference image and from a resulting image from the extraction process to be evaluated has been developed.

Facing the need of automation of statistical calculations regarding the quality obtained by the extraction process, the software was able to remedy the limitations imposed by the researched studies [3], [4], [18], [20]. This is observed by the metrics automating related to comparisons with or without using tolerance through the implementation of a computer system. The importance of using the proposed qualitative and quantitative evaluations of automatic methods for extraction of cartographic features program was evidenced by the results obtained during the implementation of the program for the example shown. The program, for example, has noted that traditional statistics obtained for the reference images and extracted (Table 1) and the values of tolerance without comparison performed on these images (Table 2) did not allow a more accurate assessment of the quality achieved by the cartographic features automatic process extraction in the example shown. This is due to the high ratio between the obtained data for the reference and the extracted images in traditional statistical calculations, and the low values obtained for the comparison of images without tolerance. Thus, the statistical values related to the comparison performed by utilizing the tolerance range were to be analyzed.

Concerning the obtained values for the example, when using a tolerance of only one point, the statistical obtained values were not satisfactory for the automatic extraction of cartographic features, since quality metrics have shown that only 50% of the points agreed between the reference image and the image resulting from the automatic extraction process. However, we should remember that the tolerance used was just one pixel that is equivalent to 0.6m at the surface. Increasing the tolerance, the values should get better. This way, the values help the user in the evaluation, who becomes responsible for the final analysis of the evaluated extraction method.

In conclusion, the developed program has demonstrated its effectiveness by providing statistical data related to the quality of the obtained extract, facilitating the analysis of the user on the performed extraction method. The results obtained with the developed computer program confirm the importance of evaluating methods of automatic feature extraction.

The computational program contributes to the literature for the following reasons: it is able to calculate statistical values related to analysis of the quality of a procedure for automatic extraction, statistical calculations are carried out efficiently and quickly (the maximum waiting time for results was less than one (1) second, and the time depends on the size of the images and the comparison tolerances); it performs few comparisons during processing, since such

comparisons are performed on binary images; resulting images are generated in each matching process, which facilitates the visualization of the errors obtained in the positioning of these on the image; it allows a traditional statistical analysis on the original image; and moreover, the developed system is not restricted and may be operated by any user.

Therefore, it is concluded that the program developed assists the user to perform qualitative and quantitative assessments quickly and consistently in relation to the automatic extraction process executed, since these ratings are based on the studied statistical calculations and on the images resulting from the comparisons performed by the program.

All tests performed during this work were done on remote sensing images containing cartographic features of interest, because this is a common type of images used in Cartography. However, we intend to conduct further studies of the application of the same computer program for aerial photographs and even tests using others edge detectors.

REFERENCES

- [1]. Banon, G. J. F. Course at “X Congresso Nacional de Matemática Aplicada e Computacional”, Gramado, 1987.
- [2]. Baxes, G. A. “Digital Image Processing: principles and applications”, John Willey, New York, 1994.
- [3]. Cardim, G. P.; Silva, E. A. Development of na algorithm to analyze cartographic features extraction methods, in “35 International Symposium on Remote Sensing of Environment”, ISPRS, Maryland, 2013.
- [4]. Cardim, G. P.; Silva, E. A. Análise da qualidade de processos automáticos de extração de feições cartográficas, *Omnia Exatas*, 2011, 4(2): p. 7-18.
- [5]. Crósta, A. P. “Processamento Digital de Imagens de Sensoriamento Remoto”, IG/UNICAMP, Campinas, 1999.
- [6]. Davies, E. “Computer and Machine Vision: Theory, Algorithms, Practicalities”, Academic Press, 2012.
- [7]. Forsyth, D. A; Ponce, J. “Computer Vision – a modern approach”, Prentice Hall, 2003.
- [8]. Gomes, J.; Velho, L. “Computação Gráfica: imagem”, IMPA, Rio de Janeiro, 1994.
- [9]. Gonzalez, R. C.; Woods, R. E. “Processamento de Imagens – técnicas digitais”, Pearson Prentice Hall, New Jersey, 2008.
- [10]. Ishikawa, A. S. “Detecção de Rodovias em Imagens Digitais de Alta Resolução com o Uso da Teoria da Morfologia Matemática”, Master Project, FCT/UNESP, Presidente Prudente, SP, 2008.
- [11]. Lampinen, J.; Laaksonen, J.; Oja, E. “Remote Sensing and Image Interpretation”, John Wiley & Sons, 2008.

- [12]. Lampinen, J.; Laaksonen, J.; Oja, E. "Pattern Recognition", Image Processing and Pattern Recognition, Academic Press, 1998.
- [13]. Muller, D. N.; Daronco, E. L. "Operações Aritméticas em Imagens". Universidade Federal do Rio Grande do Sul, Porto Alegre, 2000.
- [14]. Nóbrega, R. A. A. "Detecção de Malha Viária na Periferia Urbana de São Paulo Utilizando Imagens Orbitais de Alta Resolução Espacial e Classificação Orientada a Objetos", PhD Thesis. Escola Politécnica, USP, São Paulo, 2007.
- [15]. Parker, J. R. "Algorithms for Image Processing and Computer Vision", John Wiley & Sons, 1996.
- [16]. Pedrini, H.; Schwartz, W. R. "Análise de Imagens Digitais: princípios, algoritmos e aplicações", Thomson Learning, São Paulo, 2008.
- [17]. Pitas, I. "Digital Image Processing Algorithms and Applications", John Wiley & Sons, 2000.
- [18]. Silva, E. A.; Cardim, G. P. Applying Digital Image Processing to Evaluate an Extraction Method of Cartographic Features in Digital Images, Journal of Earth Science and Engineering, 2012, 2(4): p. 241-246.
- [19]. Silva, E. A.; Leonardi, F. Calculation of the Area of Power Plant Using Mathematical Morphology, Journal of Communication and Computer, 2012, 9(2): p. 221-225.
- [20]. Wiedemann, C. External Evaluation of Road Networks, ISPRS Archives, 2003, XXXIV: p. 93-98.
- [21]. Wiedemann, C.; Heipke, C; Mayer, H.; Hinz, S. Automatic Extraction and Evaluation of Road Networks from Moms-2p Imagery, International Archives of Photogrammetry and Remote Sensing, 1998: p. 95-100.

Convolutional Bottleneck Network with Dropout for Dysarthric Speech Recognition

Toru Nakashika¹, Toshiya Yoshioka¹, Tetsuya Takiguchi¹, Yasuo Arikawa¹,
Stefan Duffner², Christophe Garcia²

¹*Department of System Informatics, Kobe University, JAPAN*

²*Université de Lyon, CNRS, INSA-Lyon, LIRIS, UMR 5205, FRANCE*

¹nakashika@me.cs.scitec.kobe-u.ac.jp

ABSTRACT

In this paper, we investigate the recognition of speech produced by a person with an articulation disorder resulting from athetoid cerebral palsy. The articulation of the first spoken words tends to become unstable due to strain on speech muscles, and that causes degradation of speech recognition. Therefore, we propose a robust feature extraction method using a convolutional bottleneck network (CBN) instead of the well-known MFCC. The CBN stacks multiple various types of layers, such as a convolution layer, a subsampling layer, and a bottleneck layer, forming a deep network. Applying the CBN to feature extraction for dysarthric speech, we expect that the CBN will reduce the influence of the unstable speaking style caused by the athetoid symptoms. Furthermore, we also adopt dropout in the output layer since automatically-assigned labels to the dysarthric speech are usually unreliable due to ambiguous phonemes uttered by the person with speech disorders. We confirmed its effectiveness through word-recognition experiments, where the CNN-based feature extraction method outperformed the conventional feature extraction method.

Keywords: Articulation disorders, Feature extraction, Convolutional neural network, Bottleneck feature, Dropout, Dysarthric speech.

1 INTRODUCTION

Recently, the importance of information technology in the welfare-related fields has increased. For example, sign language recognition using image recognition technology [1], text reading systems from natural scene images [2], and the design of wearable speech synthesizers for voice disorders [3, 4] have been studied.

As for speech recognition technology, the opportunities in various environments and situations have increased (e.g., operation of a car navigation system, lecture transcription during meetings, etc.). However, degradation can be observed in the case of children [5], persons with

a speech impediment, and so on, and there has been very little research on orally-challenged people, such as those with speech impediments. It is hoped that speech recognition systems will one day be able to recognize their voices.

One of the causes of speech impediments is cerebral palsy. Cerebral palsy results from damage to the central nervous system, and the damage causes movement disorders. Three general times are given for the onset of the disorder: before birth, at the time of delivery, and after birth. Cerebral palsy is classified as follows: 1) spastic type 2) athetoid type 3) ataxic type 4) atonic type 5) rigid type, and a mixture of types [6].

In this paper, we focused on a person with an articulation disorder resulting from the athetoid type of cerebral palsy as in [7]. Athetoid symptoms develop in about 10-15% of cerebral palsy sufferers. In the case of a person with this type of articulation disorder, the first movements are sometimes more unstable than usual. That means, the case of movements related to speaking, the first utterance is often unstable or unclear due to the athetoid symptoms. Therefore, we recorded speech data for a person with a speech impediment who uttered a given word several times, and we investigated the influence of the unstable speaking style caused by the athetoid symptoms.

In speech recognition technology, frame-wise features such as mel-frequency cepstral coefficients (MFCC), linear predictive coding (LPC), and an autoregressive model (AR) have been widely used so far. However, these features do not capture the temporal information unless delta features are used. Especially for dysarthric speech, where the signals fluctuate more obviously than the signals uttered by a physically unimpaired person, spectral transition in the short term is considered to be an important factor in capturing the local temporal-dimensional characteristics. In this paper, we employ a convolutional neural network (CNN) [8, 9])-based approach to extract disorder- dependent features from a segment MFCC map. The CNN is regarded as a successful tool and has been widely used in recent years for various tasks, such as image analysis [10, 11, 12], a spoken language [13], and music recognition [14]. A CNN consists of a pipeline of convolution and pooling operations followed by a multi-layer perceptron. In dysarthric speech, the key points in time-spectral local areas of an input feature map are often shifted slightly due to the fluctuation of the speech uttered by a person with an articulation disorder. However, thanks to the convolution and pooling operations, we can train the CNN robustly to deal with the small local fluctuations. Furthermore, we expect that the CNN extracts specific features associated with the articulation disorder we are targeting when we train the network using only the speech data of the articulation disorder.

For the research described in this paper, we used a convolutive bottleneck network (CBN) [15], which is an extension of a CNN, to extract disorder-specific features. A CBN stacks a bottleneck layer, where the number of units is extremely small compared with the adjacent layers, following the CNN layers. Due to the bottleneck layer having a small number of units, it is expected that it can aggregate the propagated information and extract fundamental features

included in an input map. Furthermore, we also use a dropout technique [16] to prevent overfitting appeared in the output layer. Since the label data (teaching signal) is obtained by forced-alignment from dysarthric speech where each phoneme fluctuates largely, the teaching signal for the training of the network is very unreliable. The dropout in the output layer ignores some information in the teaching signal, and thus will deal with the problem of the wrong alignment.

This paper is organized as follows: we briefly review the fundamental method, CNN in Section 2. The proposed feature extraction method and the structure of the CBN used in the experiments are presented in Section 3. In Section 4, we show the experimental results, and we give our conclusions regarding in Section 5.

2 CONVOLUTIONAL NEURAL NETWORK

In this section, we describe a convolution layer and a pooling layer, which are fundamental components of a CNN (convolutional neural network).

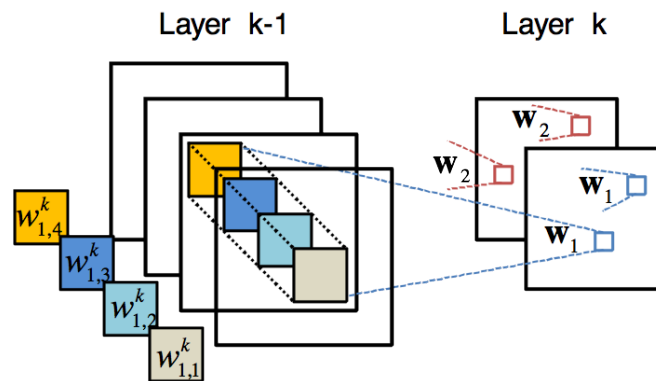


Figure 1: Feature maps in a convolutional layer (right) feed input feature maps (left)

2.1 Convolution layer

Assuming that we have a two-dimensional input feature map $\mathbf{x} \in \mathbb{R}^{N_n^x \times N_m^x}$ and a convolutive filter $\mathbf{w} \in \mathbb{R}^{N_n^w \times N_m^w}$, the output of a convolutive operation $\mathbf{h} = \mathbf{x} * \mathbf{w}$ also becomes a two-dimensional feature with the size of $N_n^h \times N_m^h$ ($N_n^h \equiv N_n^x - N_n^w + 1$ and vice versa). A CNN generally has a number of such filters $\{\mathbf{w}_1, \dots, \mathbf{w}_L\}$ in a convolutive layer, and feeds an input \mathbf{x} using each filter to create the corresponding outputs $\{\mathbf{h}_1, \dots, \mathbf{h}_L\}$, which is referred to as a feature map.

Given all of the feature maps in the $(k-1)$ th layer $\{\mathbf{h}_1^{k-1}, \dots, \mathbf{h}_i^{k-1}, \dots, \mathbf{h}_I^{k-1}\}$, the j th feature map $\mathbf{h}_j^k \in \mathbb{R}^{N_h \times N_h}$ in the k th (convolution) layer can be calculated as

$$\mathbf{h}_j^k = f \left(\sum_{i \in I} \mathbf{w}_{j,i}^k * \mathbf{h}_i^{k-1} + \mathbf{b}_j^k \right), \quad (1)$$

where $\mathbf{w}_{j,i}^k$ and \mathbf{b}_j^k indicate a predictable filter from the i th feature map in $(k-1)$ th layer to the j th map in the k th layer and a bias map of the j th map in the k th layer, respectively. In this paper, we used an element-wise sigmoid function for the activation function as follows

$$f(\mathbf{x}) = \frac{\mathbf{1}}{\mathbf{1} + e^{-\mathbf{x}}}, \quad (2)$$

where the fraction bar indicates element-wise division.

Each unit in a convolution layer is connected to the units in the corresponding local area of size $N_n^w \times N_m^w$ in the previous layer (local receptive field). In other words, the convolution layer in a CNN captures local patterns in an input map using various filters (Figure 1).

2.2 Pooling layer

Followed by the convolution layer, a pooling procedure is generally used in a CNN, creating what is called a pooling layer. Each unit in the pooling layer aggregates responses in the local subregion $\mathcal{P}(M \times M)$ in the previous convolution layer. As a result, a feature map in the pooling layer has the size of $N_n^h/M \times N_m^h/M$.

There exist various pooling methods (e.g. max-pooling), but we use average-pooling in this paper, calculated as follows

$$\mathbf{h}_j^{k+1} = f \left(w_j^{k+1} \cdot \frac{1}{M^2} \sum_{(u,v) \in \mathcal{P}} \mathbf{h}_{j,u,v}^k + b_j^{k+1} \right), \quad (3)$$

where w_j^{k+1} and b_j^{k+1} are weight parameter and a bias parameter of the j th feature map in the pooling layer $(k-1)$ th layer, respectively. $\mathbf{h}_{j,u,v}^k$ represents the unit in the corresponding subregion identified with (u, v) in the feature map in the k th layer.

This pooling process enables the network to ignore small position shifts of a key point in the input feature map since it aggregates information in the local area.

3 PROPOSED METHOD

In our approach, we use a convolutional neural network (CNN) that has a bottleneck layer in the network, referred to as a convolutive bottleneck network (CBN) [15], for capturing speaker-dependent features from a dysarthric speech signal.

3.1 Convolutive Bottleneck Network

A CBN consists of an input layer, convolution layer and pooling layer pairs, fully-connected MLPs (multi-layer perceptrons) with a bottleneck structure, and an output layer in the order shown in Figure 2. In our approach, the CBN feeds a mel map (two-dimensional acoustic features in time-mel-frequency) and outputs 54 phoneme labels. The MLP shown in Figure 2 stacks three layers (m_1 , m_2 , m_3), where we give 108 units, 30 bottleneck units, and 108 units in each layer, respectively. The filter sizes in the convolution layer and the pooling layer will be discussed in the experimental section. Since the bottleneck layer has reduced the number of units for the adjacent layers, we can expect that each unit in the bottleneck layer aggregates information and behaves as a compact feature descriptor that represents an input with a small number of bases, similar to other feature descriptors, such as MFCC, LDA (linear discriminant analysis) or PCA (principal component analysis). It is reported that a feature extraction method using bottleneck features improved speech recognition accuracy from a well-known ABN (American Broad News) corpus [17], and in this paper as well, we use such features (the unit values in the bottleneck layer) for speech recognition, instead of using MFCC. The extracted features are obtained from the statistically-trained speaker-dependent CBN; hence, it is expected that it better represents characteristics in the speech of the target articulation disordered speech than MFCC does.

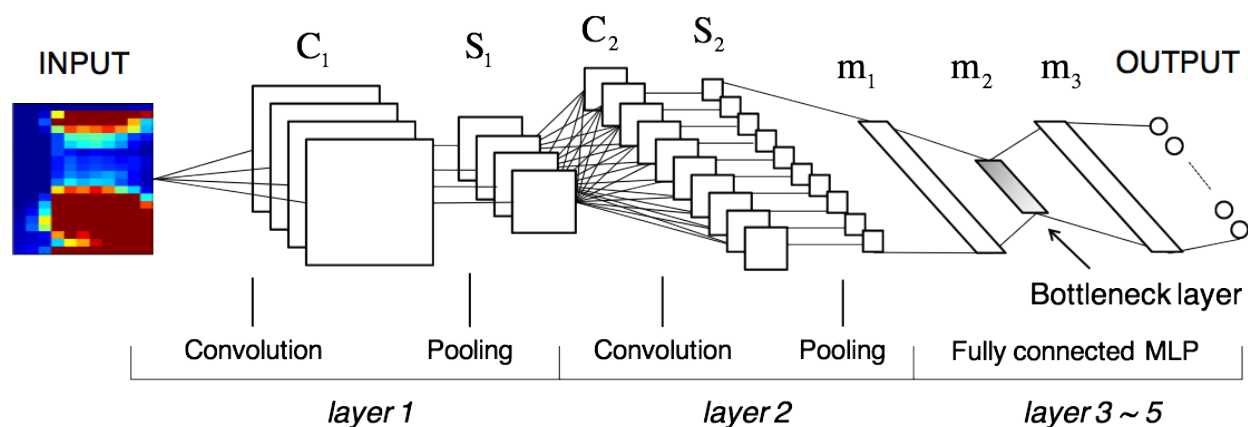


Figure 2: Convolutional Bottleneck Network (CBN)

3.2 Bottleneck feature extraction from dysarthric speech

Figure 3 shows a system flowchart of our method, where speaker-specific features are extracted using a CBN. First, we prepare the input features for training a CBN from a speech signal uttered by person with an articulation disorder. After calculating short-term mel spectra from the signal, we obtain mel maps by dividing the mel spectra into segments with several frames (13 frames in our experiments) allowing overlaps. For the output units of the CBN, we use phoneme labels that correspond to the input mel-map. For example, when we have a mel map with the label /i/, only the unit corresponding to the label /i/ is set to 1, and the others are set to 0 in the output layer. The label data is obtained by forced alignment using a hidden Markov model (HMM) from the speech data. The parameters of the CBN are trained by back-propagation with stochastic gradient descent, starting from random values. The bottleneck (BN) features in the trained CBN are then used in the training of another HMM for speech recognition.

In the test stage (“Feature extraction” in Figure 3), we extract features using the CBN, which feeds the mel maps obtained from test data and tries to produce the appropriate phoneme labels in the output layer. Again, note that we do not use the output (estimated) labels for the following procedure, but we use the BN features in the middle layer, where it is considered that information in the input data is aggregated. Finally, the system recognizes dysarthric speech by feeding the extracted BN features into HMMs.

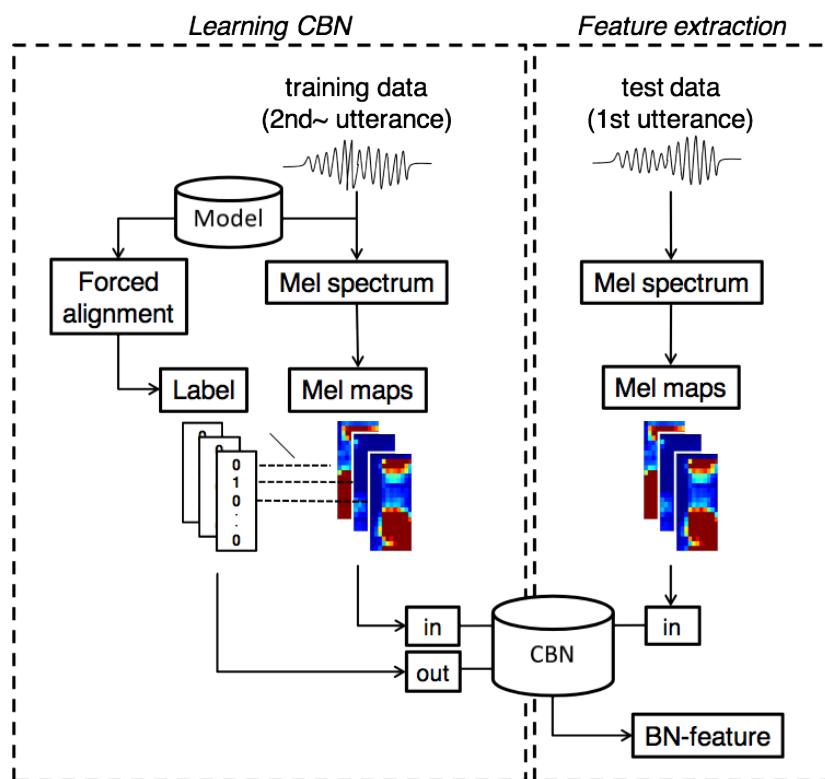


Figure 3: Flow of our feature extraction method for dysarthric speech using a convolutive bottleneck network

4 EXPERIMENTAL EVALUATION

4.1 Word recognition experiments (speaker A)

In this section, we discuss and evaluate our experiments of word recognition using a CBN presented in the previous section. Since we want to investigate the effectiveness of the CBN, we did not use dropout in the output layer of the CBN in these experiments.

4.1.1 Conditions

Our feature extraction method was evaluated on word recognition tasks for one male person (identified with “speaker A”) with an articulation disorder. We recorded 216 words included in the ATR Japanese speech database [18] repeating each word five times (Figure 4). The utterance signal was sampled at 16 kHz and windowed with a 25-msec Hamming window every 10 msec. Then we clipped each utterance manually. In our experiments, the first utterances of each word were used for evaluation, and the other utterances (the 2nd through 5th utterances) were used for the training of both a CBN and an acoustic model. We used the HMMs (54 context-independent phonemes) with 5 states and 8 mixtures of Gaussians for the acoustic model.

We trained and evaluated three CBNs: 28 units, 30 units, and 32 units in the bottleneck (BN) layer. The extracted BN features from each CBN were compared with 28-, 30-, and 32-dimensional MFCC+ΔMFCC, respectively.

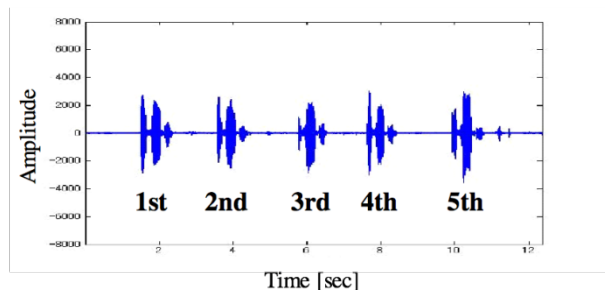


Figure 2: Example of recorded speech data

4.1.2 Training of CBN

In this section, we explain the training conditions of the CBN in detail. We trained the network using pairs of a mel map from the 2nd through 5th utterances and the label, as shown in Figure 3.

Each value of the convolutive filter $w_{j,i}^k$ (and the weight w_j^{k+1}) is initialized by [19] as follows:

$$w_{j,i}^k \ni w \sim \mathcal{U} \left(-\sqrt{\frac{6}{N_j + N_{j+1}}}, \sqrt{\frac{6}{N_j + N_{j+1}}} \right), \quad (3)$$

where $\mathcal{U}(a, b)$ denotes uniform distribution at the interval from a to b . N_j and N_{j+1} indicate the numbers of input dimensions and output dimensions at the j th layer, respectively. The bias parameters b_j^k and b_j^{k+1} were set to 0 as initial values.

These parameters were trained so as to minimize the errors between the target labels and the output values using a back-propagation algorithm. We iterated batch-based training with 50 frames in a mini-batch 100 times, with a fixed learning rate of 0.1.

4.1.3 CBN architectures

In this section, we discuss our preliminary experiment in which we change the architecture of a CBN (such as the number of feature maps and the size of a convolution filter) as shown in Table 1. In this preliminary experiment, we will see which architecture produced the best recognition accuracy. All the architectures have two pairs of a convolution layer and a pooling layer followed by three-layer MLPs with a bottleneck layer, forming a nine-layer network in total. We used 108, 30 and 108 units in the MLP part, in this order, for all the architectures (the bottleneck feature had 30 dimensions in this preliminary experiment). For the input layer, we used a 39-dimensional mel map with 13 frames without overlapping. The size of the map was 39×13. When we use ‘Arc1’ in Table 1, for example, the feature maps in each convolution and pooling layer have 36×12, 12×4, 9×3, and 3×1 sizes, in this order. In this case, 3×27(= 81) units are fully connected to the first layer of the MLP part.

Table 2 shows recognition accuracies obtained from each architecture. As shown in Table 2, we obtained the best word recognition accuracies from ‘Arc1’, although it did not always outperform the other architectures with respect to the MSE and label classification accuracy. This is considered to be due to the fact that the extracted bottleneck features of ‘Arc1’ were more abstract and suited to the acoustic model in word recognition. For the remaining experiments, we used ‘Arc1’ for the CBN architecture except for the number of units in the bottleneck layer.

Table 1: Filter size and number of feature maps for each architecture. The values for C1 (and C2) indicate filter size of the first (and the second) convolution layer that has #1 maps (and #2 maps), respectively. Each convolution layer is associated with the pooling layer (S1 and S2). The values for S1 and S2 mean the pooling factor M)

	C1	S1	#1	C2	S2	#2
Arc1	4×2	3	13	4×2	3	27
Arc2	10×4	2	13	10×4	2	27
Arc3	4×2	3	18	4×2	3	36
Arc4	4×2	4	13	4×2	2	27
Arc5	8×6	2	13	8×2	3	27

Table 2: Word recognition accuracies using the bottleneck features (Word-Acc.) obtained from each architecture, along with the mean squared error of the closed data (MSE), and the open classification accuracies of the phoneme labels using a CBN only (without using the acoustic models) (Phoneme-Acc.)

	Arc1	Arc2	Arc3	Arc4	Arc5
MSE ($\times 10^{-4}$)	2.42	2.01	2.32	2.43	2.09
Phoneme-Acc. (%)	48.7	49.3	47.9	49.4	49.5
Word-Acc. (%)	88.0	87.7	82.4	84.3	83.8

4.1.4 Results and discussion

Figure 5 shows the word recognition accuracies comparing our CBN features with the conventional MFCC features, when changing the number of feature dimensions. As shown in Figure 5, the use of bottleneck features in a convolutional network improved the accuracies from 84.3% to 88.0% (30 dimensions). This is due to the robustness of the CBN features to small local fluctuations in a time-melfrequency map, caused by the dysarthric speech.

We further investigated our method to check the effectiveness of the convolution layer (and pooling layer). In this evaluation, we replaced some convolution layers (here we refer to the pair of a convolution layer and a pooling layer as simply a “convolution layer”) with fully-connected layers in the network (‘Arc1’). First, we replaced the second convolution layer (‘Layer 2’ in Figure 2) with a fully-connected layer with 108 units. Second, we alternated two convolution layers with two fully-connected layers with 108 units, which is regarded as a 7-layer DBN (deep bottleneck network). The results are summarized in Table 3. From Table 3, we notice that the more convolution layers the network had, the better the performance of the system. Again, we consider that this is because the convolution filter captured characteristics in the input maps, making it robust to local fluctuations. When we compare the fully-connected model (DBN) with the MFCC, we see that the DBN performs poorly since it tends to suffer from over-fitting and a lack of robustness to the open data, especially in dysarthric speech, which fluctuates every time the speaker begins speaking.

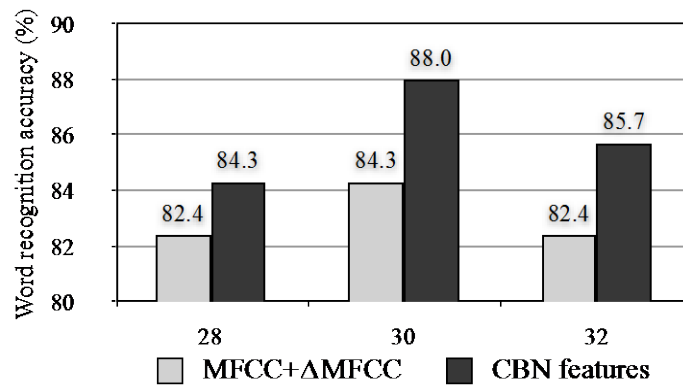


Figure 5: Word recognition accuracies (%) for the utterances of “speaker A” using bottleneck features in a convolutional network

Table 3: Word recognition accuracies as the number of convolution layers changed.

# of conv v.s. full layers	Acc. (%)
No conv, 5 full (DBN)	83.3
1 conv, 4 full (CBN)	84.7
2 conv, 3 full (CBN)	88.0
Baseline (MFCCs)	84.3

4.2 Word recognition experiments (speaker B)

We confirmed improvement of recognition accuracies by using a CBN feature extraction method in the previous experiments. However, the symptom of the articulation disorder and the tendency of the fluctuation in dysarthric speech vary on the speaker. In this section, we show experimental results using speech uttered by another person (female; “speaker B”) with an articulation disorder.

4.2.1 Conditions

We conducted word recognition experiments similarly to the previous experiments using speech of words included in the ATR Japanese speech database, uttered by “speaker B”. The speech data consists of 200 words, each of which was repeated three times (600 word speech in total). In the experiments, the first utterances of each word (200 words) were used for the test, and the other utterances (400 words) were used for the training of a CBN and acoustic models. The other configurations were set same as the experiments with “speaker A”.

4.2.2 Results and discussion

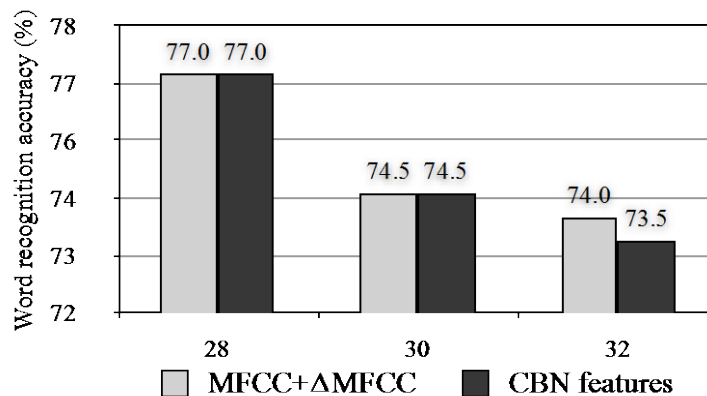


Figure 6: Word recognition accuracies (%) for the utterances of “speaker B” using bottleneck features in a convolutional network

Figure 6 shows experimental results of “speaker B”. As shown in Figure 6, unlike the results with “speaker A”, we did not see improvements of recognition accuracy with CBN features. One of the reasons is considered to be due to the assigned phoneme labels included in the training data. In other words, there exist gaps between the estimated labels obtained by forced alignment and actual labels, because the speaker could not utter some words correctly. It means that we give incorrect teaching signals to the network, which degrades the performance in the training. According to the experimental results, this problem arises especially on the second speaker. Figures 7 and 8 show examples of alignment for “speaker A” and “speaker B”, respectively. Each figure compares the results of forced-alignment obtained by using HMMs (a) and manually-assigned actual labels (b). As shown in Figure 7, the forced-alignment result of “speaker A” was similar to the actual labels. However, in case of “speaker B”, the segment for phoneme /y/ was enlarged and the following phoneme bounds were quite wrong as shown in Figure 8. This means that the features that should correspond to the phoneme /a/ or /m/ were regarded as the phoneme /y/ in the training.

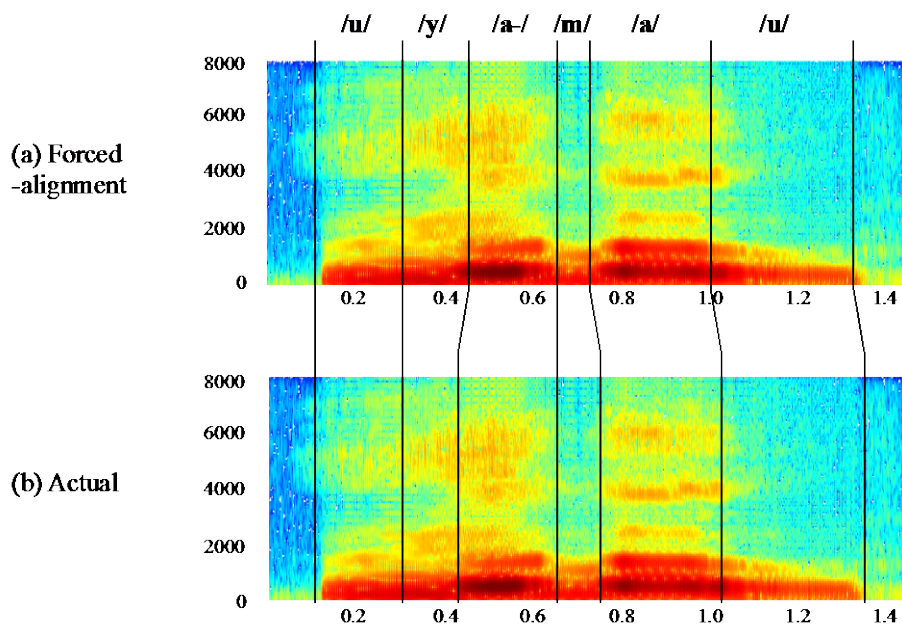


Figure 7: Example of forced-alignment for “speaker A”

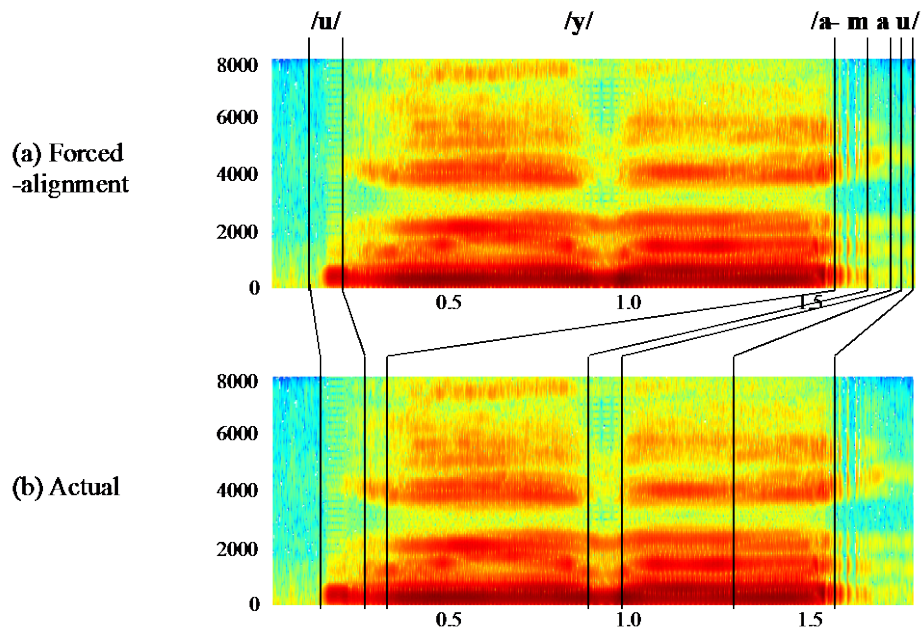


Figure 8: Example of forced-alignment for “speaker A”

4.2.3 Dropout effect

To solve the problem discussed in the previous subsection, we employ a dropout technique [16] when training the CBN, in this paper. The dropout gives the network generalization capabilities by ignoring some randomly-selected units (setting the weights to zero) in a layer. We expect

that the network with dropout in the output layer (training signal) prevents over-fitting to the label data that is unreliable because of forced-alignment. Specifically, given an input vector \mathbf{x}_p , the output of a network $\mathbf{f}_{out}(\mathbf{x}_p)$ is obtained by applying a binary mask as follows:

$$\mathbf{f}'_{out}(\mathbf{x}_p) = \mathbf{f}_{out}(\mathbf{x}_p) \circ \mathbf{m} \quad (4)$$

where \circ denotes element-wise product, and each value of \mathbf{m} is randomly set to 1 with a probability p_d (0 with a probability $1 - p_d$). When each unit in the output layer randomly takes the value of 0 even when the value is activated, the network tries to capture abstracts hidden in the data. In our experiments, we used $p_d = 0.5$.

Figure 9 shows experimental results, adding the result of a CBN with dropout from Figure 6. As shown in Figure 9, the accuracy was highly improved when we apply dropout. Compared with the baseline (MFCC+ Δ MFCC), the dropout method (CBN+DR) achieved an up-to-5-point improvement. Through these experiments, “ambiguous” training using dropout worked well especially for the speech where phonemes fluctuate largely and it is difficult to prepare the exact labels, as the speech uttered by “speaker B”.

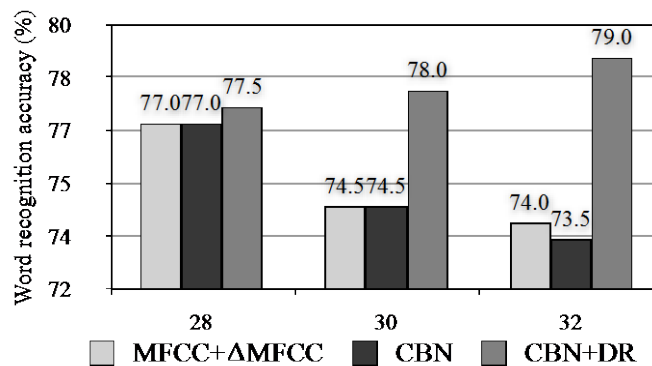


Figure 9: Word recognition accuracies (%) for the utterances of “speaker B” using bottleneck features and dropout (DR)

5 CONCLUSIONS

The articulation of speech uttered by persons with speech disorders tends to become unstable due to strain on their speech-related muscles. This paper described a robust feature extraction method using a convolutional bottleneck network (CBN). In word recognition experiments, our method achieved an approximately 4-point improvement compared with the conventional MFCC features for a male speaker (“speaker A”). For the another speaker (“speaker B”), we could not obtain better performance from the same technique as “speaker A”, because the speech fluctuates largely and it was difficult to estimate boundaries of phonemes correctly by

forced-alignment. However, when we realize ambiguous training using dropout, our method achieved a 5-point improvement compared with MFCC features for “speaker B”.

Since the tendency of the fluctuation in dysarthric speech depends on the speaker, we would like to apply and investigate our method to more persons with speech disorders in the future.

REFERENCES

- [1]. S. Cox and S. Dasmahapatra, “High-Level Approaches to Confidence Estimation in Speech Recognition,” *IEEE Trans. on SAP*, vol. 10, No. 7, pp. 460-471, 2002.
- [2]. M. K. Bashar, T. Matsumoto, Y. Takeuchi, H. Kudo and N. Ohnishi, “Unsupervised Texture Segmentation via Wavelet-based Locally Orderless Images (WLOIs) and SOM,” 6th IASTED International Conference COMPUTER GRAPHICS AND IMAGING, 2003.
- [3]. T. Ohsuga and Y. Horiuchi and A. Ichikawa, “Estimating Syntactic Structure from Prosody in Japanese Speech,” *IEICE Trans. on Information and Systems*, 86(3), pp. 558—564, 2003.
- [4]. K. Nakamura and T. Toda and H. Saruwatari and K. Shikano, “Speaking Aid System for Total Laryngectomees Using Voice Conversion of Body Transmitted Artificial Speech,” *Interspeech 2006*, pp. 1395—1398, 2006.
- [5]. D. Giuliani and M. Gerosa, “Investigating recognition of children’s speech,” *ICASSP2003*, pp. 137—140, 2003.
- [6]. S. T. Canale and W. C. Campbell, “Campbell’s Operative Orthopaedics,” Mosby-Year Book, 2002.
- [7]. H. Matsumasa, T. Takiguchi, Y. Arika, I. Li, T. Nakabayashi, “Integration of Metamodel and Acoustic Model for Speech Recognition,” *Interspeech 2008*, pp.2234-2237, 2008.
- [8]. Y. Lecun et al., “Gradient-based learning applied to document recognition,” *Proc. IEEE*, pp. 2278-2324, 1998.
- [9]. H. Lee et al., “Unsupervised feature learning for audio classification using convolutional deep belief networks,” in *Advances in Neural Information Processing Systems 22*, pp. 1096-1104, 2004.
- [10]. C. Garcia and M. Delakis, “Convolutional Face Finder: A Neural Architecture for Fast and Robust Face Detection,” *Pattern Analysis and Machine Intelligence*, 2004.
- [11]. M. Delakis and C. Garcia, “Text detection with Convolutional Neural Networks,” *Proc. of the Int. Conf. on Computer Vision Theory and Applications*, 2008.
- [12]. R. Hadsell et al., “Learning long-range vision for autonomous off-road driving,” *Journal of Field Robotics*, 2009.
- [13]. G. Montavon, “Deep learning for spoken language identification,” *NIPS Workshop on Deep Learning for Speech Recognition and Related Applications*, 2009.

- [14]. T. Nakashika, C. Garcia, and T. Takiguchi, "Local-feature-map Integration Using Convolutional Neural Networks for Music Genre Classification," Interspeech 2012, 2012.
- [15]. K. Vesely et al. "Convolutional bottleneck network features for LVCSR," in ASRU, pp. 42-47, 2011.
- [16]. C. Plahl, R. Schlyter, and H. Ney, "Improving neural networks by preventing co-adaptation of feature detectors," CoPR, 2012.
- [17]. C. Plahl et al., "Hierarchical bottle neck features for LVCSR," Interspeech 2010, pp. 1197-1200, 2010.
- [18]. A. Kurematsu et al., "ATR japanese speech database as a tool of speech recognition and synthesis," Speech Communication, No.4, pp.357-363, 1990.
- [19]. X. Glorot and Y. Bengio, "Understanding the difficulty of training deep feedforward neural networks," International Conference on Artificial Intelligence and Statistics, pp. 249-256, 2010.

Experimental Verification of Parameter Identification Method based on Symbolic Time Series Analysis and Adaptive Immune Clonal Selection Algorithm

Rongshuai Li

Engineering General Institute of Shanghai Construction Group, NO.666 Eeat Daming Road,
Shanghai,200080, China

Email: lrs0809@gmail.com

ABSTRACT

The parameter identification method based on symbolic time series analysis (STSA) and adaptive immune clonal selection algorithm (AICSA) was experimentally verified using a 5-story experimental model structure. In the experimental verification, both single and multiple damage scenarios were studied. A 5-story structure was initially healthy with all original columns intact. The single-damage case, the double-damage or the triple-damage case was simulated by replacing the columns of one, two or three different floors, respectively. The experimental results have shown that the parameter identification method based on STSA and AICSA can successfully identify structure parameters only utilizing measured acceleration information for various damage scenarios under different excitation conditions. The proposed approach was shown promising for application of SHM on buildings.

Keywords: structural health monitoring; clonal selection algorithm; symbolic time series analysis; adaptive immune; building structures;

1 INTRODUCTION

A new parameter identification method based on symbolic time series analysis (STSA) and adaptive immune clonal selection algorithm (AICSA) was proposed in reference [1]~[4]. To better assess the performance of the proposed methodology, experimental validation of the proposed approach has been conducted. Following the detailed description of the experimental setups, experimental results are provided which show the proposed approach to be very promising. A 5-story structure was initially healthy with all original columns intact. Two columns of one floor were then replaced by weak columns (of the same material and integrity as healthy columns, but with smaller cross-sectional area) to simulate a single-damage case. The double-damage or triple-damage case was simulated by replacing the columns of two or three different stories, respectively. Under the basement of the structure, there were some bearings so that

the structure could have a ground motion. The experimental results have shown that the proposed approach can successfully identify parameters of structure utilizing measured acceleration information for various damage scenarios under different excitation conditions. The proposed approach was shown promising for application of SHM on buildings.

2 PROPOSED METHOD

2.1 Procedure

In the research field of structural parameter identification, the time response of the system is usually compared with that of a parameterized model using a norm or some performance criterion to give us a measure of how well the model explains the system.

We will explain our methodology using a physical system with input u and output y . Let $y(t_i)$ ($i = 1, \dots, T$) denote the value of the actual system at the i th discrete time step. Suppose that a parameterized model able to capture the behavior of the physical system is developed and this model depends on a set of n parameters, i.e., $x = (x_1, x_2, \dots, x_n)^T \in R^n$. Given a candidate parameter value x and a guess \hat{X}_0 of the initial state, $\hat{y}(t_i)$ ($i = 1, \dots, T$), the value of the parameterized model, i.e., the identified system at the i th discrete time step, can be obtained. Hence, the problem of system identification boils down to finding a set of parameters that minimize the prediction error between the system output $y(t_i)$, which is the measured data, and the model output $\hat{y}(x, t_i)$, which is calculated at each time instant t_i .

Usually, our interest lies in minimizing the predefined error norm of the time series outputs, e.g., the following mean square error (MSE) function,

$$f(x) = \frac{1}{T} \sum_{i=1}^T \|y(t_i) - \hat{y}(x, t_i)\|^2 \quad (1)$$

where $\|\cdot\|$ represents the Euclidean norm of vectors. Formally, the optimization problem requires one to find a set of n parameters $x^* \in R^n$ so that a certain quality criterion is satisfied, namely, that the error norm $f(\bullet)$ is minimized. The function $f(\bullet)$ is called a fitness function or objective function. Typically, an objective function that reflects the goodness of the solution is chosen.

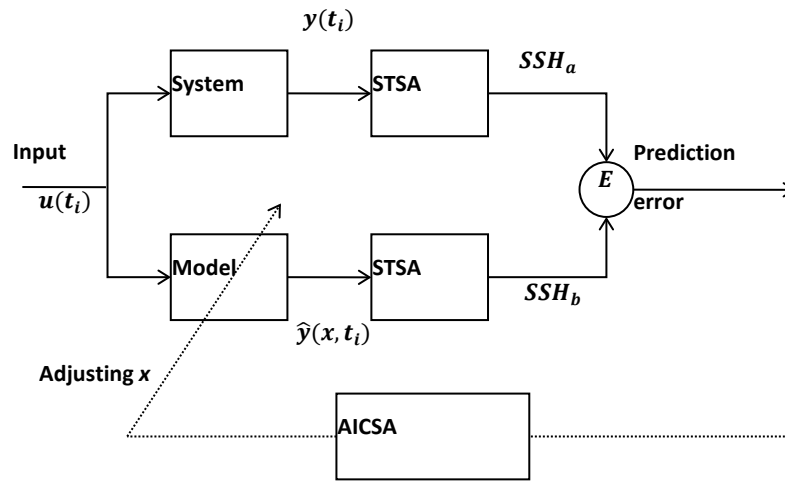


Figure 1. Procedure of AICSA combining STSA for identification of structural parameters.

In our methodology, we introduce an index, the relative state sequence histogram error (RSSHe), to measure the distance between SSH_a and SSH_b (SSH_a and SSH_b are the system output and model output, respectively). The definition is:

$$\begin{cases} SSH_a = [d_a^0, d_a^1, \dots, d_a^{Q-1}] \\ SSH_b = [d_b^0, d_b^1, \dots, d_b^{Q-1}] \end{cases}, \quad Q = 2^r \quad \text{and} \quad RSSHe = \sqrt{\frac{\sum_{i=0}^{Q-1} (d_b^i - d_a^i)^2}{\sum_{i=0}^{Q-1} (d_a^i)^2}} \quad (2)$$

where $d_{a/b}^i$ is the frequency of state i in SSH_a or SSH_b . The procedure of AICSA combining STSA for identification of structural parameters was shown in Figure 1.

2.2 Guideline for parameter selection

In STSA, the main parameters are the word length and window length, and they control the resolution of the whole representation space. For a window length T and word length r , two limiting cases of SSH are predefined as:

- Case 1: All states in the SSH are distributed uniformly, and the frequency of each state is $\frac{1}{2^r}$.
- Case 2: Only one state in the SSH has the frequency of 1; the frequencies of the other states are 0.

Suppose there are two different SSH s: SSH_a and SSH_b . From Equation (3), when SSH_a corresponds to limiting case 1 and SSH_b to limiting case 2, the maximum value of $RSSHe$ is:

$$RSSHe_{max} = \sqrt{\frac{\sum_{i=0}^{Q-1} (d_b^i - d_a^i)^2}{\sum_{i=0}^{Q-1} (d_a^i)^2}} = \sqrt{\frac{(1 - \frac{1}{2^r})^2 + (\frac{1}{2^r})^2 (2^r - 1)}{(\frac{1}{2^r})^2 * 2^r}} = \sqrt{2^r - 1} \quad (3)$$

When SSH_a and SSH_b are the same, the minimum $RSSHe$ is 0. Then,

$$RSSHe \in [RSSHe_{min}, RSSHe_{max}] = [0, \sqrt{2^r - 1}] \quad (4)$$

Since the minimum changeable unit in SSH is $\frac{1}{T-r+1}$, the change in frequency of one state in SSH will absolutely be related to the change in frequencies of other states. Supposing that there are only two minimum unit differences between SSH_a and SSH_b , the minimum distinguishable $RSSHe$ is:

$$RSSHe_{dis} = \sqrt{\frac{\sum_{i=0}^{i=Q-1} (d_b^i - d_a^i)^2}{\sum_{i=0}^{i=Q-1} (d_a^i)^2}} = \sqrt{\frac{(\frac{1}{T-r+1})^2 + (\frac{1}{T-r+1})^2}{\sum_{i=0}^{i=Q-1} (d_a^i)^2}} = \frac{\sqrt{\frac{2}{\sum_{i=0}^{i=Q-1} (d_a^i)^2}}}{T-r+1} \quad (5)$$

When SSH_a is limiting case 1, the maximum distinguishable $RSSHe_{dis}^{max}$ will be:

$$RSSHe_{dis}^{max} = \frac{\sqrt{2(r+1)}}{T-r+1} \quad (6)$$

When SSH_a is limiting case 2, the minimum distinguishable $RSSHe_{dis}^{min}$ will be:

$$RSSHe_{dis}^{min} = \frac{\sqrt{2}}{T-r+1} \quad (7)$$

The resolution is:

$$[RSSHe_{dis}^{min}, RSSHe_{dis}^{max}] = \left[\frac{\sqrt{2}}{T-r+1}, \frac{\sqrt{2(r+1)}}{T-r+1} \right] \quad (8)$$

Note that we also need to consider the number of the possible distributions of states in one SSH . If the number of states in SSH is 2^r and the minimum changeable unit is $\frac{1}{T-r+1}$, finding the total number of possible distributions N_{SSH} of SSH boils down to a classic combination problem, which is 'put $T - r + 1$ identical balls in 2^r different boxes. The combinatorial number is:

$$N_{SSH} = C_{T-r+2^r}^{2^r-1} \quad (9)$$

As we can see, longer window and word lengths are related to higher resolution, which means that the self and non-self-spaces can be separated much more accurately. This is the key to obtaining accurate structural parameter identification.

So far, our discussion of the effect of the window length and word length has been based on a case in which only one story's output (raw acceleration data) is used, but structures with multiple degrees of freedom (MDOF) may have more outputs than that. Supposing the outputs from N stories can be obtained, the boundary of the solution space is:

$$RSSHe \in [RSSHe_{min}, RSSHe_{max}]^N = [0, \sqrt{2^r - 1}]^N \quad (10)$$

The resolution falls to:

$$[RSSHe_{dis}^{min}, RSSHe_{dis}^{max}]^N = \left[\frac{\sqrt{2}}{T-r+1}, \frac{\sqrt{2(r+1)}}{T-r+1} \right]^N \quad (11)$$

Also, the total number of possible distributions increases to:

$$[N_{SSH}]^N = [C_{T-r+2r}^{2r-1}]^N \quad (12)$$

From Equations (10) to (12), it is evident that as more story outputs are obtained, the more accurate the identification results will be.

The root-mean-square error (RMSe) was used to verify the feasibility and performance of the identification results. RMSe is defined as

$$RMSe = \sqrt{\frac{\sum_{i=1}^n (k_{c,i} - k_{real,i})^2}{\sum_{i=1}^n k_{real,i}^2}} \quad (13)$$

where $k_{c,i}$ and $k_{real,i}$ are the candidate stiffness and real stiffness of the i th story, respectively.

3 EXPERIMENTAL SETUP

A series of experiments were performed to verify the performance of our proposed approach. The model structure is depicted in Figure 2.

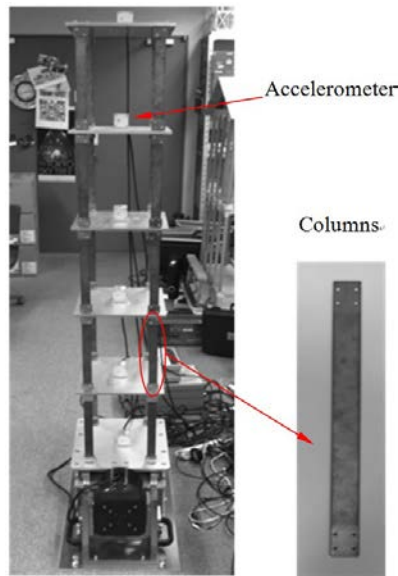


Figure 2. Experimental setup of small model

This experimental setup imitates a 5-story shear frame buildings. The story mass is decided by the aluminum floor slab which is 2.43 kg for each floor. The story stiffness is decided by the bronze plate spring with the size of 0.0025m×0.030m×0.24 m. The Young's modulus of bronze is 1.00×10^{11} N/m², so the interfloor stiffness is 1.36×10^4 N/m. The structure was initially healthy with all original columns intact, and the natural frequency of the first to the fifth mode is 3.39Hz ,9.89Hz, 15.59Hz, 20.03 Hz and 22.84 Hz, respectively.

The damage was introduced by replacing columns by weak columns with the size of 0.0030m×0.0060m×0.24 m, shown in Figure 3. By replacing two columns in a story, the story stiffness was reduced by 33%.



Figure 3. Healthy (Left) and Damaged (Right) Columns

Under the basement of the structure, there were some bearings so that the structure could have a ground motion. The force input to the structure is provided with an electrodynamic shaker as shown in Figure 4. One acceleration sensor was installed on the basement to measure the ground motion. The sensor installed on each floor plate was used to measure the acceleration response of each floor.

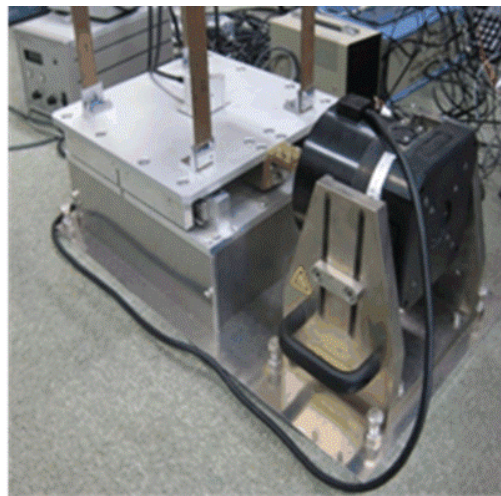


Figure 4. Bearings and Shaker

4 PROCEDURE

The 5-story structure was initially healthy with all original columns intact. The force input to the structure was provided by the shaker to obtain the acceleration data of the 5th story of the structure in normal state. Then, two columns of the first story were then replaced by weaker

columns (of the same material and integrity as healthy columns but with a smaller cross-sectional area) to simulate the abnormal state of the structure as stiffness reduction at a single story. The abnormal state of stiffness reduction at two stories was simulated by replacing two columns of the 1st story as well as those of the 3rd story. Finally, two columns of the 5th floor were also replaced to simulate the abnormal state case of stiffness reduction at three stories.

For only small completely vibration of the experimental setup is needed, and also considering avoiding the resonance region, a 1.1-Hz sine wave was used as the input signal in the experiments. Part of the input signal (0 to 20 s) is shown in Figure 5. The response of the experiential structure was recorded for 30s at a sampling frequency of 100 Hz; the total data length was 3000.

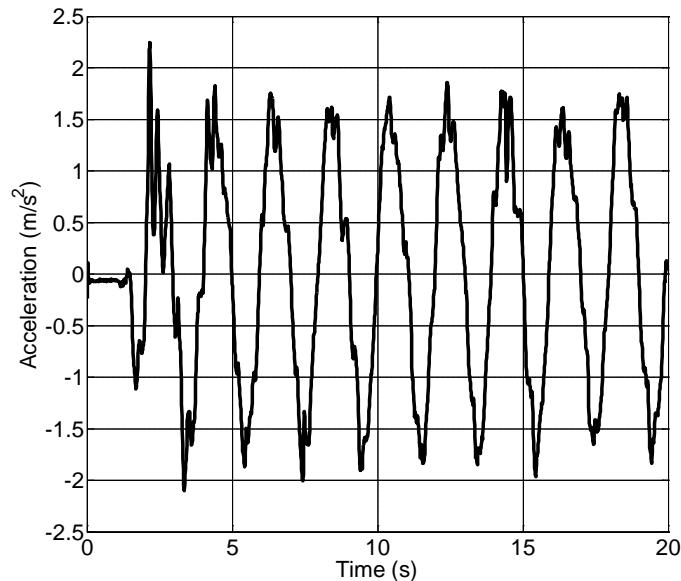


Figure 5. One typical acceleration signal

5 DAMAGE IDENTIFICATION RESULTS

The results summarized in Tables 1~4 show that RMSe is acceptable with our proposed method. In the verification, every case is calculated 10 times independently and average RMSe can be obtained. The average RMSe for each case is 3.64%, 3.63%, 3.82% and 3.88%, respectively. The trend is same as that of numerical simulation.

Table 1. Results of experimental verification of original structure. (Unit is 10 kN/m)

	True stiffness	Process number									
		1	2	3	4	5	6	7	8	9	10
k1	1.36	1.34	1.36	1.38	1.40	1.39	1.35	1.35	1.34	1.33	1.33
k2	1.36	1.37	1.40	1.34	1.36	1.34	1.34	1.39	1.38	1.32	1.37
k3	1.36	1.37	1.35	1.36	1.33	1.39	1.34	1.37	1.38	1.36	1.36
k4	1.36	1.33	1.37	1.38	1.33	1.34	1.37	1.36	1.35	1.38	1.32
k5	1.36	1.33	1.34	1.39	1.34	1.40	1.36	1.39	1.37	1.40	1.35
RMSe (%)	0.00	3.63	3.40	3.37	4.35	4.35	2.62	3.37	2.65	4.82	3.83

Table 2. Results of experimental verification of single-damage case. (Unit is 10 kN/m)

	True stiffness	Process number									
		1	2	3	4	5	6	7	8	9	10
k1	0.91	0.92	0.90	0.92	0.92	0.90	0.89	0.90	0.90	0.91	0.91
k2	1.36	1.35	1.35	1.38	1.36	1.35	1.39	1.35	1.34	1.39	1.36
k3	1.36	1.38	1.37	1.36	1.36	1.38	1.36	1.36	1.34	1.36	1.33
k4	1.36	1.34	1.38	1.36	1.38	1.36	1.37	1.34	1.34	1.34	1.34
k5	1.36	1.37	1.33	1.36	1.38	1.35	1.37	1.38	1.36	1.39	1.35
RMSe (%)	0.00	3.63	4.17	2.21	3.40	3.08	3.60	3.73	3.92	5.01	3.52

Table 3. Results of experimental verification of double-damage case. (Unit is 10 kN/m)

	True stiffness	Process number									
		1	2	3	4	5	6	7	8	9	10
k1	0.91	0.91	0.93	0.92	0.89	0.89	0.91	0.92	0.93	0.93	0.90
k2	1.36	1.33	1.35	1.34	1.34	1.35	1.35	1.36	1.38	1.39	1.38
k3	0.91	0.91	0.90	0.90	0.90	0.92	0.91	0.90	0.91	0.90	0.89
k4	1.36	1.36	1.38	1.34	1.37	1.37	1.34	1.35	1.35	1.37	1.38
k5	1.36	1.38	1.36	1.33	1.35	1.36	1.34	1.38	1.34	1.36	1.39
RMSe (%)	0.00	4.07	3.45	4.92	3.63	2.62	3.16	2.96	3.80	4.25	5.39

Table 4. Results of experimental verification of triple-damage case. (Unit is 10 kN/m)

	True stiffness	Process number									
		1	2	3	4	5	6	7	8	9	10
k1	0.91	0.92	0.91	0.93	0.90	0.90	0.89	0.94	0.92	0.91	0.92
k2	1.36	1.33	1.35	1.38	1.34	1.38	1.37	1.37	1.34	1.37	1.38
k3	0.91	0.91	0.92	0.91	0.92	0.91	0.93	0.90	0.90	0.90	0.90
k4	1.36	1.35	1.36	1.34	1.34	1.35	1.35	1.39	1.37	1.35	1.34
k5	0.91	0.90	0.91	0.90	0.93	0.92	0.93	0.94	0.95	0.89	0.88
RMSe (%)	0.00	3.88	1.54	3.95	4.02	2.95	4.00	5.75	4.70	3.35	4.68

6 CONCLUSION

In this paper, the parameter identification method based on STSA and AICSA was experimentally verified using a 5-story experimental model. The 5-story structure was initially healthy with all original columns intact. Two columns of one floor were then replaced by weak columns to simulate a single-damage case. The double-damage or triple-damage case was simulated by replacing the columns of two or three different floors, respectively. Under the basement of the structure, there were some bearings so that the structure could have a ground motion. The experimental results have shown that the proposed approach can successfully identify parameters of structure utilizing measured acceleration information for various damage scenarios under different excitation conditions. The proposed approach was shown promising for application of SHM on buildings.

REFERENCES

- [1]. Li R, Mita A. Structural damage identification using adaptive immune clonal selection algorithm and acceleration data[C]//SPIE Smart Structures and Materials+ Nondestructive Evaluation and Health Monitoring. International Society for Optics and Photonics, 2011: 79815A-79815A-10.
- [2]. Li R, Mita A, Zhou J. Hybrid Methodology for Structural Health Monitoring Based on Immune Algorithms and Symbolic Time Series Analysis[J]. Journal of Intelligent Learning Systems & Applications, 2013, 5(1).
- [3]. Li R, Mita A, Zhou J. Symbolization-based differential evolution strategy for identification of structural parameters[J]. Structural Control and Health Monitoring, 2013, 20(10): 1255-1270.
- [4]. Li R, Mita A, Zhou J. Feasibility Study of Parameter Identification Method Based on Symbolic Time Series Analysis and Adaptive Immune Clonal Selection Algorithm[J]. Open Journal of Civil Engineering, 2012, 2: 198.

A MATLAB Toolbox for Misconceptions Analysis Based on S-P Chart, Grey Relational Analysis and ROC

Tian-Wei Sheu, Phuoc-Hai Nguyen, Phung-Tuyen Nguyen, Duc-Hieu Pham, Ching-Pin Tsai and Masatake Nagai

Graduate Institute of Educational Measurement, National Taichung University of Education, Taichung, Taiwan;

sheu@mail.ntcu.edu.tw, phuochai1979@gmail.com, tuyennguyenphung@gmail.com, hieuhagdthsp2@gmail.com, tsai.chenbin@msa.hinet.net, nagai@kamakuranet.ne.jp

ABSTRACT

The purpose of this study is to design a MATLAB toolbox for misconceptions analysis based on Student-Problem Chart (S-P Chart), Grey Relational Analysis (GRA), and Receiver Operating Characteristic (ROC). Misconceptions analysis is actually necessary for teachers as well as students to improve teaching and learning process. Moreover, it is not only an objective research method, but also can evaluate the comprehensive academic achievement of students, and can select problems for the test. However, there is a difficult problem of the calculation for this method. Therefore, the design of a MATLAB toolbox for misconceptions analysis is necessary. This toolbox not only helps to process data quickly and accurately, but also displays the results on a graphical user interface visually. The experimental results show that this toolbox is actually useful for teachers in analyzing and evaluating the learning performance of students, and helps researchers to perform their educational researches more convenient.

Keywords: MATLAB toolbox, misconceptions analysis, S-P Chart, GRA, ROC.

1 INTRODUCTION

In the field of education, when teachers provide instruction on concepts in various subjects, they are teaching students who already have some pre-instructional knowledge about the topic. Knowledge of students can be erroneous, illogical or misinformed. These erroneous understandings are termed alternative conceptions or misconceptions. Misconceptions analysis is an integral and vital part of teaching and learning, providing feedback on progress through the assessment period to both students and teachers [1].

In recent years, many studies of misconceptions have been carried out in different countries and at all educational levels from elementary school to universities [2]. Thus, the study of methods to determine misconceptions is necessary for misconceptions analysis. In 2013, Sheu, T. W., et al., [3, 4] proposed a method for misconceptions analysis based on Student-Problem Chart, Grey Relational Analysis, and Receiver Operating Characteristic, that produced an analysis from a small amount of students and problems. It points out that which areas are the most important to address in the structure of concepts. Teachers can use this system as a reference when conducting remedial teaching. At this time, this method is becoming more relevant in education. This method provides teachers both effective and objective tool for research in teaching.

In 1969, Takahiro Sato proposed S-P Chart that could be used not only to display the diagnostic assessment of learning, but also give full play to improve the effectiveness of the curriculum. The S-P chart analysis could provide the two caution indices. One is the caution index for students (*CS*), and the other is the caution index for problems (*CP*). With these two indices, the researchers could select items with proper qualities and understand the cognition and learning condition of students [5]. Deng first introduced the grey system theory in 1982, and then it is applied to treat small amount insufficient information data. The data can be transformed from grey to white, and use to prediction and decision-making processes in the theory. Besides, the satisfactory prediction results with partially unknown parameters can be obtained. In grey system theory, there is a method of grey relational analysis which can treat uncertain, multiple, discrete, and incomplete information effectively. The main function of GRA is to calculate the discrete data and quantify the factors [6, 7]. Receiver operating characteristics graph is useful for organizing classifiers and visualizing their performance, it is commonly used in medical decision making. In recent years, it has been used increasingly in machine learning and data mining research [8]. The area under the ROC curve (*AUC*) is frequently used as a measure for the effectiveness of diagnostic markers. Its value can be interpreted as the probability that a classifier is able to distinguish a randomly chosen positive example from a randomly chosen negative example [9]. *AUC* is a measure for the diagnostic accuracy of a test and is often used to make comparisons between diagnostic tests or between observers [10].

In this paper, the researchers used a MATLAB toolbox based on Student-Problem Chart, Grey Relational Analysis, and Receiver Operating Characteristic to analyze misconceptions from the test results of the seventh grade mathematics for a class in Central Taiwan. This study is not only focused on the remedial instruction, but also noted how to enhance the quality of teaching strategies and how to choose students' learning misconceptions, and provide the teaching ideas to achieve the most effective teaching.

2 BASIC THEORIES

2.1 Student - Problem Chart Theory

The S-P Chart theory was first proposed by Takahiro Sato in 1969 [11]. Sato's method is to do analysis and sorting based on students' response pattern in the items. The analysis and sorting results can be used to get item quality and the students' diagnostic messages for teachers' effective learning [12]. The coefficient used for individual students and problems by S-P chart is caution index which is provided in caution index for student (CS) and caution index for item (CP). Caution index is mainly used as an index to judge students or questions whether are anomalies in response patterns. CS and CP are defined as follows [13, 14] (as shown in Table 1). Let item responses be

$$X = [x_{ij}], \quad x_{ij} = \begin{cases} 1, & \text{if answer is right} \\ 0, & \text{if answer is wrong} \end{cases} \quad (1)$$

and the number of student is $S_i, i = 1, 2, \dots, m$, the number of problem is $P_j, j = 1, 2, \dots, n$.

Caution index for students (CS) are defined as follow:

$$CS_i = 1 - \frac{\sum_{j=1}^n (x_{ij})(x_{\bullet j}) - (x_{i\bullet})(\bar{x})}{\sum_{j=1}^n (x_{\bullet j}) - (x_{i\bullet})(\bar{x})} \quad (2)$$

where $\bar{x} = \frac{1}{n} \sum_{j=1}^n x_{\bullet j}$ and $N = x_{i\bullet} = \sum_{j=1}^n x_{ij}$

Table 1: S-P Chart

	Problem number $P_j, j = 1, 2, \dots, n$	Total score	CS
Student number $S_i, i = 1, 2, \dots, m$	$X = [x_{ij}]_{m \times n}$	High \updownarrow Low	SS_i CS_i
Number of correct answer	More \leftarrow Less PP_j	$\sum_{i=1}^m SS_i = \sum_{j=1}^n PP_j$	
CP	CP_j		

and caution index for problems (CP):

$$CP_j = 1 - \frac{\sum_{i=1}^m (x_{ij})(x_{i\bullet}) - (x_{\bullet j})(\bar{x}')}{M \sum_{i=1}^m (x_{i\bullet}) - (x_{\bullet j})(\bar{x}')} \tag{3}$$

where $\bar{x}' = \frac{1}{m} \sum_{i=1}^m x_{i\bullet}$ and $M = x_{\bullet j} = \sum_{i=1}^m x_{ij}$

2.2 Grey Relational Analysis

The GRA method can make the analysis more concrete and accurate, and the uncertain factors in the studies can also be analyzed [12]. The GRA procedures are shown as follows.

2.2.1 Establishing the raw data analysis

For setting up the GRA, there must be reference vector x_0 and comparative vector x_i , and they are shown as follows.

$$x_0 = (x_0(1), x_0(2), \dots, x_0(k), \dots, x_0(m)) \tag{4}$$

where $k = 1, 2, \dots, m$

$$\left. \begin{aligned} x_1 &= (x_1(1), x_1(2), \dots, x_1(k), \dots, x_1(m)) \\ x_2 &= (x_2(1), x_2(2), \dots, x_2(k), \dots, x_2(m)) \\ &\vdots \\ x_i &= (x_i(1), x_i(2), \dots, x_i(k), \dots, x_i(m)) \\ &\vdots \\ x_n &= (x_n(1), x_n(2), \dots, x_n(k), \dots, x_n(m)) \end{aligned} \right\} \tag{5}$$

where $i = 1, 2, \dots, n$

2.2.2 Generations of grey relation

During the GRA process, researchers need to extract the available data by satisfying three rules, and they are: non-dimension, scaling and polarization. There are three methods to generate and standardize the data, and they are: larger-the-better, smaller-the-better, and nominal-the-better. In this paper, the researchers only use larger-the-better method. It is shown as follows.

$$x_i^*(k) = \frac{x_i(k) - \min_{\forall i} x_i(k)}{\max_{\forall i} x_i(k) - \min_{\forall i} x_i(k)} \tag{6}$$

where $\max_{\forall i} x_i(k)$ means the maximum number in j , and $\min_{\forall i} x_i(k)$ means the minimum number in j .

2.2.3 Calculations of Grey Relational

Based on Nagai's equation [15], the grey relation can be calculated in this paper when partial grey relation's reference vector is x_0 and comparative vector is x_j . When γ_{0i} is close to 1, it means that x_0 and x_j are highly related to each other. The equation of the localized grey relation is shown as follows.

$$\gamma_{0i} = \gamma(x_0(k), x_i(k)) = \frac{\bar{\Delta}_{\max} - \bar{\Delta}_{0i}}{\bar{\Delta}_{\max} - \bar{\Delta}_{\min}} \quad (7)$$

where $\bar{\Delta}_{0i} = \|x_{0i}\|_{\rho} = \left(\sum_{k=1}^n [\Delta_{0i}(k)]^{\rho} \right)^{\frac{1}{\rho}}$, $\bar{\Delta}_{\max}$ represents the maximum of $\bar{\Delta}_{0i}$, and $\bar{\Delta}_{\min}$ represents the minimum of $\bar{\Delta}_{0i}$. When $\rho \geq 1, 2, \dots, m$, it means Minkowski's grey relation; when $\rho = 2$, it means Euclidean grey relation.

2.2.4 Grey relational grade

The decision-making is based on the comparison of the grey relation. Though ranking, we can find out an importance of the factors and then identify the maximum or minimum of impact factors. The factors become the associated principle of the system.

2.3 Receiver Operating Characteristic

Receiver operating characteristics are a powerful statistical modeling tool which can be used in decision making, particularly when setting threshold values for tests. Receiver operating characteristic curves are a graphical plot of sensitivity of a test and 1-specificity for a binary classifier system as the test threshold varies. In order to construct an ROC curve the researchers need to calculate the Se and Sp of the test for each possible cut point value, and they are shown as follows.

Table 2: The contingency table

	Actual Value	
Prediction Outcome	True Positive (a)	False Positive (b)
	False Negative (c)	True Negative (d)

$$\text{Sensitivity (Se)} = \frac{a}{a+b} \quad (8)$$

$$\text{Specificity (Sp)} = \frac{d}{c+d} \quad (9)$$

$$\text{AUC} = \frac{\text{Se} \cdot (1 - \text{Sp})}{2} + \frac{(\text{Se} + 1) \cdot \text{Sp}}{2} \quad (10)$$

The area under the ROC curve (*AUC*) is a summary statistic of diagnostic performance. The *AUC* could distinguish between non-predictive ($\text{AUC} < 0.5$), less predictive ($0.5 \leq \text{AUC} < 0.7$), moderately predictive ($0.7 \leq \text{AUC} < 0.9$), highly predictive ($0.9 \leq \text{AUC} < 1$) and perfect prediction ($\text{AUC} = 1$) [16-17].

ROC Analysis Method

The analysis steps of ROC as follows:

Step 1: Establishing the response result of students

$$\text{Let } X = [x_{ij}]_{m \times n}, x_{ij} = \begin{cases} 1, & \text{if answer is right} \\ 0, & \text{if answer is wrong} \end{cases} \quad (11)$$

be the response result of students, analysis results of S-P Chart are shown in Table 1.

Step 2: The set of positive and negative class labels of students and problems are defined in definitions 1.

Definition 1: The prediction matrix for students

The state setting of positive “1” and negative “0” in prediction matrix $[d_{ij}]_{m \times n}$ is determined by the following formula:

$$D_S = [d_{ij}]_{m \times n}, d_{ij} = \begin{cases} 1, & \text{if } j \leq SS_i \\ 0, & \text{if } j > SS_i \end{cases} \quad (12)$$

where SS_i is the score of *i*-th student in S-P chart, $D_S = [d_{ij}]_{m \times n}$ is the matrix that predicts states of positive and negative of students.

Definition 2: The prediction matrix for problems

The state setting of positive “1” and negative “0” in prediction matrix $[d'_{ij}]_{m \times n}$ is determined by the following formula:

$$D_P = [d'_{ij}]_{m \times n}, d'_{ij} = \begin{cases} 1, & \text{if } i \leq PP_j \\ 0, & \text{if } i > PP_j \end{cases} \quad (13)$$

where PP_j is the number of correct answer of *j*-th problem in S-P chart, $D_P = [d'_{ij}]_{m \times n}$ is the matrix that predicts states of positive and negative of problems.

Step 3: The researchers calculated AUC values based on the response result of students $[x_{ij}]_{m \times n}$ with the prediction matrix $[d_{ij}]_{m \times n}$ and $[d'_{ij}]_{m \times n}$. When the student answered all problems correctly for the whole test, his (her) AUC value is set of "1", in contrast, when he (she) did not answer any problem correctly, his (her) AUC value is set of "0". Similarly, when the problem is answered correctly by all students in the group of student surveyed, its AUC value is set of "1", in contrast, when it is not answered correctly by any student, its AUC value is set of "0". According to the AUC values, the researchers analyzing items through the epsilon (ϵ) threshold was equal to 0.7 in this study. Because the AUC could distinguish between non-predictive ($AUC < 0.5$), less predictive ($0.5 \leq AUC < 0.7$), moderately predictive ($0.7 \leq AUC < 0.9$), highly predictive ($0.9 \leq AUC < 1$) and perfect prediction ($AUC = 1$) [18].

2.4 The Method of Analyzing Misconceptions

The synthesis of the results of the S-P Chart, GRA and ROC allows to analyze the misconceptions based on the given conditions as follows:

Definition 3: Misconceptions of students

Misconceptions of students (M_S) that are defined by the following formula:

$$M_S = \left\{ x_i \left| \begin{array}{l} \gamma_S > 0.5, CS_i \geq 0, AUC_i < \epsilon \\ \gamma_S \leq 0.5, 0 < CS_i \leq 0.75, AUC_i < \epsilon \end{array} \right. \right\} \quad (14)$$

where $i = 1, 2, \dots, m$.

In misconceptions of students (M_S), the students have Gamma value (γ_S) that are greater than 0.5 from S-P Chart, caution index for students (CS_i) that are greater than or equal to 0, and AUC values (AUC_i) that are less than the epsilon (ϵ) threshold; and the students have Gamma value (γ_S) that are less than or equal to 0.5 from S-P Chart, caution index for students (CS_i) that are greater than 0 and less than or equal to 0.75, and AUC values (AUC_i) that are less than the epsilon (ϵ) threshold [19-22].

Definition 4: Misconceptions of problems

Misconceptions of problems (M_P) that are defined by the following formula:

$$M_P = \left\{ x_j \left| \begin{array}{l} \gamma_P > 0.5, CP_j \geq 0, AUC_j < \epsilon \\ \gamma_P \leq 0.5, 0 < CP_j \leq 0.75, AUC_j < \epsilon \end{array} \right. \right\} \quad (15)$$

where $j = 1, 2, \dots, n$.

In misconceptions of problems (M_P), the problems have Gamma value (γ_P) that are greater than 0.5 from S-P Chart, caution index for problems (CP_j) that are greater than or equal to 0, and AUC values (AUC_j) that are less than the epsilon (ϵ) threshold; and the problems have Gamma value (γ_P) that are less than or equal to 0.5 from S-P Chart, caution index for students (CP_j) that are greater than 0 and less than or equal to 0.75, and AUC values (AUC_j) that are less than the epsilon (ϵ) threshold [19-22].

3 BUILDING TOOLBOX

3.1 Software Specifications and Requirements

- Windows 7, Windows 8 or upgrade versions.
- Screen resolution 1280×800.
- MATLAB R2012b version or upgrade versions.

This paper presents a sample program that is developed by MATLAB including many scientific functions due to supply an experiment environment on the computer, and then a reliable program can be developed. The program for misconceptions analysis has been developed by MATLAB R2012b software. Using this program depends on the user's knowledge about MATLAB.

3.2 The Program for Misconceptions Analysis

The program for misconceptions analysis has 6 basic steps.

Step 1: Input data.

Data is the response matrix of students that is numerical and written in *.csv file or *.xlsx file.

Step 2: Calculate student total, problem total, and Cronbach's Alpha value.

Step 3: S-P Chart.

Calculate students' total scores, correct answer of problems, and correct ratio. Next, arrange in order of students' total scores, and correct answer of problems. Then, calculate caution index for Student (CS), and Caution Index for Problem (CP), and design the table for results.

Step 4: Grey Relational Analysis (GRA).

Calculate GRA for students, and GRA for problems. Next, arrange in order of GRA for students, and GRA for problems. Then, drawing GRA graphs for students and problems.

Step 5: Receiver Operating Characteristic (ROC).

Calculating Sensitivity (Se), and Specificity (Sp). Next, calculate the area under the ROC curve (AUC). Then, draw ROC graphs for students and problems.

Step 6: Continue or exit program.

If new data is selected, the program will continue and back to step 1, or else the program will be ended. The main algorithms of the program are described in figure 1. The user can save the results and the graphs to *.csv file or *.xlsx file and jpeg image formatted.

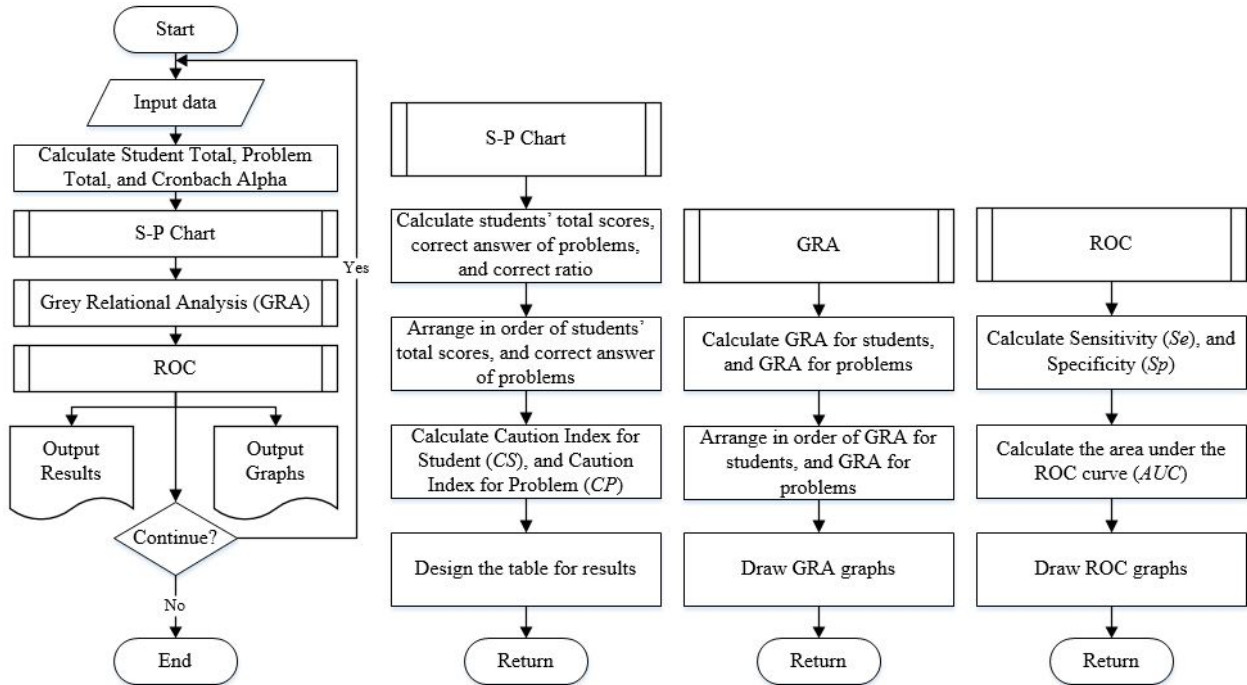


Figure 1: The flowchart for misconceptions analysis

4 EXPERIMENTAL RESULTS AND DISCUSSION

4.1 Working with the MATLAB Toolbox

The graphical user interface starts up when file “SPChart_GRA_ROC.m” is opened, the graphical user interface of program is displayed on the screen of the computer (Fig. 2 and Fig. 3). Firstly, the user needs to click the button “Input Data” to input the data. Data is the response matrix of students that is numerical and written in *.csv file or *.xlsx file. Secondly, the user clicks the button “Graphs for Students” or “Graphs for Problems”, and clicks the button “OK”, the program will process data, and then program displays the results and the graphs. In this panel, the user can clicks the button “Save Results” to save the results with *.csv file or *.xlsx file formatted, and clicks the button “Save Graphs” to save the graphs with *.JPG file formatted. Finally, if new data is selected, the program will continue, or else if the user clicks the button “Exit” the program will be ended.

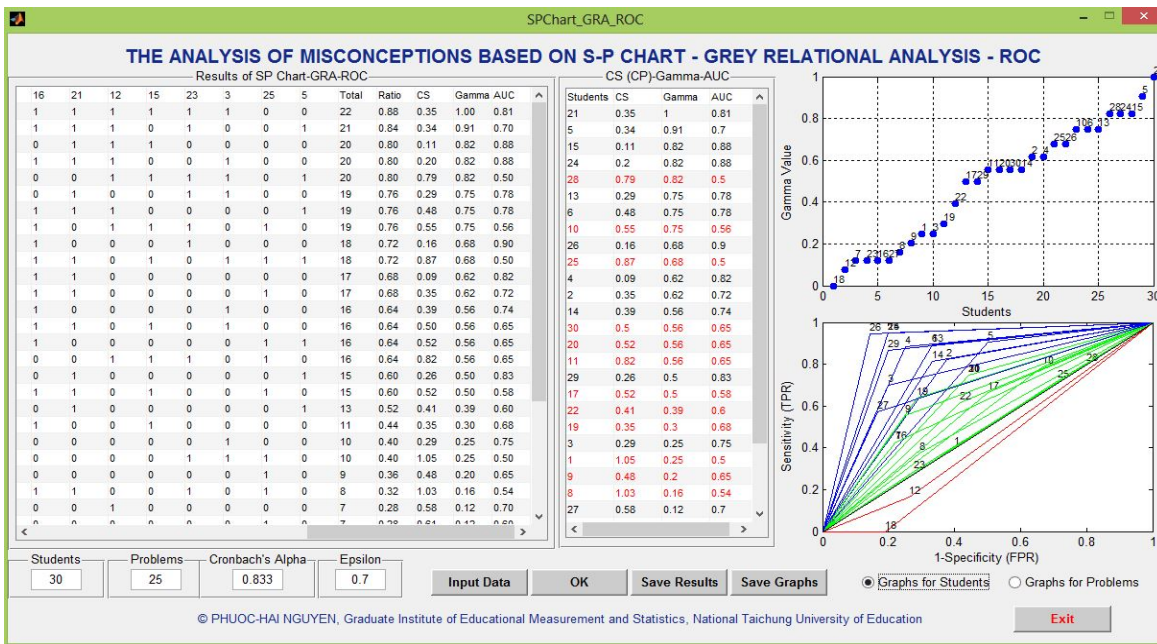


Figure 2: The graphical user interface of the toolbox for the results and the graphs of students

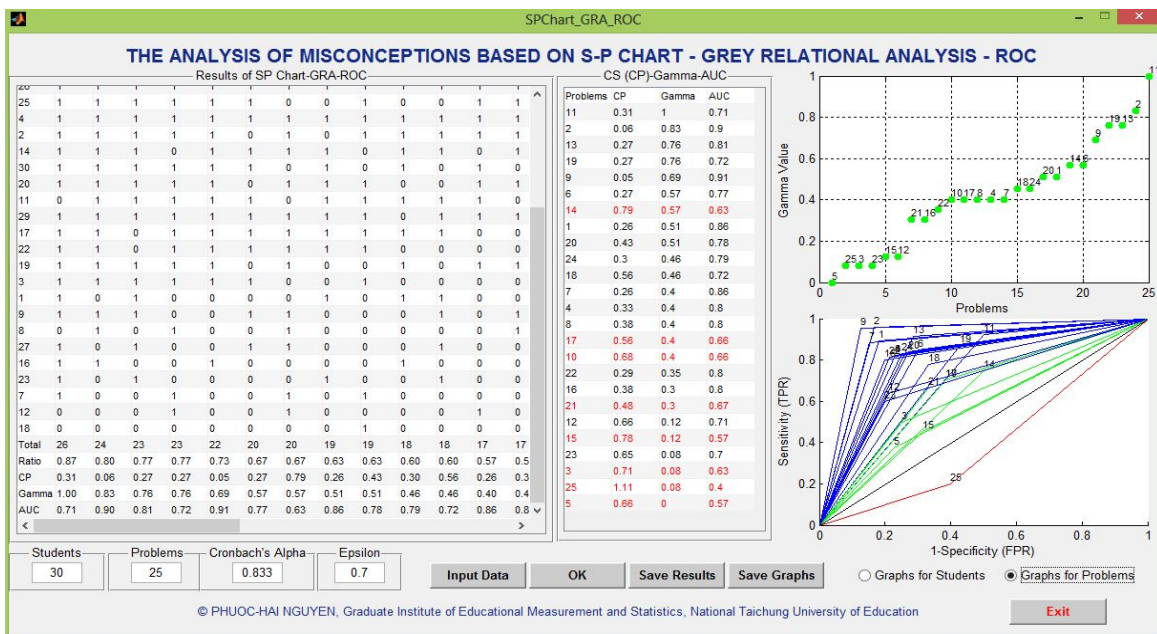


Figure 3: The graphical user interface of the toolbox for the results and the graphs of problems

4.2 Application Example

In this paper, the researchers used a MATLAB toolbox based on Student-Problem Chart, Grey Relational Analysis, and Receiver Operating Characteristic to analyze misconceptions from the test results of the seventh grade mathematics for a class in Central Taiwan. The number of students was 30 students and the number of items was 25 problems. This study carried out a reliability test for the answers by using Cronbach's Alpha coefficient. The results showed that

Cronbach's Alpha value of the test was $\alpha = 0.833$, which meant the reliability of the information was quite good. The results of the test is shown in table 3.

According to the results from figure 2 and table 3 showed that 17 students having *AUC* values are less than 0.7 ($S_{28}, S_{10}, S_{25}, S_{30}, S_{20}, S_{11}, S_{17}, S_{22}, S_{19}, S_1, S_9, S_8, S_{16}, S_{23}, S_7, S_{12}$, and S_{18}). However, six students having *Gamma* values are less than 0.5 and *CS* values are greater than 0.75 ($S_1, S_8, S_{23}, S_7, S_{12}$, and S_{18}). The results from figure 3 and table 3 showed that eight problems having *AUC* values are less than 0.7 ($P_{14}, P_{17}, P_{10}, P_{21}, P_{15}, P_3, P_{25}$, and P_5). However, two problems having *Gamma* value are less than 0.5 and *CP* value is greater than 0.75 (P_{15} and P_{25}). The researchers determined misconceptions based on the given conditions of *Gamma* value, *CS* value, *CP* value, and *AUC* value of students and problems for this class. The result of analyzing misconceptions showed that 11 students have misconceptions ($S_{28}, S_{10}, S_{25}, S_{30}, S_{20}, S_{11}, S_{17}, S_{22}, S_{19}, S_9$, and S_{16}), and six problems have misconceptions in this class ($P_{14}, P_{17}, P_{10}, P_{21}, P_3$, and P_5). The results from figure 2, figure 3, figure 4, and table 3 showed that this toolbox not only helps to process data accurately, but also displays the results on a graphical user interface visually.

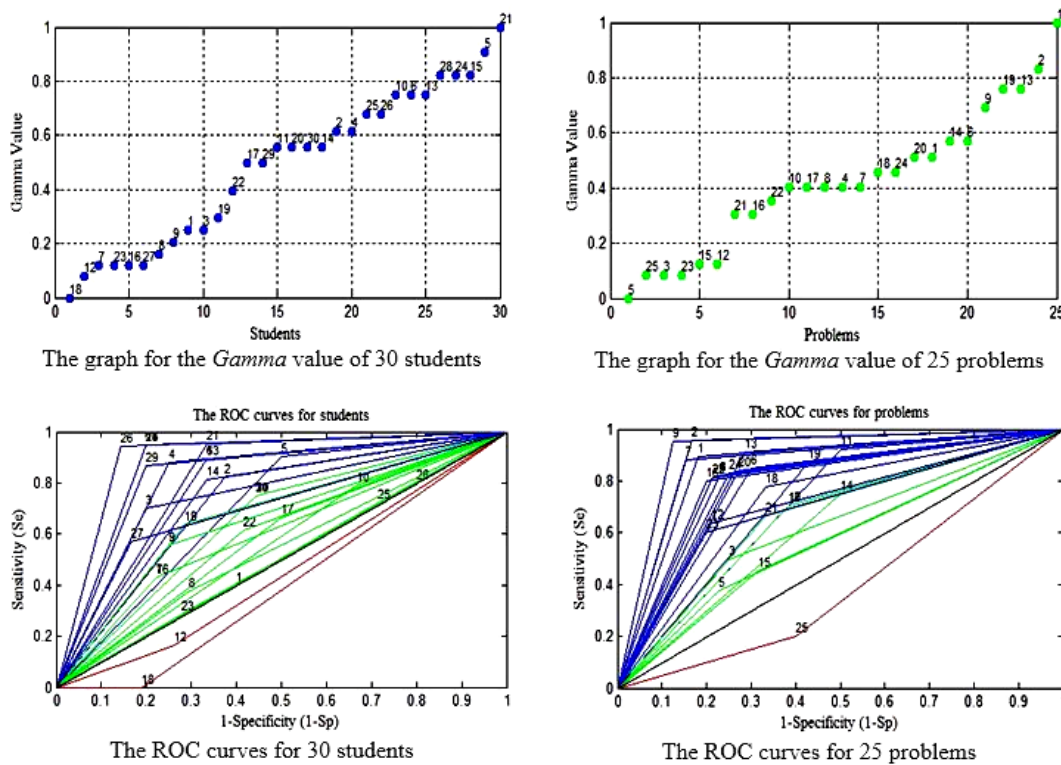


Figure 4: The graphs of application example

Table 3: The results of application example

S \ P	11	2	13	19	9	6	14	1	20	24	18	7	4	8	17	10	22	16	21	12	15	23	3	25	5	Total	Ratio	CS	GS	AUC
21	1	1	1	1	1	1	1	1	1	1	0	1	1	1	1	1	1	1	1	1	1	1	1	0	0	22	0.88	0.35	1.00	0.81
5	1	1	1	1	1	1	1	1	1	1	1	1	1	1	1	0	1	1	1	1	0	1	0	0	1	21	0.84	0.34	0.91	0.70
15	1	1	1	1	1	1	1	1	1	1	1	1	1	1	1	1	0	1	1	1	1	0	0	0	0	20	0.80	0.11	0.82	0.88
24	1	1	1	1	1	1	1	1	1	1	1	1	1	0	1	1	1	1	1	1	0	0	1	0	0	20	0.80	0.20	0.82	0.88
28	1	1	1	1	1	1	0	1	1	1	1	1	1	1	0	1	1	0	0	1	1	1	1	0	1	20	0.80	0.79	0.82	0.50
13	1	1	1	1	1	1	1	1	1	1	1	0	1	1	1	1	0	1	0	0	1	1	0	0	0	19	0.76	0.29	0.75	0.78
6	1	1	1	1	1	1	0	1	0	1	1	1	1	1	1	1	1	1	1	1	0	0	0	0	1	19	0.76	0.48	0.75	0.78
10	1	1	1	1	1	1	1	1	1	1	1	1	0	1	1	0	0	1	0	1	1	1	0	1	0	19	0.76	0.55	0.75	0.56
26	1	1	1	1	1	1	1	1	1	1	1	1	1	1	0	1	1	1	0	0	0	1	0	0	0	18	0.72	0.16	0.68	0.90
25	1	1	1	1	1	1	0	0	1	0	0	1	1	0	1	1	1	1	1	0	1	0	1	1	1	18	0.72	0.87	0.68	0.50
4	1	1	1	1	1	1	1	1	1	1	1	1	1	1	0	0	1	1	1	1	0	0	0	0	0	17	0.68	0.09	0.62	0.82
2	1	1	1	1	1	0	1	0	1	1	1	1	1	1	0	1	1	1	1	0	0	0	0	0	1	17	0.68	0.35	0.62	0.72
14	1	1	1	0	1	1	1	1	0	1	1	0	1	1	1	1	1	1	0	0	0	0	0	1	0	16	0.64	0.39	0.56	0.74
30	1	1	1	1	1	1	0	1	0	1	0	1	0	1	1	1	0	1	1	0	1	0	1	0	0	16	0.64	0.50	0.56	0.65
20	1	1	1	1	1	0	1	1	1	0	0	1	1	1	0	1	1	1	0	0	0	0	0	0	1	16	0.64	0.52	0.56	0.65
11	0	1	1	1	1	1	0	1	1	1	1	1	0	1	1	0	0	0	0	1	1	1	0	1	0	16	0.64	0.82	0.56	0.65
29	1	1	1	1	1	1	1	1	1	0	1	1	1	0	1	0	0	0	1	0	0	0	0	0	1	15	0.60	0.26	0.50	0.83
17	1	1	0	1	1	1	1	1	1	1	0	0	0	0	0	0	1	1	1	0	1	0	0	0	1	15	0.60	0.52	0.50	0.58
22	1	1	0	1	1	1	1	1	1	0	0	0	0	1	1	1	0	0	1	0	0	0	0	0	1	13	0.52	0.41	0.39	0.60
19	1	1	1	1	1	0	1	0	0	1	0	1	1	0	0	0	0	1	0	0	1	0	0	0	0	11	0.44	0.35	0.30	0.68
3	1	1	1	1	1	1	0	0	1	0	0	0	0	0	1	1	0	0	0	0	0	0	1	0	0	10	0.40	0.29	0.25	0.75
1	1	0	1	0	0	0	0	1	0	1	1	0	0	0	1	0	1	0	0	0	0	1	1	1	0	10	0.40	1.05	0.25	0.50
9	1	1	1	0	0	1	1	0	0	0	1	0	1	0	1	0	0	0	0	0	0	0	0	1	0	9	0.36	0.48	0.20	0.65
8	0	1	0	1	0	0	1	0	0	0	0	0	1	0	0	0	0	1	1	0	0	1	0	1	0	8	0.32	1.03	0.16	0.54
27	1	0	1	0	0	1	1	0	0	0	1	0	0	0	1	0	0	0	0	1	0	0	0	0	0	7	0.28	0.58	0.12	0.70
16	1	1	0	0	1	0	0	0	0	1	0	0	0	1	0	1	0	0	0	0	0	0	0	0	1	7	0.28	0.61	0.12	0.60
23	1	0	1	0	0	0	0	1	0	0	1	0	0	0	0	1	0	0	0	1	1	0	0	0	0	7	0.28	0.83	0.12	0.50
7	1	0	0	1	0	0	1	0	1	0	0	0	0	0	1	0	0	0	0	0	0	1	0	0	1	7	0.28	0.88	0.12	0.60
12	0	0	0	1	0	0	1	0	0	0	0	1	0	0	0	0	1	0	1	0	0	0	1	0	0	6	0.24	1.01	0.08	0.45
18	0	0	0	0	0	0	0	0	1	0	0	0	0	0	0	1	0	0	0	1	1	0	0	0	0	4	0.16	1.34	0.00	0.40
Total	26	24	23	23	22	20	20	19	19	18	18	17	17	17	17	17	16	15	15	11	11	10	10	10	8	423				
Ratio	0.870	0.800	0.770	0.770	0.730	0.670	0.670	0.630	0.630	0.600	0.600	0.570	0.570	0.570	0.570	0.570	0.530	0.500	0.500	0.370	0.370	0.330	0.330	0.330	0.27					
CP	0.310	0.060	0.270	0.270	0.050	0.270	0.790	0.260	0.430	0.300	0.560	0.260	0.330	0.380	0.560	0.680	0.290	0.380	0.480	0.660	0.780	0.650	0.711	1.10	0.66					
GP	1.000	0.830	0.760	0.690	0.570	0.570	0.510	0.510	0.460	0.460	0.400	0.400	0.400	0.400	0.350	0.300	0.300	0.120	0.120	0.080	0.080	0.080	0.00	0.00						
AUC	0.710	0.900	0.810	0.720	0.910	0.770	0.630	0.860	0.780	0.790	0.720	0.860	0.800	0.800	0.660	0.660	0.800	0.800	0.670	0.710	0.570	0.700	0.630	0.400	0.57					

S = 30
P = 25

5 CONCLUSION

Based on the findings from this study, some viewpoints and suggestions are discussed as follows.

- This study has successfully developed a MATLAB toolbox for misconceptions analysis based on S-P Chart, GRA, and ROC. This toolbox has many advantages such as: easy for use, time-saving, accurate and clearly visual output. Especially, the user can save the results and the graphs to *.csv file or *.xlsx file and jpeg image formatted.
- This toolbox is not only an objective research method, but also helps teachers to diagnose the situation exploration of student learning. This will be essential tool to innovate teaching methods and training quality management in education.
- This toolbox is actually useful for teachers as well as students to improve teaching and learning process. Teachers can use it as a reference when conducting remedial teaching. At this time, this toolbox is becoming more relevant in education. This method provides teachers both effective and objective tool for research in teaching.

In conclusion, this toolbox is actually useful for teachers in analyzing and evaluating the learning performance of students, selecting problems in the teaching process, and helps researcher convenience to conduct their educational researches.

REFERENCES

- [1]. Bambico, T., Mathematical Strengths, Difficulties and Misconceptions of Teachers: Analysis of Their Performance in an Achievement Test. *Journal of International Development and Cooperation*, 2002. 9(1): p. 41-60.
- [1]. Çelikten, O., S. İpekçioğlu, H. Ertepinar, and Ö. Geban, The effect of the conceptual change oriented instruction through cooperative learning on 4th grade students' understanding of earth and sky concepts. *Science Education International*, 2012. 23(1): p. 84-96.
- [2]. Sheu, T. W., P. H. Nguyen, P. T. Nguyen, D. H. Pham, C. P. Tsai, and M. Nagai, Using S-P Chart, Grey Relational Analysis, and Receiver Operating Characteristic to Analyze Misconceptions. *International Conference on Grey System Theory and Kansei Engineering Conference*, 2013. p. 25-32.
- [3]. Sheu, T. W. P. H. Nguyen, P. T. Nguyen, D. H. Pham, C. P. Tsai, and M. Nagai, The Analysis of Misconceptions Based on S-P Chart, Grey Relational Analysis, and Receiver Operating Characteristic. *International Journal of Kansei Information*, 2014. 5(1): p. 1-12.
- [4]. Lin, Y. H., and S. M. Chen, "The Investigation of S-P Chart Analysis on the Test Evaluations of Equality Axiom Concepts for Sixth Graders," *Proceedings of the 2nd WSEAS/IASME International Conference on Educational Technologies*, Bucharest, Romania, 2006.
- [5]. Deng, J. Introduction to Grey System Theory. *Journal of Grey System*, 1989. 1: p. 1-24.
- [6]. Liang, J. C., T. W. Sheu, J. W. Tzeng, B. T. Wang, and M. Nagai, 5W1H, GRA and GSM in the evaluation and identify on optimal design of bike lamps. *Journal of Convergence Information Technology (JCIT)*, 2011. 6(12): p. 266-274.
- [7]. Fawcett, T., An introduction to ROC analysis. *Pattern Recognition Letters*, 2006. 27: p. 861-874.
- [8]. Faraggi, D., and B. Reiser, Estimation of the area under the ROC curve. *Statistics In Medicine*, 2001. 21: p. 3093-3106.
- [9]. Nguyen, P. H., T. W. Sheu, P. T. Nguyen, D. H. Pham, C. P. Tsai, and M. Nagai, Based on WPOT Combines with ROC Concepts Structure Analysis and Cognitive Diagnostic. *Kansei Information of Creative Contest*, Chien Kuo Technology University, Taichung, Taiwan, 2013. p. 21-29.
- [10]. Sheu, T. W., T. L. Chen, J. W. Tzeng, C. P. Tsai, and M. Nagai, Study on the Conception of Learning Problems of Students by Combining the Misconception Domain and Structural Analysis Methods. *Journal of Computers*, 2013. 8(5): p. 1255-1266.

- [11]. Sheu, T. W., P. H. Nguyen, P. T. Nguyen, and D. H. Pham, A Matlab Toolbox for AHP and LGRA-AHP to Analyze and Evaluate Factors in Making the Decision. *International Journal of Kansei Information*, 2013. 4(3): p. 149-158.
- [12]. Sheu, T. W., D. H. Pham, P. T. Nguyen, and P. H. Nguyen, A Matlab Toolbox for Student-Problem Chart and Grey Student-Problem Chart and Its Application. *International Journal of Kansei Information*, 2013. 4(2): p. 75-86.
- [13]. Sheu, T. W., T. L. Chen, J. W. Tzeng, C. P. Tsai, H. J. Chiang, C. L. Chang, and M. Nagai, Applying Misconception Domain and Structural Analysis to Explore the Effects of the Remedial Teaching. *Journal of Grey System*, 2013. 16(1): p. 17-34.
- [14]. Tzeng, J. W., T. W. Sheu, J. C. Liang, B. T. Wang, and M. Nagai, Study on GSP Chart of the Important Certification Indicators of the E-Learning Courses in Taiwan. *International Journal of Digital Content Technology and Its Application*, 2012. 6(9): p. 9-16.
- [15]. Hanley, J. A., and B. J. McNeil, The Meaning and Use of the Area under Receive Operating Characteristic (ROC) Curve. *European Journal of Radiology*, 1982. 143: p. 29-36.
- [16]. Arian, R., V. Erkel, M. Peter, and T. Pattynama, Receiver operating characteristic (ROC) analysis: Basic principles and applications in radiology. *European Journal of Radiology*, 1998. 27: p. 88-94.
- [17]. Faraggi, D., and B. Reiser, Estimation of the area under the ROC curve. *Statistics In Medicine*, 2001. 21: p. 3093-3106.
- [18]. Sheu, T. W., J. W. Tzeng, C. P. Tsai, and , and T. L. Chen, Applying Problem-Concept Chart Combined with Structural Analysis to Investigate the Learning Misconcept-Simple Equation with One Variable for Example. *Journal of Grey System*, 2012. 15(1): p. 56-66,
- [19]. Sheu, T. W., C. P. Tsai, J. W. Tzeng, T. L. Chen, and M. Nagai, An Algorithm of the Misconception Order. *Applied Mechanics and Materials*, 2013. 284-287: p. 3010-3014.
- [20]. Sheu, T. W., T. L. Chen, C. P. Tsai, J. W. Tzeng, C. P. Deng, and M. Nagai, Analysis of Students' Misconception Based on Rough Set Theory. *Journal of Intelligent Learning Systems and Applications*, 2013. 5:p. 67-83.
- [21]. Sheu, T. W., C. P. Tsai, J. W. Tzeng, T. L. Chen, H. J. Chiang, W. L. Liu, and M. Nagai, Using Rough Set and Grey Structural Model to Investigate the Structure of the Misconceptions' Domain. *Journal of Grey system*, 2012. 15(4): p. 205-220.

On Securing a Door with Finger Print Biometric Technique

Adeolu Afolabi, Oke Alice

*Department of Computer Science and Engineering
Ladoke Akintola University of Technology, Ogbomosho. Nigeria
adefolabius@yahoo.com*

Abstract

Security of valuables is as paramount as their acquisition. Valuables ranging from human lives to expensive resources and sensitive data need to be tightly secured. In this present day when armed robbery has gotten more sophisticated particularly in developing countries, there is the need for tighter security means, and one of the most secured technologies that can be employed is biometrics, finger print door lock to be precise. Biometrics is the science and technology of measuring and analysing biological data, biometrics measures and analyses human body characteristics such as DNA, fingerprint, eye retina and iris, voice pattern, facial pattern and hand measurement [1].

The software that drives the microcontroller was done using the C language on MPLAB compiler, the coding was segmented into various modules; first, the module that drives the LCD screen, next is the module that drives the finger print scanner, this instructs the scanner to first register users and allow the inputted finger print to be compared with the pre-registered finger prints. The pre-registered finger prints are saved on the IC registers of the Micro controller. An alert is sounded whenever a fingerprint that is not found in the Microcontroller memory is placed on the scanner as an intruder.

The construction of this project was done in three different stages, the writing of the code (driver) which controls the Microcontroller using C language, the implementation of the whole project on a solder-less experiment board, the soldering of the circuits on Vero-boards and the coupling of the entire project to the casing. The implementation of this project was done on the breadboard as a prototype, the power supply was first derived from a bench power supply in the electronics laboratory, in all the development guaranteed security for illegal intrusion of illegal entity to room, the mechanism can be implemented in a broader sense on a door where a there is restriction of access.

1 INTRODUCTION

The design of security door lock using the finger print technology was built around a microcontroller, PIC16F628A, which reads in finger prints from finger print scanner and grant access, to a protected room, only to pre-registered finger print(s).



Figure 1 The picture of the SN-FPR-UART finger print reader and PIC16F628A Microcontroller.

The finger print scanner serves as the main input into this security system. Finger prints read are compared to those ones pre-programmed into the memory of the microcontroller. When a match is made, the microcontroller outputs a HIGH which activates the transistor-relay switching stage that controls opening and closing of the modelled motorized door granting access into the protected building.

A 16x2 alphanumeric liquid crystal display is used in this design to show the operating status of this embedded security system. By default it displays a welcome message requesting that the user should enter a finger print. And when a match is made it displays a corresponding message. The stages that make up the design of the development of a finger print control using standard door finger print scanner are explained fully in the third chapter of this project report.

2 PRINCIPLE OF OPERATION

The design of security door lock using the finger print technology was built around a Micro-Controller Unit (MCU), PIC16F628A, which reads in finger prints from finger print scanner and grant access, to a protected compartment, only to pre-registered finger prints. The finger print scanner serves as the main input into this embedded security system. Finger prints read are compared to those ones pre-programmed into the memory of the microcontroller. When a match is made, the microcontroller outputs a HIGH which activates the transistor-relay switching stage that controls opening and closing of the modelled motorized door granting access into the protected building.

An alphanumeric liquid crystal display (LCD) is used in this design to show the operating status of this embedded security system. By default it displays a welcome message requesting that the user should enter a finger print. And when a match is made it displays "ACCESS GRANTED" otherwise it displays "ACCESS DENIED".

2.1 Hardware Design and Configuration

The hardware design of a security door using fingerprint is achieved by interfacing a SN-FPR-UART Finger reader with the PIC16F648A Microcontroller, which is the heart of the design, it is the brain box that controls the whole security door system. An LCD status display is employed to show the operating status of the system. A door movement mechanism is used in the design to make the automated door system move in clockwise and anti-clockwise directions.

2.1.1 SN-FPR-UART Fingerprint Reader

The finger print input stage was implemented using the SN-FPR-UART. It is a compact fingerprint reader module which is specially designed for project development because of its robustness and the following outstanding features:

- a) Small in size, clear imaging, fast acquisition, high identification speed, able to sense on dry or wet fingers, supports wide range of applications.
- b) High stability, convenience (direct access to any MCU through Serial UART (Universal Asynchronous Receiver/Transmitter) operation and integrated with low current warming.
- c) Able to retrieve fingerprint raw data and fingerprint identity files.
- d) Using commercial algorithms with high recognition speed and the collection of fingerprint done by a gentle touch on the sensing area.



Figure 2 The picture of the SN-FPR-UART Finger Print Reader from Cytron Inc.

2.1.2 THE PIC16F648A

The PIC16F648A is the Microcontroller Unit used in this project work. The PIC16F628A belongs to a class of 8-bit Microcontrollers of RISC architecture. It is an 18 pin dual in-line package chip. The PIC16F628A is a tiny but complete computer. It has a CPU (central processing unit), program memory (PROM), working memory (RAM), and two input-ports. The CPU is the "brain" of the computer. It reads and executes instructions from the program memory. As it does so, it

can store and retrieve data in working memory (RAM). CPUs make a distinction between "registers" located within the CPU and "RAM" outside it; the PIC does not, and its general-purpose working RAM is also known as registers." On the 'F628A, there are 68 bytes of general-purpose RAM, located at addresses C to hex 4F. Besides the general-purpose memory, there is a special "working register" or register" where the CPU holds the data it is working on. There are also several special function registers each of which controls the operation of the PIC in some way. The program memory of the 'F648A consists of flash EPROM; it can be recorded and erased electrically, and it retains its contents when powered off. Program memory (FLASH) - for storing a written program. Since memory made in FLASH technology can be programmed and cleared more than once, it makes this microcontroller suitable for device development. EEPROM - data memory that needs to be saved when there is no supply. It is usually used for storing important data that must not be lost if power supply suddenly stops. Many other PICs require ultraviolet light for erasure and are not erasable if you buy the cheaper version without the quartz window. The chip, however, is always erasable and reprogrammable.

2.1.3 The LCD Status Display

The operating status display stage was implemented using the HD44780 based 16x2 LCD which is cheap and can display characters. Figure 3.3 shows the picture of the LCD used with the pin description. The Alphanumeric Liquid Crystal Display (LCD) is used in this design to show the operating status of this embedded security system. By default it displays a welcome message requesting that the user should enter a finger print. And when a match is made it displays "ACCESS GRANTED" otherwise it displays "ACCESS DENIED".



Figure.3 HD44780 based 16x2 LCD

2.2 The Door Movement Mechanism

The mechanism of the motor drive for the modelled automated door is built around a 5V d.c motor controlled in both directions (clockwise and anti-clockwise). To make a d.c motor go in both directions, the polarity of the d.c motor is interchanged.

Transistorised relay switch stages are needed because the outputs of the Microcontroller cannot source enough current to drive the motor directly. When a fingerprint is matched with any of the pre stored fingerprints, the Microcontroller outputs a high (digital 1) on the A1 output pin to drive the motor in the clockwise direction, thereby opening the automated door.

The high output on A1 is given a duration of ten seconds while output A2 remains low (digital 0).

After the ten seconds duration of high on A1, the Microcontroller outputs a high of A2 and a low on A1 for the duration of five seconds, to drive the motor in the anti-clockwise direction, thereby closing the door.

The whole control of the motor direction is implemented by toggling the A1 and A2 according to the table below

Table.1: the truth table for the control of the motor from the outputs of the MCU

Outputs		Motor response
A1	A2	
0	0	Off
0	1	Anticlockwise
1	0	Clockwise

The door itself was fabricated using flat ply-wood sheets. Adhesive gum was used to join the wooden sheets together to form the body of the door system

2.3 Software Design

The software that drives the microcontroller was done using the C language on MPLAB compiler from Microchip Technology Inc. The coding was segmented into various modules; first, the module that drives the LCD screen, this instructs the LCD to display status messages and other messages like 'Place Finger'; next is the module that drives the finger print scanner, this instructs the scanner to first register users and allow the inputted finger print to be compared with the pre-registered finger prints. The pre-registered finger prints are saved on the IC registers of the Micro controller. An alert is sounded whenever a fingerprint that is not found in the Microcontroller memory is placed on the scanner as an intruder.

3 DATA FLOW DIAGRAM

This shows the flow of data between different segments of the security door system as shown below:

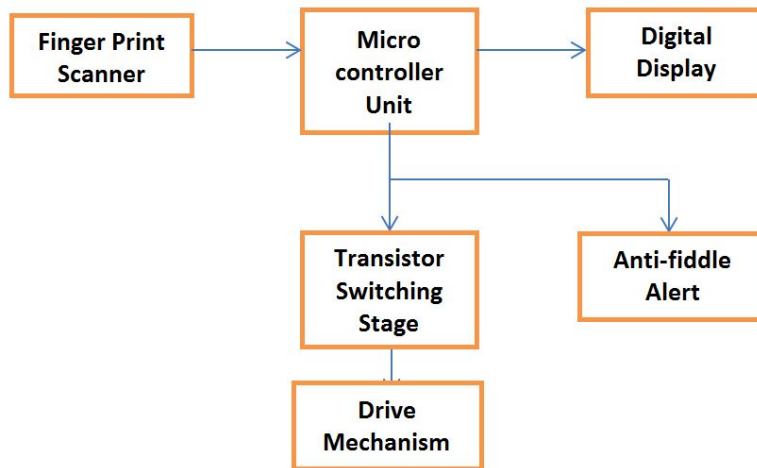


Figure 4: Data flow diagram

4 CONSTRUCTION AND TESTING

4.1 Construction

The physical realization of the project is very vital. Here the paper work is transformed into a finished hardware. After carrying out all the paper design and analysis, the project was implemented, constructed and tested to ensure its working ability. The construction of this project was done in three different stages.

- 1) The writing of the code (driver) which controls the Microcontroller using C language (MPLAB Compiler of Microchip Technology Inc.)
- 2) The implementation of the whole project on a solder-less experiment board.
- 3) The soldering of the circuits on Vero-boards.
- 4) The coupling of the entire project to the casing.

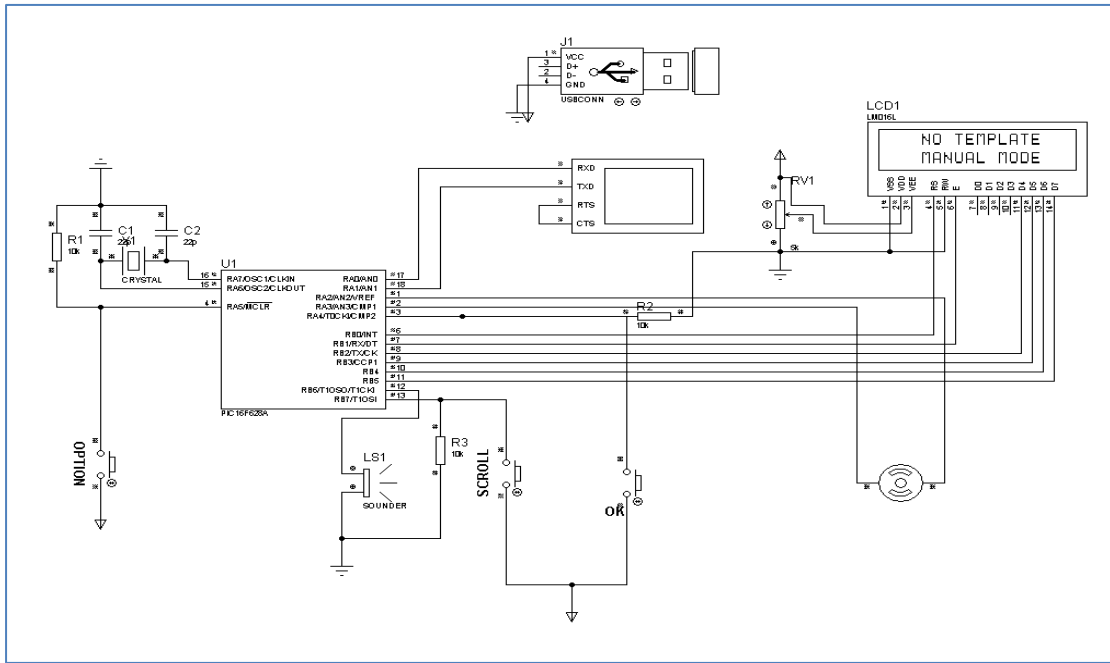
4.2 Implementation

The implementation of this project was done on the breadboard. The power supply was first derived from a bench power supply in the electronics laboratory. To confirm the workability of the circuits before the power supply stage was soldered. The implementation of the project on bread board was successful and it met the desired design aims with each stage performing as designed.

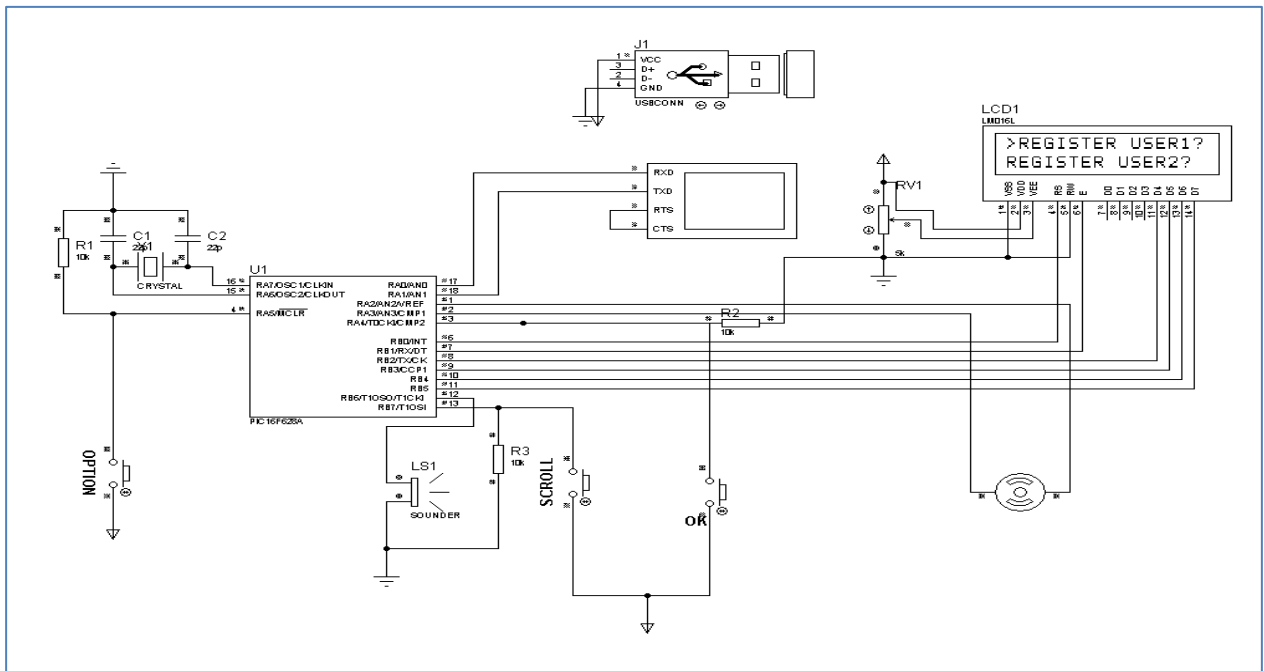
Simulation

The whole electrical part of the project was simulated on PROTEUS simulation platform before the soldering work commenced to observe the operation of the whole project.

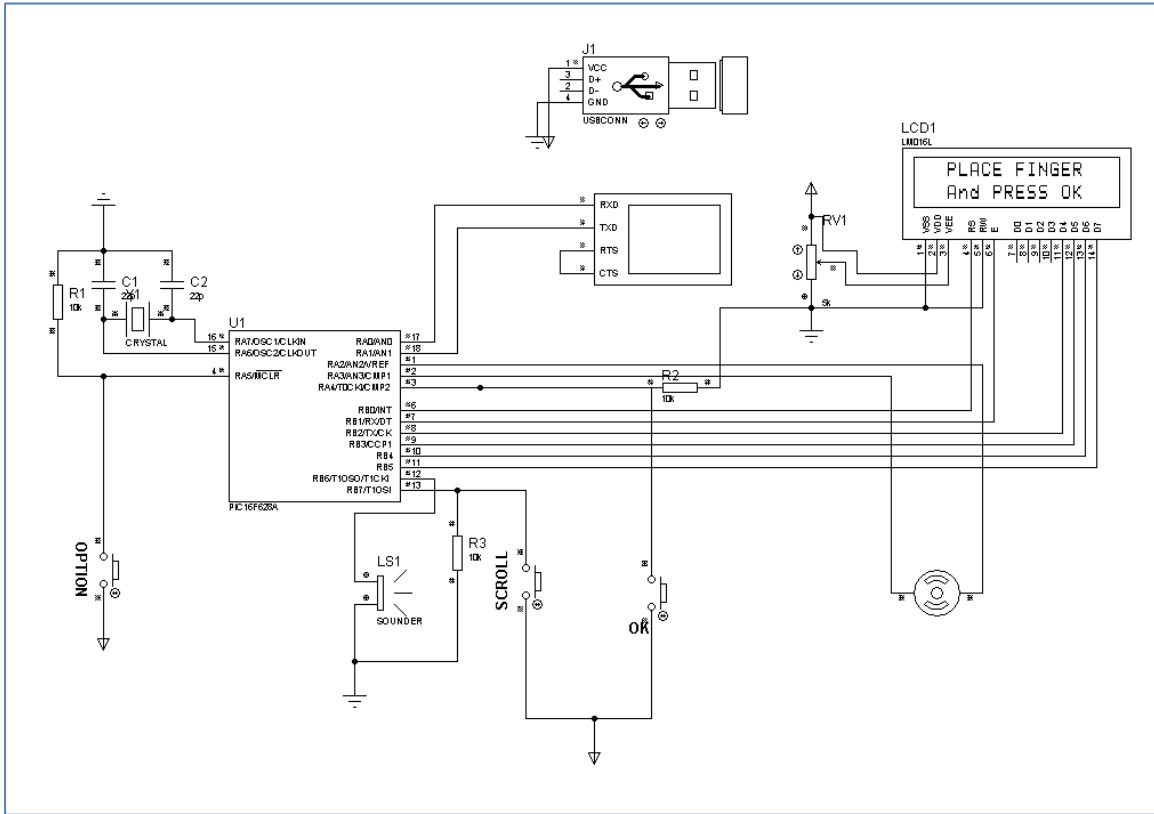
Figures 4.1 a-d shows the simulation screen shots



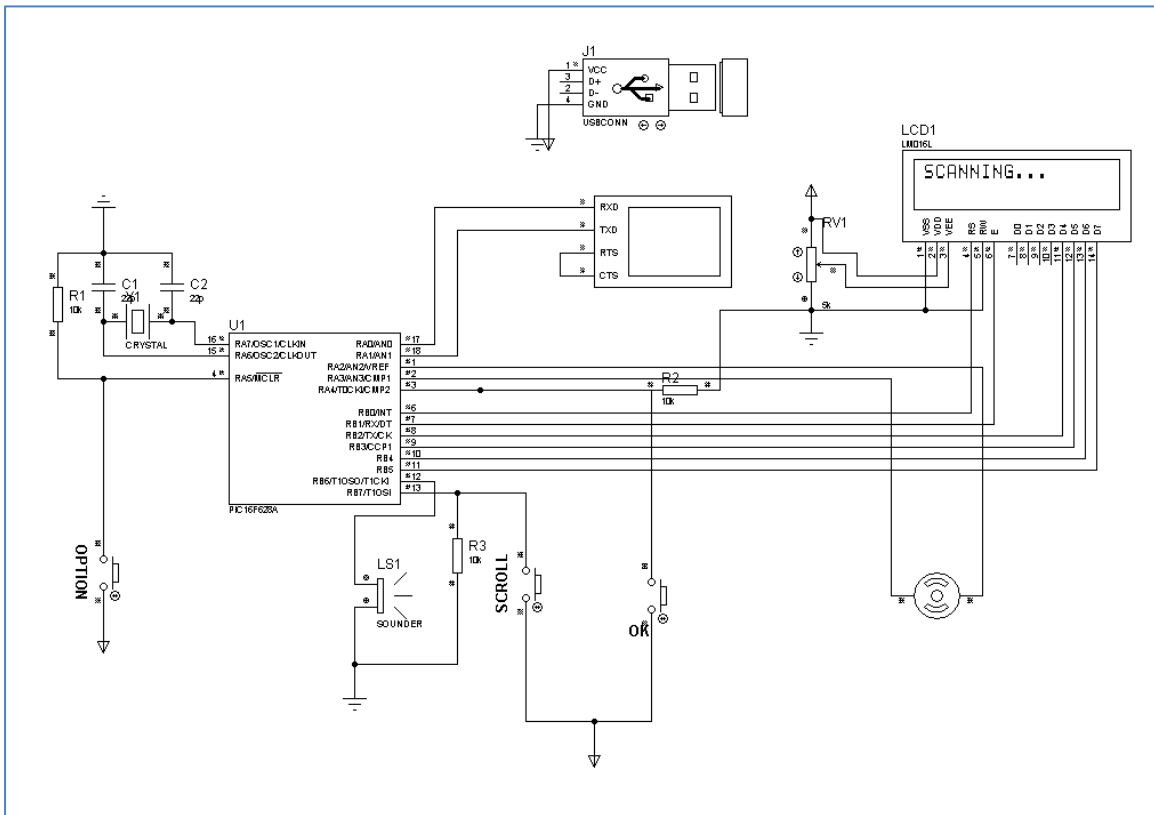
Figures 4.1a shows the simulation screen shot before any finger print was stored



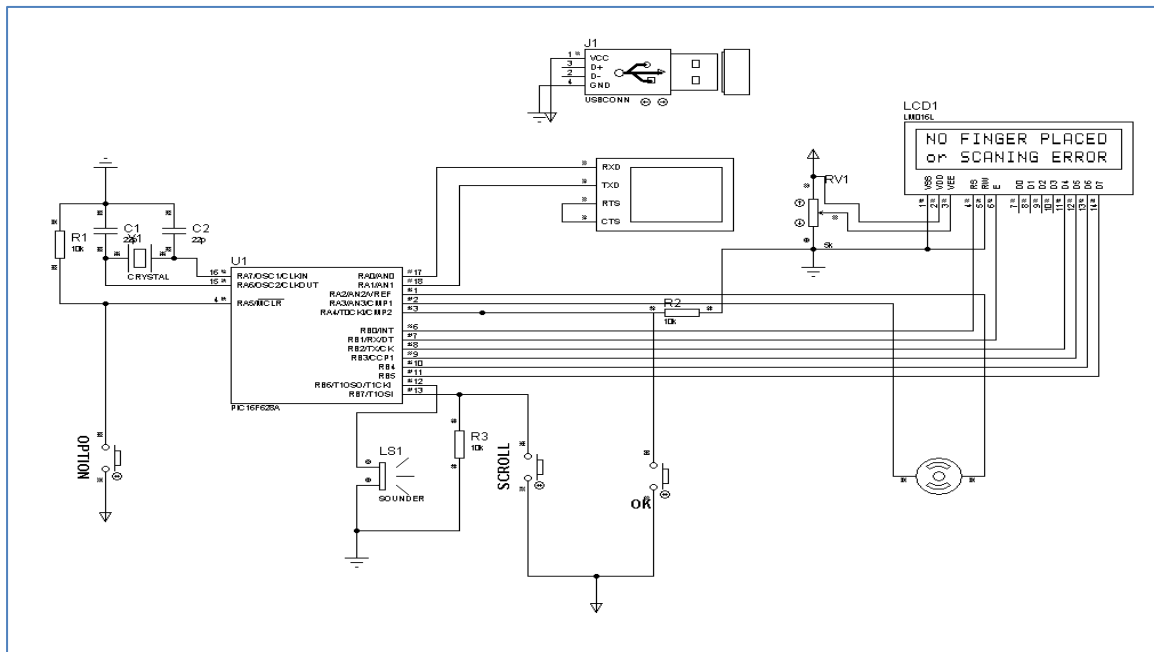
Figures 4.1b shows the simulation screen shot at registering finger print.



Figures 4.1c shows the simulation screen shot after registering finger print (default).



Figures 4.1d shows the simulation screen shot while scanning finger print.



Figures 4.1e shows the simulation screen shot while error occurs at scanning finger print.



Figure 4.2 Picture of the door system before it was enclosed

4.3 Soldering

The various circuits and stages of this project were soldered in tandem to meet desired workability of the project. The power supply stage was first soldered before the microcontroller, digital (LCD) display and finger print reader module stages were done. The soldering of the project was done on Vero-board, and was soldered on two small sized Vero boards. The first Vero board contains the power supply stage, the microcontroller stage with the finger print reader module interface stage; the second Vero board has the transistor switching for driving the motor used to automate the door.

Figure 4.3 below shows the soldering and component arrangement on the various Vero boards. Vero-board 1 has the power supply stage which includes the rectification stage, filtering stage and the voltage regulation stage; and the microcontroller stage.

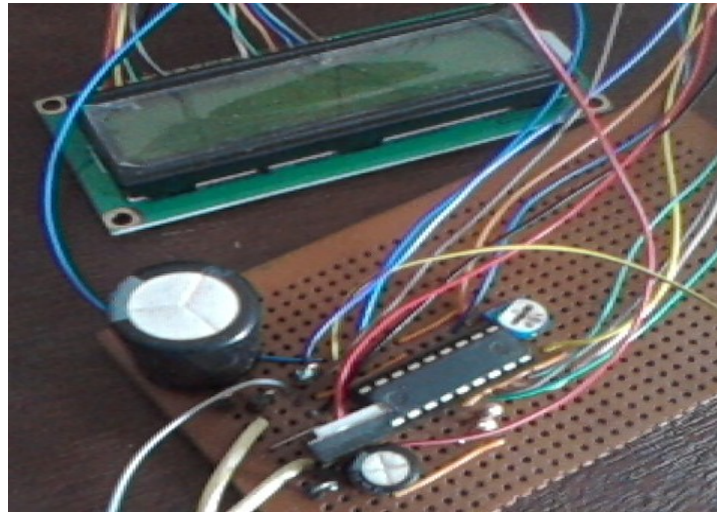


Figure 4.3 components layout on Vero-board.

4.4 Testing

Stage by stage testing was done according to the block representation on the breadboard, before soldering of circuit commenced on Vero board.

The process of testing and implementation involved the use of some test and measuring equipment stated below.

1. **Bench Power Supply:** This was used to supply voltage to the various stages of the circuit during the breadboard test before the power supply in the project was soldered. Also during the soldering of the project the power supply was still used to test various stages before they were finally soldered.
2. **Oscilloscope:** The oscilloscope was used to observe the ripples in the power supply waveform and to ensure that all waveforms were correct and their frequencies accurate. The waveform of the oscillation of the crystal oscillator used was monitor to ensure proper oscillation at 4MHz.
3. **Digital Multi-meter:** The digital multi-meter basically measures voltage, resistance, continuity, current, frequency, temperature and transistor h_{fe} . The process of implementation of the design on the board required the measurement of parameters like, voltage, continuity, current and resistance values of the components and in some cases frequency measurement. The digital multimeter was used to check the output of the voltage regulators used in this project.

5 CONCLUSION

The design is achieved by interfacing a SN-FPR-UART Finger reader with the PIC16F648A Microcontroller, it is the brain box that controls the whole secured door system. An LCD status display is employed to show the operating status of the system. A door movement mechanism is used in the design to make the automated door system move in clockwise and anti-clockwise direction, then finger print input stage was implemented using the SN-FPR-UART. It is a compact fingerprint reader module which is specially designed for project development because of its robustness and the following outstanding features. The development guarantees security for illegal intrusion of any entity to the room, the mechanism can be implemented in a broader sense on a door where there is restriction of access.

REFERENCES

- [1] Cappellir. (2003) "Handbook of Fingerprint Recognition". Chapter synthetic fingerprint generation. Springer, New York.
- [2] Cappelli R., M. Ferrara, and D. Maltoni (2006). "The Quality of Fingerprint Scanners and Its Impact on the Accuracy of Fingerprint Recognition Algorithms". In *Processing of Multimedia Content Representation, Classification and Security (MRCS2006)*, pp 10{16.
- [3] Sukthanker, G (1999), "Face Recognition: A critical look at Biologically-Inspired Approaches", Vol. 2, pp 45-48.
- [4] Tang Homan and Sunny (2001) "Face Recognition Review" Term paper, Department Computer Science and Engineering, Chinese University of Hong Kong, Shatin.
- [5] Valetin D, Abdi H, O' Toole A.J. and Cottrell G.W. (1994), "Connectionist models of Face Processing: A survey", *Pattern recognition*, Vol.27, No.9, pp1209-1230.
- [6] KarlJ.Astrom,Bjorn Wittenmark (1996) *Computer Controlled Systems :Theory and Design*.pp 23-34
- [7] Simon Cole, *Suspect Identities: A history of fingerprinting and criminal identification* (Cambridge, Mass.: Harvard University Press, 2001), pages 60-61.
- [8] Anil. K Jain, Arum Ross, and Prabhakar. S "Fingerprint Matching using Minutiae and Texture features", *proc. International conference on image processing (ICIP)*,pp 282-285, Greece, October 7-10, 2003